NORTHWEST GEOLOGY

The Journal of The Tobacco Root Geological Society

Volume 47, July 2018

43rd Annual Field Conference

Southwest Montana Geology from the Helena Salient to the Drainages Connecting Yellowstone Park

July 27–29, 2018

Two-million-year old basalt flow near Gardiner, Montana thought to represent an early phase of volcanism associated with Yellowstone eruptions. Photo by Alan English.

Published by The Tobacco Root Geological Society, Inc.

P.O. Box 118
Butte, Montana 59703

http://trgs.org

NORTHWEST GEOLOGY

The Journal of The Tobacco Root Geological Society

Requirements for Contributions

TEXT FORMAT: Word Doc (not docm), or plain text (TXT or RTF)
IMAGE FORMAT: JPG—do not embed in Word Docs
DO NOT SUBMIT TABLES OR IMAGES AS EXCEL SPREADSHEETS
FINAL DEADLINE FOR RECEIPT BY EDITORS: JUNE 1 (may be earlier; check website)

Generally, follow USGS style for writing. See COMPLETE REQUIREMENTS at trgs.org. YOU MUST READ AND FOLLOW.

Text should be submitted to the Editor(s) in MS Word-compatible (DOC) format (plain TXT or RTF is fine). **Please DO NOT provide formatting.** Do not assign page numbers, do not double space, do not use columns or backgrounds, **do not indent** anything. Especially, **PLEASE do not include images within Word documents** – they have to be removed, re-formatted, re-sized, and introduced into the publisher program. Word formats images in a way that makes files huge. Do not include large tables in text – make a separate file or image for tables. IMAGES PROVIDED AS WORD DOCUMENTS WILL BE RETURNED.

Photographs and other images should be submitted as JPG or PDF files, **separate** from text. Dimensions should be so that the full size of the image is approximately as it will be displayed – that is, if it will be 3 inches wide when printed, 3 inches wide when displayed on the computer monitor will be adequate. We can interpret most image formats; **this does not include Word or Excel, which are not image formats. ANYTHING SENT AS AN EXCEL SPREADSHEET WILL BE RETURNED.**

Scanned images and line drawings should be at NO MORE than 300 dots per inch resolution. The native size, as displayed on a computer screen should generally be no larger than the screen. If necessary, we can scan hard-copy drawings or photos for you – this is preferable to submitting images in unusual file formats. Figure captions should be submitted as a separate text file, or part of the text file.

Road Logs **must** be accompanied by (at a minimum) a location map of stops; ideally, a geologic map with stops would be included. Such maps should be provided separately from the text.

Please use the following bibliographic format. Note especially capitalization and use and position of commas and colons. For journals, do not abbreviate except J. for "journal" and U.S. in "U.S. Geological Survey."

Sears, J.W., and Hendrix, M., 2004, Lewis and Clark Line and the rotational origin of the Alberta and Helena Salients, North American Cordillera: *in* Sussman, A., and Weill, A., eds., Orogenic Curvature: Geological Society of America Special Paper 383, p.173-186.

Tikoff, B., and Teyssier, C., 1992, Crustal-scale, en-echelon P-shear tensional bridges: a possible solution to the batholithic room problem: Geology, v.20, p. 927-930.

Color images are accepted at our discretion, and will only be included if the color is critical to the understanding of the image (e.g., a complex geologic map). Images including photographs can be submitted in color, but expect that we will likely convert them to grayscale. Each color page adds about $200 to the cost of a normal press run of the guidebook.

Topics: In general, papers published in Northwest Geology do NOT need to be directly related to a particular TRGS Field Conference.

Abstracts: In general, we prefer to NOT publish stand-alone abstracts. Exceptions may be made, but we encourage you to create a short paper (which can be thought of as an expanded abstract) including at least one informative map, cross section, or image.

The Tobacco Root Geological Society, Inc.
P.O. Box 2734 • Missoula, Montana 59806
http://trgs.org

NORTHWEST GEOLOGY

The Journal of The Tobacco Root Geological Society

Volume 47, July 2018

43rd Annual Field Conference

Southwest Montana Geology from the Helena Salient to the Drainages Connecting Yellowstone Park

July 27–29, 2018

Published by The Tobacco Root Geological Society, Inc.
P.O. Box 118
Butte, Montana 59703

http://trgs.org

Edited by: Sandy Underwood and Katie McDonald

The Tobacco Root Geological Society, Inc.

P.O. Box 118
Butte, Montana 59703

Officers, 2017:

President: Jesse Mosolf, Montana Bureau of Mines and Geology, Butte, MT
Vice-President: William M. Phillips, Idaho Geological Survey, Moscow, ID
Treasurer: Katie McDonald, Montana Bureau of Mines and Geology, Butte, MT
Secretary: Emily Geraghty Ward, Rocky Mountain College, Billings, MT
Corresponding Secretary: Lara Strickland, Columbus, MT
Webmasters: Petr Yakovlev (Butte, MT)

Board of Directors, 2017:

Ted Antonioli, Geologist, Missoula, MT
Bruce E. Cox, Geologist (semi-retired), Missoula, MT
Larry Johnson, Consultant, Missoula, MT
Larry N. Smith, Dept. of Geological Engineering, Montana Tech, Butte, MT
Mike Stickney, Montana Bureau of Mines and Geology, Butte, MT
Robert C. Thomas, Dept. of Environmental Sciences, U. of Montana-Western, Dillon, MT
Emily Geraghty Ward, Geology Dept., Rocky Mountain College, Billings, MT

2018 Conference Organizers:

Sandy Underwood, John Childs, and David R. Lageson, Bozeman, Montana

Editors: Sandy Underwood and Katie McDonald (MBMG)

Layout and Editing: Susan Barth (MBMG)

Printed by Insty-Prints, Butte, Montana

ISSN: 0096-7769

http://trgs.org

NORTHWEST GEOLOGY

The Journal of The Tobacco Root Geological Society

Volume 47, July 2018

Southwest Montana Geology from the Helena Salient to the Drainages Connecting Yellowstone Park

TABLE OF CONTENTS

TRGS 2018 SCHOLARSHIP AWARD WINNERS

- Alexander Brown (Foster), Montana Tech

  Understanding the geology and geochemistry of ore formation at the Golden Chest Mine

- Garett Brown (TRGS), University of Georgia

  Testing for ecological gradients in the lower Mississippian Lodgepole Formation, Montana, USA

- Andrew Del Turco (Harrison), Stockton University

  Thermodynamic evolution of the Wyoming Province: Application of quartz c-axis analysis to constrain the kinematics and temperature of deformation recorded in the Jewel Lake quartzite, southwestern Montana

- Alexander Flores (Kleinkopf), Stockton University

  Petrophysical characterization of the North Snowy Block, southwestern Montana: Application of rock magnetism to understanding Precambrian tectonics

- Richard M. Hess (TRGS), University of Georgia

  The Sequence stratigraphic architecture of the Upper and Middle Jurassic Stump and Preuss Formations, Western Wyoming and Eastern Idaho, USA

- Leah Houser (TRGS), Utah State University

  Textural and thermochronologic constraints on the role of friction generated heat on silica-rich fault mirror surfaces of the Brigham City Segment, Wasatch fault zone, Utah

- Kimberly Kramer (TRGS), Washington State University

  Quantifying paleo-peak geothermal field gradients within three ranges in eastern Nevada

- Derek Lichtner (TRGS), University of Wyoming

  Assessing sediment preservation completeness using mass conservation and depositional signal inversion: Wasatch Formation, southwest Wyoming

- Evan Martin (TRGS), University of Idaho

  Assessing the topographic evolution of the North American Cordillera in Idaho, Wyoming and Montana during Tertiary time

- Sierra Swenson (Skipp), University of Georgia, Athens

  Integrated sequence stratigraphy and paleobiology of the Sundance Seaway, Montana, USA

- Jacob Thacker (TRGS), University of New Mexico

  The spatiotemporal evolution of Laramide deformation: An integrated geologic and thermochronologic study

- Matthew Wanker (TRGS), Indiana University

  Dynamics of sediment transport through a river bifurcation

TRGS CHARTER MEMBERS

Stanley W. Anderson
Clyde Cody
William S. Cordua
Lanny H. Fisk
Richard I. Gibson†
Thomas Hanley
Stephen W. Henderson
Thomas E. Hendrix
Mac R. Hooton
Inda Immega
Steven W. Koehler
Marian Millen Lankston†
Robert W. Lankston†
J. David Lazor
Joe J. Liteheiser, Jr.
Judson Mead*
Marvin R. Miller
Vicki M. Miller*
Allen H. Nelson
Alfred H. Pekarek
Patricia Price*
Donald L. Rasmussen
Raymond M. Rene

TRGS LIFETIME MEMBERS

John Childs
Rob Foster
Joan (Mrs. Jack) Harrison*
Karen Keefer
Layaka Mann
Chris Pool

† = co-founder
* = deceased

TRGS HAMMER AWARD RECIPIENTS

Awarded for distinguished achievement in the study of the geology of the Northern Rocky Mountains

1993: Ed Ruppel*
1994: Dick Berg
2003: Don Winston
2004: Dean Kleinkopf*
2009: Betty Skipp
2010: Jim Sears
2011: John Childs
2012: J. Michael O'Neill
2013: Paul Karl Link
2014: Reed Lewis
2015: Jeff Lonn
2016: Bruce Cox

TRGS HONORARY MEMBERS

1980: Charles J. Vitaliano*
2008: Elizabeth Younggren
(also honorary Board member)
2010: Dick Berg
2010: Bruce Cox
2010: Dean Kleinkopf*
2010: Dave Lageson
2011: Marie Marshall Garsjo
2011: Paul Link
2011: Rob Thomas
2012: Jeff Lonn
2012: Mitch Reynolds
2013: Reed Lewis
2015: Don Winston

PAPERS

XENOLITHS IN THE NORTHERN CRAZY MOUNTAINS: CONSTRAINING MAGMA YIELD STRENGTH FROM FIELD OBSERVATIONS

Francis Ö. Dudás

Massachusetts Institute of Technology, Cambridge, MA 02139

ABSTRACT

This paper describes two xenolith locations in the northern Crazy Mountains of central Montana. Host rocks at both locations are Eocene alkaline igneous rocks that are part of the Central Montana Alkaline Province. A total of 85% of felsic xenoliths at Castle Creek are Archean felsic gneisses. They constitute ~15 vol.% in one of the three intrusions, and range up to 1.4 m in length. A census indicates that there are no felsic xenoliths smaller than 7 cm; amphibolite and clinopyroxenite xenoliths show a continuum of sizes from 20 cm to <1 cm, merging with the size distribution of clinopyroxene phenocrysts. The lower size limit of felsic xenoliths is interpreted to reflect Bingham trapping. Simple calculations constrain the yield strength of the magma to ≤20 Pa. Similar calculations for mafic xenoliths suggest yield strengths ≤60 Pa. Yield strength was an insignificant factor in xenolith transport. At Cottonwood Creek, xenoliths are mostly clinopyroxenite cumulates from mafic alkaline magmas, with a few peridotites. Mineral chemistry indicates that the xenoliths are not strictly cognate with their host magma, and that the peridotites derive from a different source than the clinopyroxenites. P-T estimates from CaO in olivine suggest peridotite entrainment at 10–16 kbar and 1100–1150°C, near the crust-mantle boundary.

INTRODUCTION

The Crazy Mountains are the southernmost major igneous center of the Central Montana Alkaline Province (CMAP). Baker and Berg (1991) provide an overview of the CMAP. The most recent geochemical study of the Crazy Mountains is Dudás (1990), and much of the following description draws on that work. The alkaline magmatism of the Crazy Mountains differs from that of other CMAP centers in being sodic rather than potassic. Alkaline rocks generally occur north of the Shields River drainage, whereas the igneous rocks south of the Shields River are dominantly subalkaline (fig. 1). In the field, the two series are distinguishable by the presence of plagioclase, which occurs only in the subalkaline rocks. The alkaline and subalkaline rocks are contemporaneous, within dating uncertainty, and were intruded between 48 and 52 Ma (du Bray and Harlan, 1996; Harlan, 2006; Harlan and others, 1988). No coeval extrusive rocks have yet been documented in the Crazy Mountains.

There are five major groups of mafic alkaline rocks in the Crazy Mountains (table 1). Among these, the mafic nepheline syenites (MNS, or malignite) are most common. They are dominantly clinopyroxene–biotite–K-feldspar–nepheline rocks, but sometimes also contain olivine, sodalite (or nosean or hauynite), and accessory apatite and magnetite. Alteration of nepheline has produced cancrinite and natrolite, and zeolites occur along veins and fractures. Rheomorphic fenites dominated by aegirine, sanidine, and nepheline, but containing unusual minerals (including barytolamprophyllite, eudialyte, wadeite, loparite, priderite, and others), occur in association with some of the MNS intrusions (Chakhmouradian and Mitchell, 2002). Holocrystalline MNS forms large sills or laccoliths (Gordon Butte, Ibex Butte, Great Cliffs, Anticlinal Phacolith) and porphyritic varieties form dikes. Cumulate MNS typically contains >10 vol.% olivine in addition to clinopyroxene; it occurs toward the base of some MNS sills (Anticlinal Phacolith), and in dikes. Analcime-bearing MNS typically contains analcime in addition to nepheline as a phenocryst phase, usually in porphyritic rocks with partially aligned K-feldspar phenocrysts. It is not clear whether the analcime is a primary igneous phase. These rocks are more felsic than the MNS, and form small sills (Great Cliffs, Goat Mountain). A suite of clinopyroxene–analcime ± biotite rocks occurs predominantly as dikes. These rocks have a fine-grained groundmass, appear to contain no feldspar, and may contain magmatic carbonate; they are thus the analcime-bearing equivalents of nephelinites (analcimite). It is likely that analcime is secondary after leucite, but no preserved leucite has been found in these rocks. There are a number of other mafic alkaline rock types in the dikes that occur in the Crazy Mountains, including lamprophyres (minette) and pseudoleucite-bearing malignites.

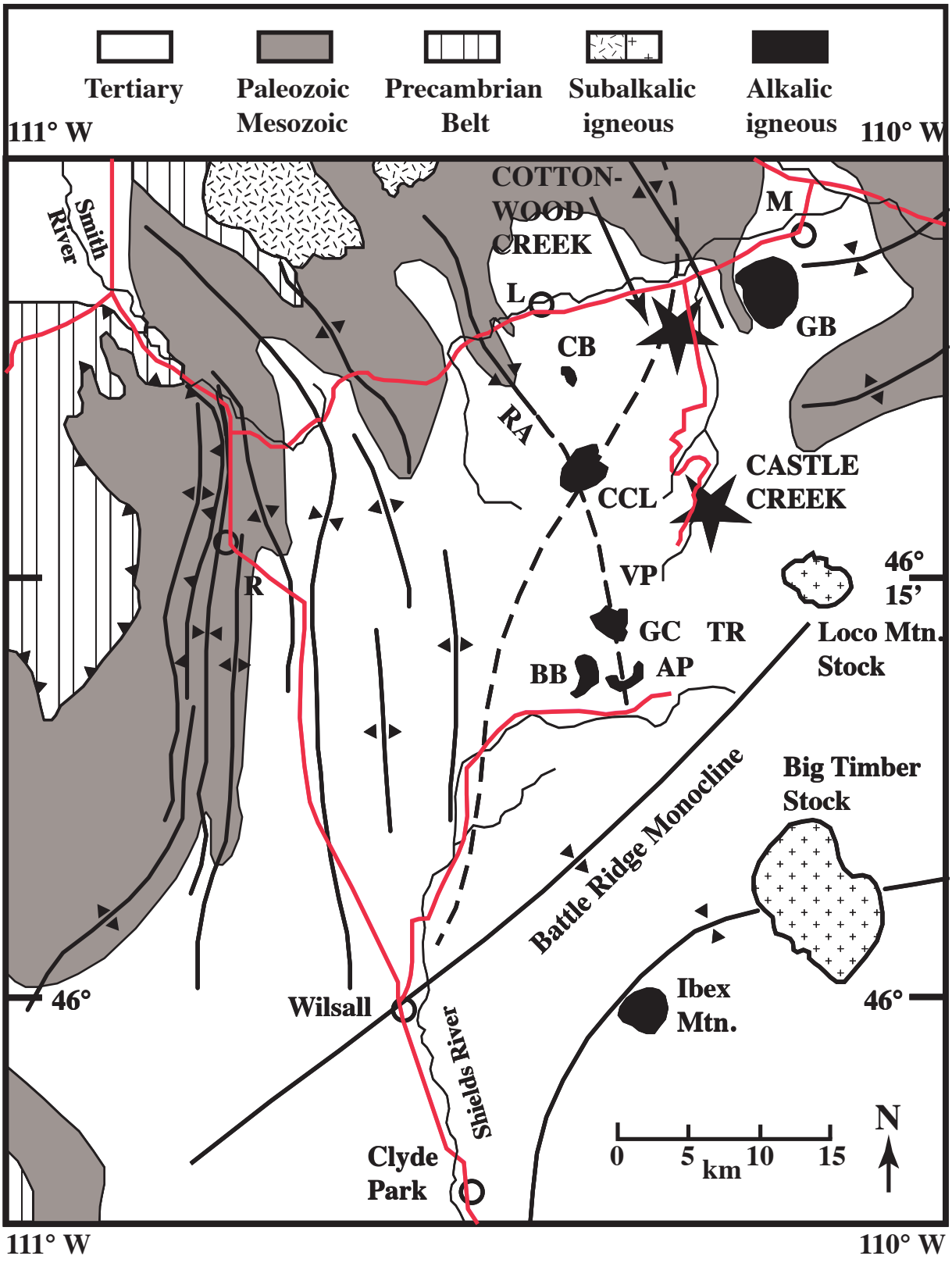

Figure 1. Generalized geological map of the Crazy Mountains area, showing the xenolith locations at Castle Creek and Cottonwood Creek. Towns include: L, Lennep; M, Martinsdale; R, Ringling. Geological locations: AP, Anticlinal Phacolith; BB, Billie Butte; CB, Comb Butte; CCL, Comb Creek Laccolith; GB, Gordon Butte; GC, Great Cliffs; RA, Robinson Anticline; TR, Target Rock; VP, Virginia Peak. The heavy dashed line extending from north to south is the approximate eastern limit of the Montana Disturbed Belt. Map based on Woodward (1982) and Ross (1955).

Table 1. Major element compositions of mafic alkalic rocks in the Crazy Mountains.

	MNS *n* = 57 (wt. %)	Cum MNS *n* = 5 (wt. %)	An MNS *n* = 8 (wt. %)	Analcimite *n* = 7 (wt. %)	Others *n* = 5 (wt. %)
SiO_2	46.83 ± 1.68	44.64 ± 1.59	51.39 ± 1.42	43.34 ± 2.48	48.06 ± 0.85
TiO_2	0.97 ± 0.12	0.91 ± 0.19	0.69 ± 0.11	0.93 ± 0.16	0.99 ± 0.09
Al_2O_3	13.36 ± 1.45	10.05 ± 1.45	15.06 ± 1.86	11.96 ± 0.87	13.98 ± 0.90
Fe_2O_3 (T)	9.41 ± 0.92	9.87 ± 0.41	7.38 ± 0.88	9.97 ± 1.00	9.34 ± 0.70
FeO	3.43 ± 0.61	5.63 ± 0.69	2.87 ± 0.20	3.57 ± 0.09	3.78 ± 0.40
Fe_2O_3	5.66 ± 1.06	3.58 ± 1.12	4.58 ± 0.71	6.50 ± 0.78	5.41 ± 0.67
MnO	0.17 ± 0.03	0.16 ± 0.01	0.14 ± 0.01	0.18 ± 0.02	0.17 ± 0.02
MgO	6.53 ± 1.79	12.74 ± 3.59	4.40 ± 1.41	7.32 ± 1.22	6.06 ± 0.85
CaO	9.87 ± 1.76	11.50 ± 2.57	6.46 ± 1.68	13.19 ± 1.49	8.73 ± 0.46
Na_2O	5.36 ± 1.00	3.57 ± 1.42	6.21 ± 0.70	4.70 ± 1.93	3.94 ± 1.43
K_2O	3.78 ± 1.05	1.98 ± 0.85	4.64 ± 0.76	1.37 ± 0.40	5.19 ± 1.16
P_2O_5	1.18 ± 0.33	0.78 ± 0.19	0.73 ± 0.14	0.99 ± 0.19	1.06 ± 0.20
Mg-number	60.8 ± 6.5	74.1 ± 5.2	56.8 ± 7.7	62.8 ± 5.6	60.0 ± 2.2

Note. MNS, mafic nepheline syenite; Cum MNS, cumulate mafic nepheline syenite; An MNS, analcime-bearing mafic nepheline syenite. Others: pseudoleucite mafic nepheline syenite, minette, lamprophyre.

Felsic alkaline rocks in the Crazy Mountains include nepheline syenite (the Comb Creek laccolith) and textural variants of nepheline syenite (pulaskite: Comb Butte, Virginia Peak, Target Rock) that form small intrusions, sills, and dikes. Analcime-bearing syenites also occur as small intrusions (Billie Butte). A quartz-normative alkali syenite forms a sill-like intrusion near Comb Butte, and phonolite and K-feldspar phonolite porphyries form resistant dikes. Rhomb porphyry and trachyte dikes also occur in the dike swarm that is centered on the Comb Creek laccolith. Among the felsic rocks, there are also numerous dikes and sills (Scab Rock Mtn.) of what is likely a hybrid between the alkaline and subalkaline series: these are latitic or trachytic rocks that contain plagioclase and hornblende, sometimes with quartz, or with analcime. A variant of these hybrid trachytes is commonly strongly carbonated, and consequently weathers easily and is friable.

Xenoliths in the Crazy Mountains occur in a range of rock types. Clinopyroxene-rich xenoliths occur in several MNS dikes and intrusions, in analcimites, and in analcime syenites; rare peridotites occur only in MNS; Archean gneiss xenoliths occur in MNS or its derivatives in at least two locations; and amphibolites and amphibolitic gneisses occur in some MNS dikes, but are most common in hybrid trachytes. Clinopyroxene-rich and amphibolite xenoliths tend to be small, mostly <5 cm in diameter, whereas the Archean gneiss xenoliths range up to almost 1.5 m in maximum dimension. The first section of this paper describes the Castle Creek pipes, where these large Archean gneiss xenoliths occur, and evaluates the mechanics of intrusion and transport of these xenoliths; the second section of this paper describes a location, along Cottonwood Creek, where clinopyroxene-rich xenoliths occur.

ANALYTICAL METHODS

Detailed descriptions of the analytical methods are given in Dudás (1990). The bulk of the major and trace element analyses were done at the Mineral Constitution Laboratory (Pennsylvania State University) by DC-plasma optical emission spectrophotometry on solutions generated by lithium metaborate fusion. Uncertainties for major elements are better than 2% relative, except for P_2O_5 (~5% relative). Uncertainties for trace elements are better than 10% relative, except for

Cr, V, and Y (~20% relative). A suite of trace element analyses was done by neutron activation analysis in the laboratory of R. Korotev at Washington University, St. Louis. Isotopic analyses of Sr and Nd were done under the supervision of R. Carlson at the Department of Terrestrial Magnetism of the Carnegie Institution of Washington. $^{87}Sr/^{86}Sr$ is reported relative to 0.710250 for NBS-978 after fractionation correction using $^{86}Sr/^{88}Sr = 0.1194$. Nd isotopic compositions were corrected for fractionation using 0.7219 for $^{146}Nd/^{144}Nd$, and are reported relative to CHUR = 0.512635. The reported carbon and oxygen isotopic analyses were done in the laboratory of P. Deines at Pennsylvania State University. Melting and crystallization experiments were conducted in the laboratory of D. Eggler at Pennsylvania State University. Electron microprobe analyses were done at the Mineral Constitution Laboratory (Pennsylvania State University), using a 3-spectrometer Etec Autoprobe, natural mineral standards, and Bence-Albee corrections. A small number of whole-rock analyses were done by X-Ray Assay Labs, Don Mills, Ontario, Canada.

SECTION 1: CASTLE CREEK

Introduction

Castle Creek is a tributary on the east side of Cottonwood Creek, north of Forest Lake. On the north side of Castle Creek, three volcanic pipes rise above the enclosing Paleocene sedimentary rocks: these pipes are the "castles" for which the creek is named. Robinson (1965) first described these intrusions. Archean felsic xenoliths constitute about 15 vol.% of these pipes, and range up to 1.5 m in maximum dimension. The abundance and size of these xenoliths motivated this study: what were the dynamics of the magma system that transported them?

The pipes are emplaced into Paleocene, terrigenous, clastic sedimentary rocks of the Crazy Mountains Basin (fig. 1). A narrow hornfels rim, typically narrower than 50 cm, but in places extending to several meters, surrounds the pipes (fig. 2). The only optically identifiable phase in the hornfels is microcrystalline aegirine, and the hornfels can be considered a fenite. There is no evidence to determine whether these pipes vented to the surface, and there is no estimate of where the current level of exposure may be with respect to the paleo-surface.

Five igneous lithologies occur within and around the pipes. The chilled margins of the pipes have compositions comparable to the malignite porphyries that are the most abundant rock type among the alkalic rocks of the northern Crazy Mountains. Rocks of the chilled margin, best exposed on the east side of the southern pipe, are black porphyries that contain up to 15 vol.% of apple-green, diopside phenocrysts that range up to 1 cm in length. Biotite phenocrysts are slightly smaller, and constitute up to 5 vol.% (fig. 3A). The groundmass consists of plumose or uniformly fine-grained K-feldspars that show no twinning, interstitial analcime, clinopyroxene, biotite, opaque oxides, or apatite. Only traces of alteration—chlorite and carbonate—occur in the chilled margin samples, though some interstitial analcime likely replaces igneous nepheline. Like other malignite porphyries in the

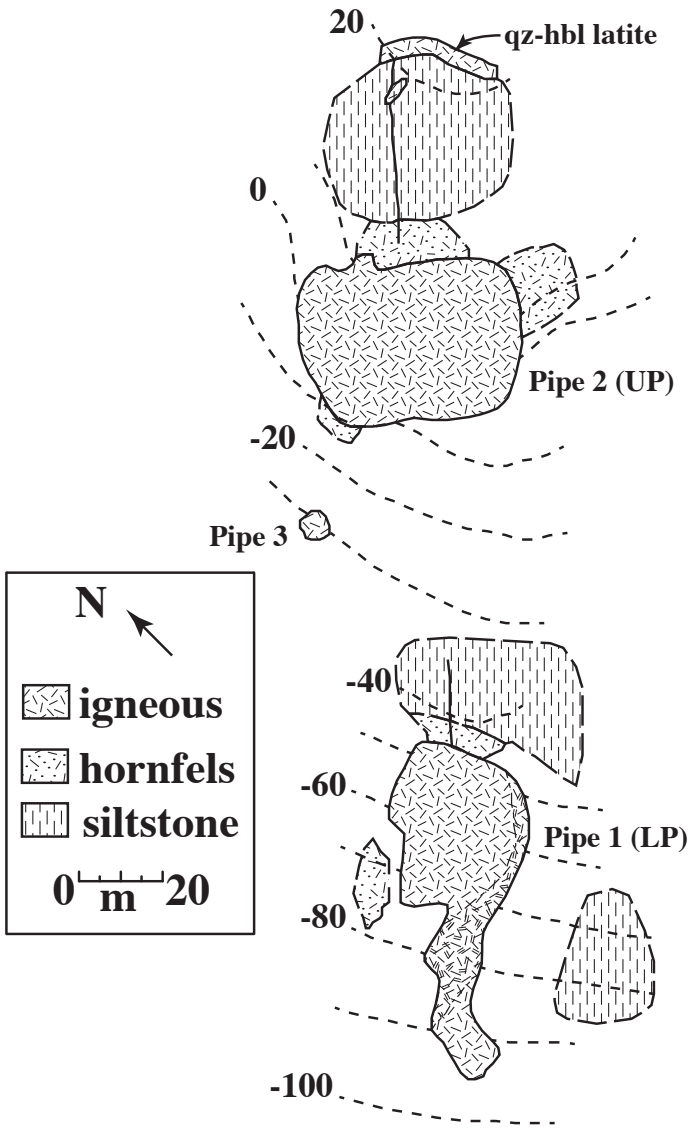

Figure 2. Geological sketch map of the area around the Castle Creek intrusions. Unpatterned areas are covered by talus and soil. The heavily patterned area on the east side of Pipe 1 is the chilled margin of the intrusion. Elevation contours are in meters, relative to 0 = 6,600 ft (based on Lebo Quadrangle topographic map).

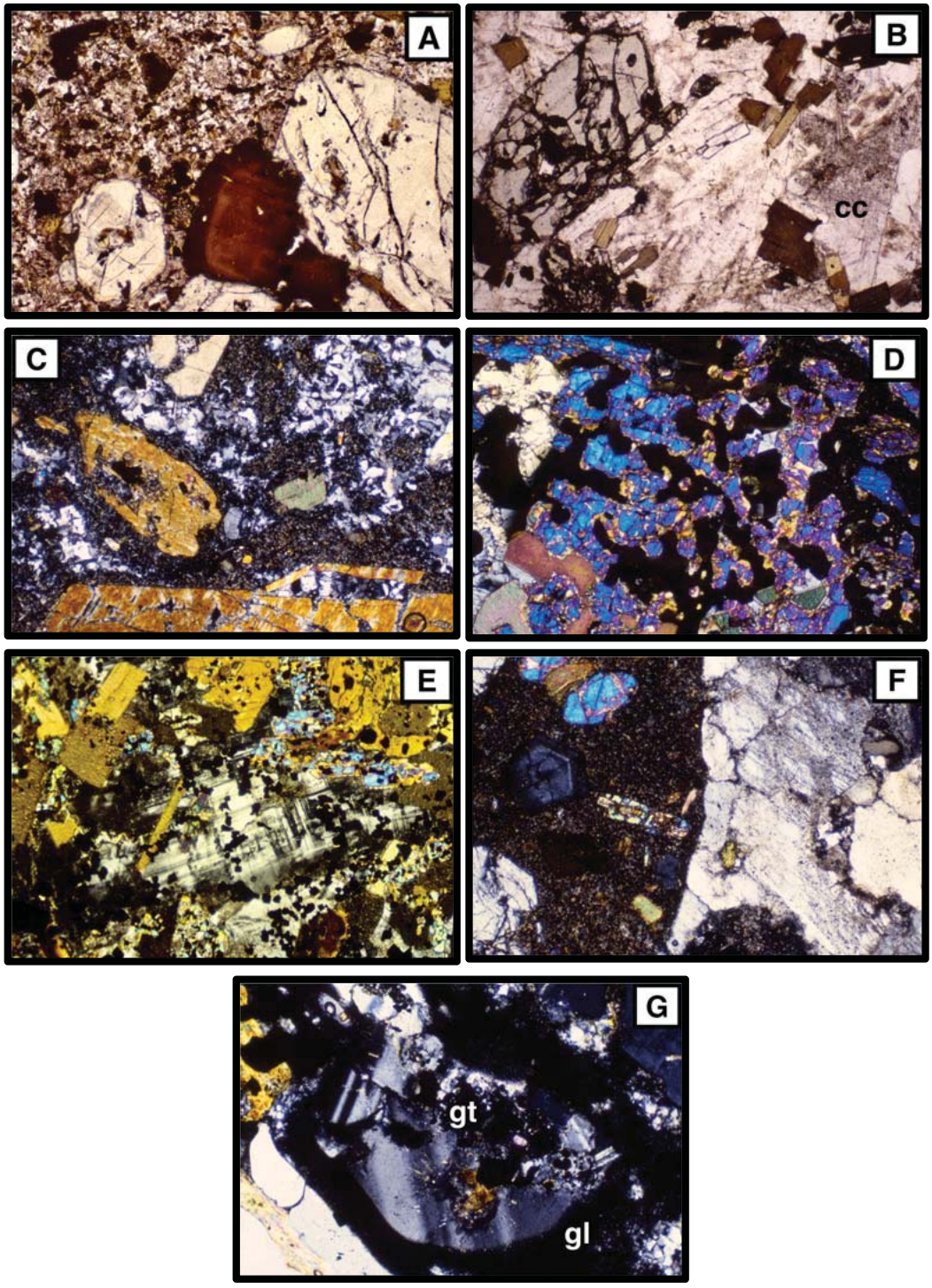

Figure 3. Photomicrographs of thin sections from Castle Creek. All images are 2.2 mm horizontally, unless otherwise indicated. A, Chilled margin sample UP6, showing coarse clinopyroxene and zoned biotite, with a fine-grained groundmass containing a second generation of biotite. B, Sample UP7. Typical fabric of the main phase of the intrusions, with coarse clinopyroxene, biotite, feldspars and calcite (cc). C, Sample LP15. The matrix at the upper right contains an aggregate of K-feldspar and quartz that is interpreted to be crystallized partial melt from a felsic gneiss xenolith. Crossed polarizers. D, Sample UP-FLT. A biotite clinopyroxenite xenolith showing oikocrystic biotite at extinction, enclosing clinopyroxene that remains in optical continuity. Crossed polarizers. E, Sample FL25-2X. An amphibolite xenolith. Microcline and scattered magnetite are interpreted to be products of interaction with the host magma. The clinopyroxene rim (blue interference colors) on amphibole is interpreted to reflect dehydration of amphibole during heating of the xenolith. Crossed polarizers. F, Sample LP10. The margins of some felsic gneiss xenoliths are very sharp, and the host magma in some cases is chilled against the xenolith boundary. Crossed polarizers. G, Sample LP15. Partial melt, solidified as glass (gl) within a felsic gneiss xenolith, formed along the grain boundary of feldspar and quartz. Garnet (gt) is isotropic, enclosed within feldspar. Image is 1 mm horizontally.

Crazy Mountains, the chilled margin samples contain no plagioclase. The chilled margin composition (UP 6, table 2) provides the "uncontaminated" end member for evaluating the extent of mixing between the original magma and the melts derived from the xenoliths.

The dominant volume of the pipes consists of a tan- to flesh-colored, variably altered, fine- to medium-grained, weakly porphyritic rock of monzonitic composition. The rock consists of a holocrystalline matrix of plagioclase and K-feldspar (2–4 mm), with partly altered xenocrysts or phenocrysts of clinopyroxene and biotite, a second generation of finer-grained clinopyroxene and biotite, minor amphibole, and accessory apatite and opaque oxides (fig. 3B). Quartz occurs in some samples, as anhedral grains up to 4 mm. Coarse clinopyroxene crystals (up to 15 mm in length) are partly carbonated and chloritized, and large (to 5 mm), potentially primary calcite grains (based on $\delta^{13}C$ and $\delta^{18}O$ measurements that are near expected magmatic compositions; Dudás, 1990) occur interstitially between the feldspar laths. Some but not all samples of this rock are quartz-normative (FL1; table 2). Similar rocks occur in scattered, strongly altered and weathered dikes along the Cottonwood Creek drainage in the northern Crazy Mountains. In all cases, these dikes also contain xenoliths, mostly strongly carbonate-altered biotite clinopyroxenites.

Irregular, usually elongate, aggregates of quartz–plagioclase–K-feldspar occur in the matrix of the monzonite (fig. 3C) near the margins of some felsic gneiss xenoliths. These are interpreted as fragments that have spalled from the xenoliths, and are invariably less than 4 cm long and 0.5–1 cm wide. The wisp-like textures and indefinite boundaries of some of these aggregates also suggest that the fragmentation of the xenoliths involved partial melting of the xenolith margins.

The northernmost igneous exposure in figure 2 is a quartz hornblende latite porphyry dike that has affinities to the quartz-saturated, sub-alkalic rocks associated with the Loco Mountain and Big Timber stocks. This dike contains no xenoliths. A nepheline normative amphibole porphyry (FL31, table 2) dike crops out just west of the area shown in figure 2; this dike contains amphibolite xenoliths (FL31X, table 2). The fifth igneous lithology in the area is a rhomb porphyry (trachyte porphyry) dike with K-feldspar phenocrysts up to 10 cm long in a tan, carbonate-altered, fine-grained groundmass; it is discontinuously exposed west of the northern edge of the southern pipe. This dike is also free of xenoliths.

Xenoliths: Observations and Data

Four types of xenoliths occur in the pipes. Small (2–4 cm), angular hornfels xenoliths are locally abundant in the malignite porphyry along the margins of the southern pipe, but have not been found in the main body of the pipes. These are interpreted to derive from the immediate host rocks of the pipe.

The second suite of xenoliths includes mafic to ultramafic biotite pyroxenites. These are interpreted to be xenoliths derived from early crystallization of the malignite porphyry magma. Similar xenoliths are discussed in Section 2 below and occur in other malignite porphyries in the northern Crazy Mountains. In the Castle Creek pipes, these xenoliths are smaller than 20 cm in diameter; their average size is near 2 cm. Locally, especially in the northern pipe, they are abundant, averaging 2–5 xenoliths per m^2 of pipe area. Typically, they have centimeter-sized biotite oikocrysts enclosing remnants of clinopyroxene that remain in optical continuity (fig. 3D). Olivine is rare in these xenoliths. In some, K-feldspar veinlets mark zones of interaction with the host magma; in others, K-feldspar and amphibole occur with biotite and clinopyroxene, possibly as reaction products between magma and xenolith. Opaque oxides and apatite are minor constituents. Many of these xenoliths are friable. No chemical analyses of these are available because of their generally small size.

Amphibolites constitute the third xenolith population. These are the least abundant xenoliths, and no amphibolites larger than 10 cm have been found. The amphibolites have reacted with the host magma more intensely than other xenoliths. They commonly contain carbonate and abundant K-feldspar (fig. 3E; FL23X, FL25-1X, FL25-2X, FL31X in table 2). Amphibole breakdown to opaque Fe-oxides is evident in some xenoliths, and CO_2-rich fluid inclusions (aqueous fluid, CO_2 fluid, and CO_2 vapor are visible) occur in several.

The most spectacular xenoliths are felsic gneisses that range up to 1.5 m in length and constitute up to 15 vol.% of the southern pipe (fig. 4). They are not uniformly distributed. They occur exclusively in monzonitic host rocks, and are abundant in the southern and middle pipes, but are uncommon in the northern

Table 2. Major element compositions and CIPW norms of selected samples, Castle Creek.

	Pipe Samples						Dike	Xenoliths						
	Chilled Margins (wt. %)			Main Body				Felsic Gneisses			Amphibolites			
	UP6	UP6/2	UP7	FL1	FL21	FL25	FL31	FL3X	FL5X	FL8X	FL23X	FL25-1X	FL25-2X	FL31X
SiO_2	50.90	50.70	51.10	53.80	57.20	55.00	50.80	70.70	73.10	71.30	47.40	46.70	44.20	48.10
TiO_2	1.11	1.11	1.10	1.02	0.82	0.91	1.15	0.43	0.06	0.22	1.35	1.51	1.80	0.97
Al_2O_3	12.30	12.20	13.20	12.40	15.70	15.30	14.90	14.60	14.60	15.70	9.37	12.70	12.90	14.90
Fe_2O_3(T)	9.72	9.64	9.91	8.72	7.11	7.64	10.50	2.85	0.40	1.35	8.70	12.30	17.80	12.50
FeO				3.59		2.66				0.80				
Fe_2O_3				4.73		4.69				0.46				
MnO	0.16	0.15	0.16	0.12	0.12	0.13	0.16	0.02	0.01	0.01	0.12	0.18	0.21	0.24
MgO	7.33	7.30	5.73	5.90	4.05	4.36	5.16	0.97	0.18	0.67	14.70	8.13	8.75	8.22
CaO	9.58	9.60	8.84	9.15	4.98	5.87	7.21	0.71	0.40	1.80	11.20	8.74	9.00	8.41
Na_2O	3.01	3.03	3.15	3.12	5.13	4.79	4.39	3.84	3.76	5.87	1.18	2.69	3.16	3.51
K_2O	3.68	3.64	3.20	2.87	4.31	4.27	2.91	5.09	5.75	1.80	3.94	4.17	2.21	2.11
P_2O_5	0.70	0.69	0.74	0.62	0.50	0.55	1.09	0.13	0.04	0.05	0.19	1.50	0.39	0.11
LOI	0.55	0.65	1.15											
CO_2				2.66	0.65	0.27								
Total	98.49	98.06	97.13	100.38	100.57	99.09	98.27	99.34	98.30	98.77	98.15	98.62	100.42	99.07
CIPW Norms (wt. %)														
q				4.20				25.09	28.04	25.00				
or	21.75	21.51	18.91	16.96	25.47	25.23	17.20	30.08	33.98	10.64	17.31	24.64	13.06	12.47
ab	18.33	18.19	26.65	26.40	43.09	34.59	31.18	32.49	31.82	49.67		10.34	8.27	19.12
an	9.18	8.94	12.43	11.35	7.08	7.64	12.36	2.67	1.72	8.60	8.63	10.26	14.49	18.67
ne	3.87	4.04			0.17	3.22	3.23				5.41	6.73	10.01	5.73
lc											4.68			
cor								1.79	1.56	0.94				
ol	10.65	10.40	9.88		9.55	8.73	12.32				19.58	16.79	20.98	18.13
fo	6.71	6.57	5.59		5.38	4.94	6.47				15.76	10.14	10.98	10.57
fa	3.93	3.82	4.29		4.17	3.79	5.85				3.82	6.66	10.00	7.57
opx			0.04	18.10				5.04	0.83	2.89				
en			0.03	11.41				2.42	0.45	1.67				
fs			0.02	6.70				2.62	0.38	1.22				
cpx	27.39	27.72	21.75	10.72	8.38	13.24	13.39				36.31	18.96	22.71	18.23
di	18.72	18.98	13.53	7.09	5.20	8.23	7.81				30.47	12.48	13.20	11.63
hd	8.68	8.74	8.22	3.63	3.19	5.01	5.59				5.85	6.48	9.51	6.59
mt	4.23	4.19	4.31	3.79	3.09	3.32	4.57	1.24	0.17	0.59	3.78	5.35	7.74	5.44
ilm	2.11	2.11	2.09	1.94	1.56	1.73	2.18	0.82	0.11	0.42	2.56	2.87	3.42	1.84
ap	1.02	1.00	1.08	0.90	0.73	0.80	1.59	0.19	0.06	0.07	0.28	2.18	0.57	0.16
cc				6.05	1.48	0.61								
Total	98.52	98.09	97.10	100.41	100.60	99.11	98.02	99.41	98.29	98.81	98.55	98.13	101.24	99.79

Figure 4. Photograph of the west side of Pipe 1, showing prominent felsic gneiss xenoliths. Dr. D.P. Gold at right.

pipe. These xenoliths (FL3X, FL5X, FL8X in table 2) consist of quartz, plagioclase, and K-feldspar (fig. 3F), with accessory amounts of biotite, apatite, zircon, and opaque oxides. Garnet occurs in some. The host magma is chilled against the margins of some of these xenoliths, and the xenoliths then have sharp margins. A small percentage of the xenoliths (<10%) contain biotite in excess of 5 vol.%, and are distinguishable by color. Thin sections of these xenoliths show that a small volume of partial melt (typically <10 vol.%) is present in the outer 10 cm of these xenoliths, and garnet and biotite have both reacted with the melt in this partial melting rind (fig. 3G).

There is no macroscopic evidence of relative motion between the felsic xenoliths and the host magma. No sag structures occur below them, nor obvious grain orientations along their margins or tops.

A census of 189 xenoliths (table 3; fig. 5) in the middle (Pipe 3) and southern (Pipe 1) pipes showed that 161 (85%) of the xenoliths in the monzonitic host rock are felsic gneisses. Xenoliths of other lithologies are all smaller than 60 cm, and most are smaller than

Table 3. Census of xenoliths at Castle Creek.

Size (cm)	Pipe 1	QFG	METASED	BIOGN	Other	Pipe 3	QFG	METASED	BIOGN	Other	Total	%
> 100	5	5									5	2.65
90 - 100	5	4	1								5	2.65
80 - 90	4	4									4	2.12
70 - 80	7	7									7	3.70
60 - 70	7	7									7	3.70
50 - 60	14	12	1	1							14	7.41
40 - 50	9	7	2			3	2	1			12	6.35
30 - 40	25	23	1	1		2			2		27	14.29
25 - 30	16	12	1	2	1	5	4		1		21	11.11
20 - 25	14	13	1			9	8	1			23	12.17
15 - 20	22	21		1		8	6		1	1	30	15.87
10 - 15	16	12	4			7	4	1		2	23	12.17
7 - 10	8	8				3	2			1	11	5.82
< 7	0					0					0	0
TOTAL	152	135	11	5	1	37	26	3	4	4	189	
%		88.82	7.24	3.29	0.66		70.27	8.11	10.81	10.81		

Note. Size is maximum dimension. QFG, quartzofeldspathic gneiss; METASED, metasedimentary rock, mostly quartzite; BIOGN, biotite-bearing gneiss, mostly QFG with >5% bio; Other usually applies to indeterminate lithologies, or to rare volcanics.

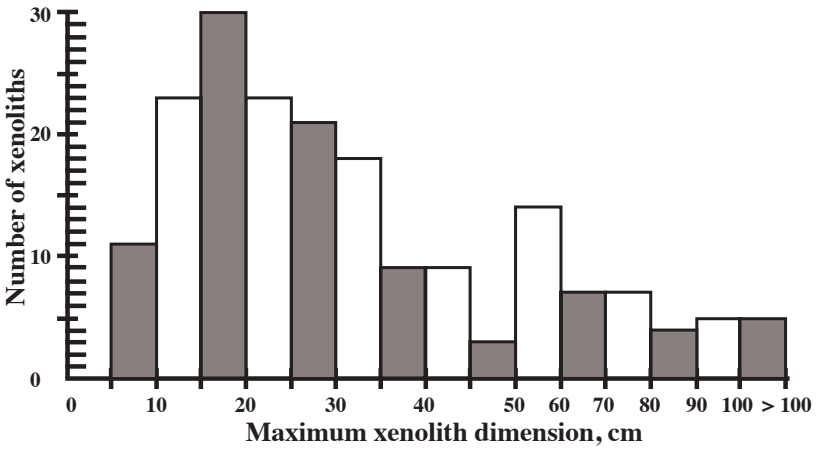

Figure 5. Histogram of sizes of felsic xenoliths. No xenoliths smaller than 7 cm (maximum dimension) were observed among the felsic xenoliths. Note the change in size categories at 50 cm.

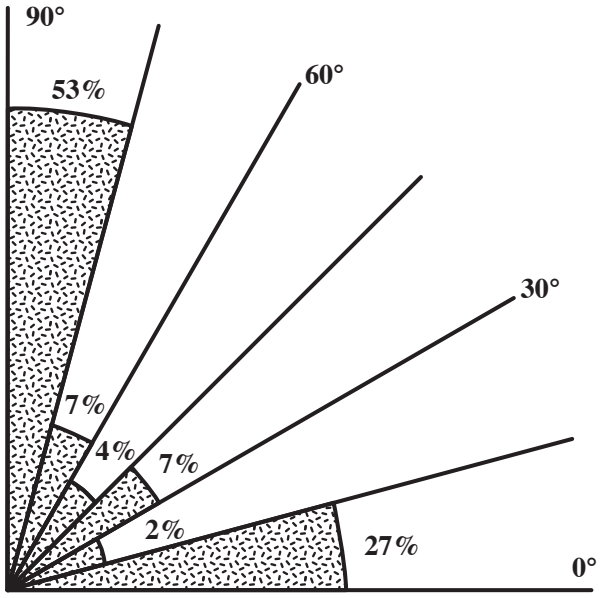

Figure 6. Orientation of felsic xenoliths. The majority of xenoliths are oriented with their long axis nearly vertical.

25 cm. By contrast, the felsic gneiss xenoliths average 35 cm, and 6% of the xenoliths exceed 1 m. There is a distinct drop in felsic gneiss xenolith abundance at sizes below 10 cm; only 6% of xenoliths are smaller than 10 cm, and the census recorded no felsic gneiss xenoliths smaller than 7 cm.

Xenolith orientation appears not to be random. Where some estimate of the orientation of the long axis of the xenolith could be made (170 of 189 xenoliths), 53% have long axes within 15° of vertical (fig. 6), and 27% are within 15° of horizontal. Sampling of xenolith alignment is biased because the best exposures on which orientation could be determined are near the walls of the pipes, where edge effects potentially affect flow and particle orientations; there are few well-exposed vertical sections in the interiors of the pipes.

The felsic granitoid and gneiss xenoliths are interpreted to be samples of the Archean basement. No granitoids or gneisses occur in the stratigraphy near the pipes, other than in the Archean. Nd and Pb isotopic data for the gneiss xenoliths (table 4) are consistent with Archean provenance.

The depth to Archean basement in the vicinity of the pipes is estimated to be about 4 km. Tertiary and Cretaceous strata in this part of the Crazy Mountains Basin have a total thickness of about 3.5 km (Feltis, 1985), a thickness constrained by structural reconstructions and by oil and gas exploration wells to the west of the northern Crazy Mountains. Underlying this basin-fill, there is a relatively thin Mesozoic section of shallow marine and terrigenous sedimentary rocks, and a Paleozoic section that probably consists dominantly of carbonates; these likely total less than 0.8 km in thickness (McMannis, 1965). The metasedimentary xenoliths in the pipes are all quartzites, and probably derive from the basal Paleozoic unit, the Flathead Fm. The Proterozoic Belt Supergroup, which is exposed to the north and northwest of the Crazy Mountains Basin (fig. 1), may pinch out in the subsurface near the location of the pipes (near the Battle Ridge Monocline; Woodward, 1981), and Proterozoic strata thus contribute a negligible thickness to the stratigraphic section. Thus, the minimum vertical transport distance for the Archean xenoliths, assuming that they derive from the uppermost Archean strata, is about 4 km. No estimate for the maximum depth of these xenoliths is possible because their mineralogy is not amenable to geobarometry.

Geochemical Data

Tables 2, 4, and 5 show geochemical data. The malignite porphyry in the chilled margin of the pipes is feldspathoid-normative and broadly basaltic in composition. It is geochemically similar to numerous other malignite porphyry dikes in the northern Crazy Mountains. The main body of the pipes, represented by samples FL1, FL21, and FL25, is heterogeneous, and varies from being feldspathoid-normative to quartz-normative. The dominant control on this variability is interpreted to be contamination by both melt and solid fragments derived from the felsic gneiss xenoliths.

The geochemical contrast between the feldspathoid-normative chilled margin and the felsic

Table 4. Isotopic compositions of selected Castle Creek samples.

	Pipe Samples	Xenoliths			
	Main Body	Felsic Gneisses			Amphibolites
	FL1	FL3X	FL5X	FL8X	FL31X
$^{87}Rb / ^{86}Sr$	0.1762	0.5176	1.0433	0.1739	0.0671
$^{87}Sr / ^{86}Sr(m)$	0.707590 ± 40	0.718312 ± 34	0.737364 ± 34	0.709876 ± 32	0.706627 ± 27
$^{87}Sr / ^{86}Sr(i, 50)$	0.707465	0.717944	0.736623	0.709752	0.706579
$^{147}Sm / ^{144}Nd$				0.1025	0.1262
$^{143}Nd / ^{144}Nd$ (m)				0.510871 ± 33	0.511625 ± 31
$^{143}Nd / ^{144}Nd$ (i, 50)				0.510837	0.511584
T_{DM}				2.96	2.49
$^{206}Pb / ^{204}Pb$			15.05	14.77	
$^{207}Pb / ^{204}Pb$			15.30	15.06	
$^{208}Pb / ^{204}Pb$			34.38	36.13	
	cc	qz	qz	qz	
$\delta^{18}O$ (SMOW)	11.46	8.8 ± 0.1	10.2 ± 0.3	7.8 ± 0.4	
$\delta^{13}C$ (PDB)	-6.31				

Note. cc, calcite; qz, quartz.

gneiss xenoliths makes it possible to estimate the extent of mixing between the host magma and the xenoliths. Because it is clear from petrographic evidence that bulk samples of the pipe include both xenocrysts from disaggregated xenoliths and some amount of partial melt from these xenoliths, the composition of the felsic mixing component is best approximated by the average composition of the xenoliths, and not by some estimate of the minimum melt composition. Using the average xenolith composition, the amount of mixing, based on major element data, ranges from about 15% in FL1, 30% in FL25, and to 40% in FL21, with an uncertainty of about 10%. The uncertainty reflects the limited sampling of the xenoliths, their chemical variability, and the selective alteration of feldspars in the xenoliths that causes variability in the CaO, Na_2O, and K_2O data. Estimates of the extent of mixing based either on trace element abundances or isotopic compositions are less successful because of the large variation in trace element abundances and isotopic compositions among the xenoliths, as well as the limited sampling of the xenoliths.

What is clear from the geochemical data is that the main body of the pipes is poorly mixed, and that no single estimate of magma composition is meaningful. Though it is geochemically a "monzonite," it is a monzonite because of mixing between a ne-normative MNS magma and felsic components derived from the xenoliths.

Discussion

The transport of xenoliths depends on magma ascent velocity, on the density contrast between xenoliths and the surrounding magma, on the effective viscosity of the magma, and on the yield strength of the magma. Theoretical models describe and can be used to predict the density and viscosity of single-phase silicate liquids over a range of temperatures and pressures (e.g., Bottinga and others, 1982; Ghiorso and Sack, 1995; Giordano and others, 2006; Lange and Carmichael, 1990; Shaw, 1972). These models are based on laboratory experiments. Theoretical models can also predict the density and viscosity of two-phase (melt plus solid, melt plus vapor) mixtures, but the experimental verification of these predictions is more

Table 5. Trace element data for selected samples from Castle Creek.

	Pipe Samples						Dike	Xenoliths						
	Chilled Margins			Main Body				Felsic Gneisses			Amphibolites			
	UP6 (data in ppm)	UP6/2	UP7	FL1	FL21	FL25	FL31	FL3X	FL5X	FL8X	FL23X	FL25-1X	FL25-2X	FL31X
Rb	72	64	80	71	100	110	48	105	131	45.6	115	120	50	31.6
Sr	1730	1750	2220	1160	1160	1420	1430	600	363	760	520	1380	1390	1380
Ba	2300	2270	2800	2000	2340	2400	2450	2000	1180	440	3550	3850	1610	1580
Y	28	18	35	35		30		10	5	5	15	30		
Zr	131	127	95	140	300	220	220	320	40	25	100	190	190	25
Nb	43	37	29	35		40		10		5	35	55		
Sc				23.6		16.23				1.64				
V				175		175		40	15		120	270		
Cr				255		130		15	5	1.62	790	125	250	325
Co				32.5		23				3.17				
Ni				75		40				5	255	85		
Cu				98	69	70	60	2	5	18	185	195	180	54
Zn				65	90	85	105	15		25	60	115	140	125
Cs				1.36		1.39				0.472				
Be				2.9		4				1.3	1.5	3.2		
Hf				4.11		6.16				3.98				
Ta				0.67		1.18				0.06				
Sb				0.114		0.075				0.021				
Th				7.5		13				0.44				
U				1.61		2.81				0.22				
La				62.6	80	106	85	120	30	12.9	15	70	15	
Ce				131		205				21.5				
Nd				61		85				7.14				37.9
Sm				9.95		11.8				1.21				7.91
Eu				2.41		2.81				1.21				
Tb				0.74		0.82				0.135				
Yb				1.69		2.12				0.28				
Lu				0.231		0.303				0.06				

difficult and not entirely successful (Møller and others, 2006), particularly at high solid or vapor contents (Stein and Spera, 1992; Walsh and Saar, 2008). Much work focuses on melt–vapor systems (Gonnermann and Manga, 2007; Rust and others, 2003) and on physical properties of plutons during crystallization (Petford, 2003; Yoshinobu and others, 2009), where the shape of the entrained solids impacts the effective viscosity. Experimental verification of effective viscosity for magmas containing large (>1 cm) solid fragments or vapor bubbles is not currently possible. Theoretical prediction and experimental measurement of magma properties is just beginning to address three-phase systems (melt, vapor, solid; Harris and Allen, 2008; Longo and others, 2009; Sahagian, 2005), but it is these systems that are of greatest concern in terms of understanding eruption and flow dynamics.

Early laboratory experiments used Stokes' law to determine melt viscosity. By measuring the settling rate of spheres having a known density contrast with respect to the melt in the experimental capsule, the viscosity can be calculated. A version of this method can be applied to field observations, but in a magma conduit, there is no fixed frame of reference with respect to which the rate of settling can be measured, and the most important parameter is not absolute displacement, but the relative motion between magma and xenolith. Because xenolith size is a proxy for xenolith mass, however, the xenolith size at which there is no relative motion between the magma and the xenolith—the mass at which Bingham trapping occurs—is a size from which magma yield strength can be approximated.

Sparks and others (1977) proposed the idea of Bingham trapping of xenoliths, and Sachs and Stange (1993) developed its theoretical framework. Conceptually, Bingham trapping of solid fragments occurs during magma flow when the yield strength of the magma is sufficient to support the excess mass of a solid fragment whose density exceeds that of the magma itself. This is termed Bingham trapping because the magma has a finite yield strength—it is not a Newtonian fluid—and, despite the density difference between the magma and the xenolith, the xenolith is "trapped" by the magma, with no relative motion between magma and xenolith. The behavior of magma when solids or vapor bubbles are present resembles that of a Bingham fluid.

At xenolith masses (or sizes) larger than the mass at which Bingham trapping occurs, the relative motion between xenolith and magma can cause ablation of the xenolith, reducing its size (Sachs and Stange, 1993). The rate of ablation depends both on the rate of advection of heat to the xenolith–magma interface and the rate of removal of xenolithic material from the interface. Ablation continues until there is no relative motion between xenolith and magma. The consequences of this conceptual model are that ablated xenoliths have ellipsoidal to subspherical geometries, that the xenolith size distribution has a relatively sharp lower bound, and that the magma is progressively contaminated by material ablated from the xenoliths. There is potentially both physical evidence of xenolith ablation (the xenolith size distribution) and a geochemical signature with which the process of ablation can be tracked.

All of the relevant magma properties (density, viscosity, temperature, chemical composition) change progressively with pressure along the intrusion path. The entrainment and ablation of "cold" xenoliths chills the magma, so that "heat death" (freezing of the magma in the conduit) would occur more rapidly in a xenolith-bearing intrusion than in a xenolith-free system. This implies that intrusions with a large xenolith load, particularly with a "cold," crustal xenolith load, are capable only of limited vertical ascent.

For xenoliths of different densities, the size at which Bingham trapping occurs changes—dense, mafic xenoliths have a smaller Bingham trapping size than felsic xenoliths, though both have the same excess mass. Thus, in magmas that contain a range of xenolith lithologies, it is possible to get multiple estimates of yield strength, and, ideally, these constrain the "real" value. This study presents observational evidence that, at Castle Creek, there is a minimum xenolith size (between 7 and 10 cm for felsic gneiss xenoliths, and ~2 cm for multi-grain amphibolite and clinopyroxenite xenoliths) and geochemical data that track contamination of the host magma (mixing of 15–40% of average felsic gneiss compositions into the chilled margin composition).

Spera (1984) derived two equations for xenolith settling rate that differ because flow behavior changes as a function of flow velocity as reflected in the Reynolds number (Rex). For Rex >2, the equation is:

$$Ux = 0.344(\Delta\rho g/\rho l)^{5/7}(\rho l/\eta l)^{3/7}(R_n - 15\sigma_o/4\Delta\rho g)^{8/7}$$

For Rex < 2, the equation is:

$$Ux = (2/9)(\Delta\rho g/\eta l)(R_x - 15\sigma_o/4\Delta\rho g)^2,$$

where:

Ux is the xenolith settling rate,

$\Delta\rho$ is the density contrast between xenolith and magma,

g is the acceleration due to gravity,

ρl is the density of the magma,

ηl is the plastic viscosity of the Bingham magma,

R_x is the xenolith radius, and

σ_o is the yield strength of the magma.

The Reynolds number of the xenolith is defined to be ρl Dx Ux/ηl, where Dx is the xenolith diameter. The equations treat xenoliths as spherical solids. Based on reasonable estimates of $\Delta\rho$, ρl, and ηl, with g being constant, and Rx being measured, the xenolith settling rate, Ux, and the magma yield strength, σ_o, can be calculated. The density and viscosity values can be constrained, but not specified exactly; thus, computation of the settling rate and yield strength tests a range of density and viscosity values.

Estimates of Magma and Xenolith Density

The geochemical data in table 2 were used to calculate magma densities for the chilled margin and mixed magma samples. Because the chilled margin samples contain <20% phenocrysts, densities calculated using partial molar densities from Lange and Carmichael (1990) are a usable approximation. For the four analyses that constrain the least contaminated magma composition (UP6, UP6/2, UP7, and FL31), the calculated melt densities at atmospheric pressure and 1,100°C range from 2,601 to 2,621 kg/m^3. The magma temperature is constrained by experiments on malignite whole rock compositions (Dudás, 1990). At atmospheric pressure, the liquidus of the least fractionated malignite (AP4) in the Crazy Mountains is near 1,290°C, with olivine on the liquidus. Clinopyroxene appears as a second phase near 1,270°C. No other phases are stable above 1,100°C. The chilled margin composition of the Castle Creek pipes is less magnesian than the least fractionated malignite, and olivine is absent, but clinopyroxene phenocrysts are present. A reasonable estimate of chilled margin magma temperature is thus below the clinopyroxene liquidus of the experimental charges, but above the liquidus of nepheline and feldspar (~1,050°C).

The main body of the Castle Creek pipes was probably not a melt-only system at any point in its history, and calculations of the physical properties of the mixed magma samples have large uncertainties. For the same conditions as for the chilled margin (P = 1 atm., T = 1100°C), the mixed magma samples have calculated densities between 2,505 and 2,575 kg/m^3.

Several factors affect the calculated density. Corsaro and Pompilio (2004) have calculated the impact of these factors on the density of alkalic melt compositions that occur at Etna. They found that melt compressibility as a function of changing pressure causes a density decrease of ~5% between 1,000 MPa and 0.1 MPa. A temperature drop of ~400°C, from 1,300°C to 900°C, causes a density increase of about 4%. Addition of 15 wt.% mafic phenocrysts (e.g., clinopyroxene) to the magma increases the density by ~2%. The volatile content of the magma affects the density of the magma in two ways. Dissolved volatiles have a large effect; at constant T and P, the dissolution of 3 wt.% water in an alkaline basaltic magma decreases density by ~8 %; carbon dioxide has a much smaller effect than water, and typically has much lower solubility. At low pressures, the volatiles in the magma are progressively exsolved and form a separate vapor phase, which dramatically decreases magma density.

The most significant difference between the conditions at Etna and the Castle Creek locality is that, at Etna, the magma source is at great depth, and consequently the P and T range over which density changes need to be tracked is much greater. At Castle Creek, it is difficult to adduce evidence for vertical xenolith transport over more than 4 km. At such shallow depths, the P and T ranges are smaller, and volatile solubility is much lower. The important conclusion from evaluation of the sensitivity of magma density to various factors is that, at Castle Creek, it is unlikely that magma density was below 2340 kg/m^3 (i.e., 2,600 kg/m^3 less 10%). The calculations utilized this range of magma densities, but assumed a base case magma density of 2,500 kg/m^3.

Xenolith densities were calculated from their normative compositions. At 25°C, these range from 2,640 to 2,690 kg/m^3 for the felsic xenoliths, and from 3,220

to 3,565 kg/m^3 for the mafic xenoliths. The minimum possible densities for these xenoliths, at 1,100°C, range from 2,610 to 2,660 and 3,190 to 3,530 kg/m^3, respectively. Some of the felsic xenoliths could be almost neutrally buoyant with respect to the calculated density of the uncontaminated, anhydrous host magma, whereas the mafic xenoliths may have a density contrast of up to 1,200 kg/m^3 with respect to the mixed magma. Because the presence of volatiles would decrease the initial magma density, it is unlikely that any of the xenoliths were positively buoyant in the magma at the time of intrusion. Furthermore, the evidence of chilling of the host magma against some xenoliths, and the limitation of partial melting to the outer 10 cm of the xenoliths, indicate that the bulk of the xenoliths remained "cold," and therefore relatively dense. In the yield strength calculations, the density contrast between the magma and the felsic xenoliths was assumed to lie between 10 and 200 kg/m^3.

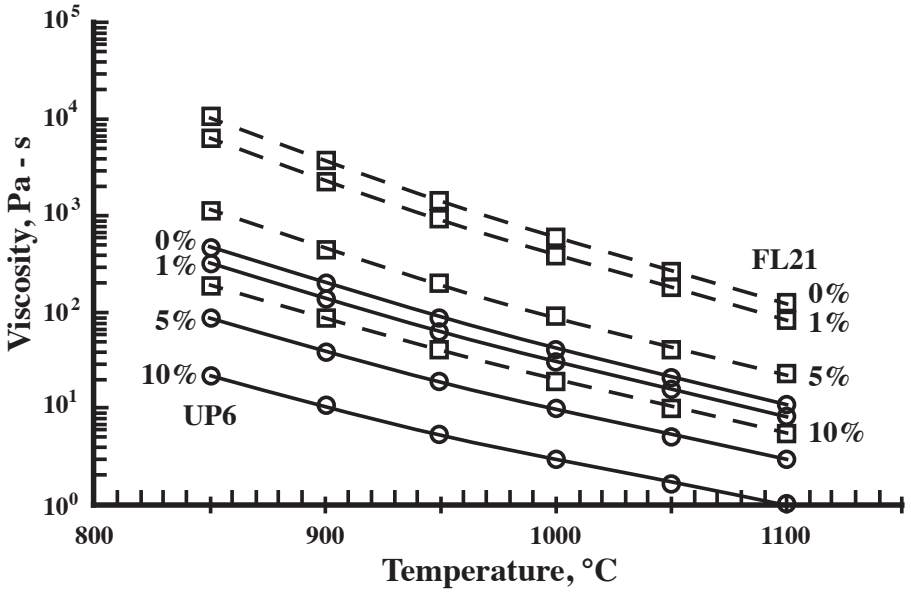

Figure 7. Calculated viscosity of a chilled margin sample (UP6, circles) and a sample of the main magma body (FL21, squares). FL21 is the most silicic of the samples analyzed. Percentage values indicate the mol.% of dissolved H_2O. Viscosity varies over about 4 orders of magnitude, and averages near 100 Pa-s at intermediate temperatures and H_2O content.

Estimates of Yield Strength and Magma Viscosity

The model of Bingham trapping of xenoliths in a magma presupposes that the yield strength of the magma is equal to the excess xenolith mass that it can support. It also presupposes that, prior to trapping, relative motion between magma and xenoliths leads to ablation of the xenoliths until the Bingham trapping size is reached. In the case of the Castle Creek pipes, there is clear evidence of partial melting on the exterior of the felsic gneiss xenoliths, and that melt and fragments of xenoliths have been incorporated in the magma. There is also clear petrographic evidence of interaction between the mafic xenoliths and the host magma. Thus, observational and geochemical evidence suggests that ablation of the felsic xenoliths, at least, occurred during xenolith transport.

The value of the viscosity, ηl, can be calculated from the chemical composition of the chilled margin of the pipes. This viscosity applies to the least contaminated, anhydrous, single-phase melt that existed before crystallization began, and is a minimum estimate of the effective viscosity of the magma at the time of xenolith capture. Additional calculations of viscosity, over a range of temperature and using a range of water contents, and the chemical composition of the main volume of the Castle Creek pipes, show that the viscosity of the magma could have varied over four orders of magnitude (fig. 7). There is no simple way to estimate the viscosity of the multi-phase, liquid + solid ± vapor magma that was actually involved in xenolith transport, but tests of the sensitivity of the yield strength calculation to variations in effective viscosity over the range 1–500 Pa-s show that viscosity is not a major control.

Using an ideal spherical geometry, the viscosity, and the xenolith and magma densities calculated above, we can estimate the yield strength of the Castle Creek magma from the minimum xenolith sizes. For the felsic gneisses, there is a break in the xenolith size distribution near 10 cm (diameter; fig. 5); for the mafic xenoliths, there is a continuum of sizes that merges, at the low end, with the sizes of individual xenocrysts or phenocrysts, at about 1 cm. The best constraint on yield strength, then, is from the felsic xenoliths, and these suggest a value that is <20 Pa (fig. 8) for xenolith radius <5 cm. For mafic xenoliths of radius = 1 cm, a similar yield strength can be calculated for a density contrast of 600 kg/m^3. The size distribution of felsic xenoliths indicates that r = 2.5 cm is smaller than the Bingham trapping size, and figure 8 suggests that yield strengths >50 Pa are probably not realistic. Among the mafic xenoliths, only those smaller than about 2–3 cm are common, and a 2-cm radius is larger than the inferred Bingham trapping size for

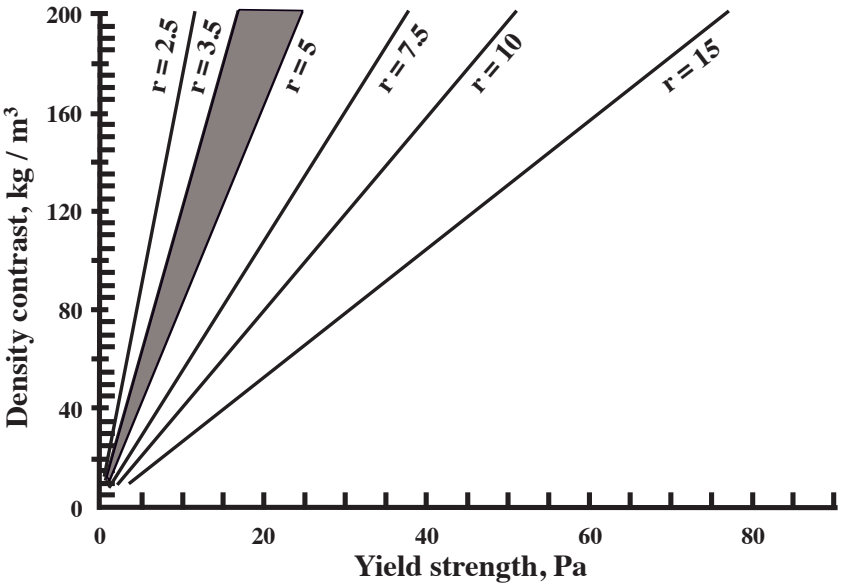

Figure 8. Calculated yield strength for Castle Creek magmas, showing dependence on xenolith radius. The gray field is the expected range for Castle Creek, based on the minimum observed xenolith sizes. The density contrast between magma and xenoliths is a major control.

these. For a range of density contrasts up to 1,200 kg/m^3 and viscosities of 1–500 Pa-s, the mafic xenoliths suggest yield strengths <60 Pa. Because the mafic and felsic xenoliths may have been entrained at different locations along the magma intrusion path, the yield strength of the magma at the times of their entrainment could have been different.

The volume of the largest xenolith is 0.677 m^3, and, for a density of 2,650 kg/m^3, has a mass of ~1,800 kg. An equivalent volume of magma, assuming a density of 2,500 kg/m^3, has a mass of 1,692 kg, so that the excess mass of the largest xenolith being transported by the magma is ~108 kg. By contrast, the excess mass of a xenolith captured by Bingham trapping (r = 5 cm) is ~0.08 kg (fig. 9). Magma yield strength thus plays an insignificant role in the transport of the largest xenoliths. The upward transport of the largest xenoliths was primarily by kinetic energy of intrusion; the felsic gneisses are not neutrally buoyant, nor does yield strength support their excess mass.

Additional Interpretations Based on Xenoliths: Transit Time and Magma Flux

Two constraints allow an estimation of xenolith transit time. The first is the approximation that the Archean gneiss xenoliths were transported at least 4 km upward.

The second constraint derives from the observation that some partial melting has occurred within the granitic gneiss xenoliths to depths of about 10 cm, but that no melt has been observed in sections taken more than 10 cm from the xenolith margins. For an assumed initial magma temperature of 1,150°C at the time of xenolith trapping, and for an assumed xenolith melting temperature of 750°C (i.e., near the granite solidus in a water-undersaturated system), the time required for the xenolith margins to reach the melting temperature by conductive heating is about 4 days. The xenolith ascent rate, then, is about 1 cm/sec, and presumably, the magma ascent rate is somewhat greater. This estimate is sensitive to the assumed thermal conductivity (k) of the xenoliths; for k ~ 10^{-6} J/cm-sec-°C, conductive heating brings the margins of the xenoliths to 750°C in about 4 days, whereas, for k ~ 10^{-5} J/cm-sec-°C, the xenolith margins reach 750°C in about 10 h. The estimate is also sensitive to the assumed initial starting temperature of the xenoliths.

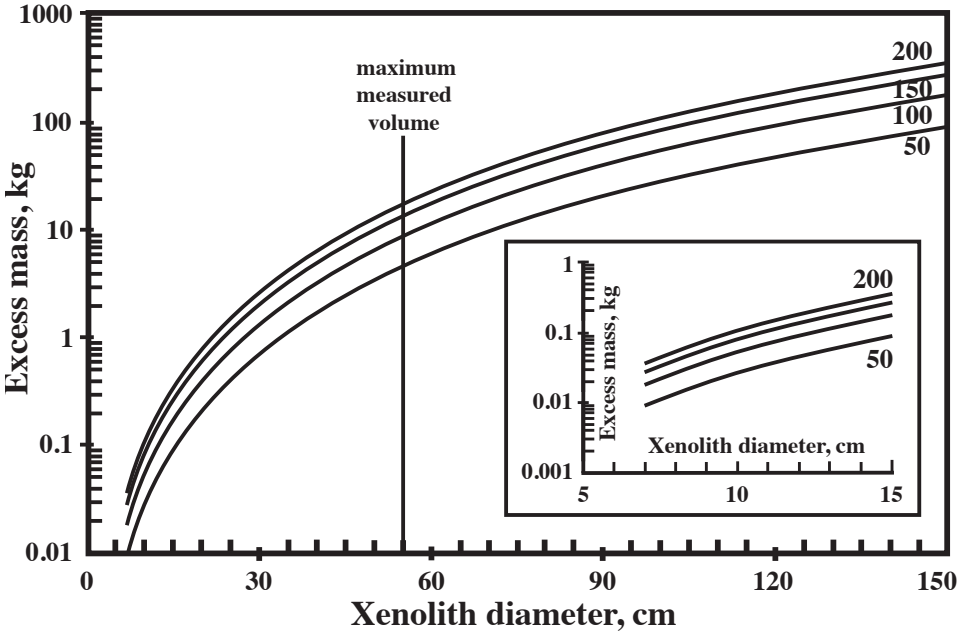

Figure 9. Plot of excess mass of xenoliths as a function of xenolith size. Model calculations are for spherical nodules. The maximum measured volume for any of the xenoliths is equivalent to that of a sphere of diameter 55 cm, though the xenoliths have maximum dimensions up to 142 cm. Density contrast between the magma and the xenoliths is contoured in kg/m^3. The inset shows the range of excess masses for small xenoliths.

For the 4-day transit time, the initial temperature of the xenoliths at the time of entrainment was assumed to be 75°C (a geotherm of ~12°C/km). The maximum possible xenolith temperature at entrainment could be near 400°C, i.e., approximately the brittle–ductile transition, above which fragmentation to form xenoliths might be unlikely; such an elevated temperature would suggest a significantly deeper source. Higher initial temperatures would decrease estimates of transit time, while increasing transit distance. Finally, these calculations assume conductive heating only, whereas the Bingham trapping model assumes that there is continuous advection of new magma to the xenolith margins—there is relative motion between xenoliths and magma—so that the conductive heating model yields a maximum possible transit time. If we assume a fast transit time that might be consistent with k ~ 10^{-5} J/cm-sec-°C, then the xenolith ascent rate would be near 10 cm/sec. The range of these estimates (1–10 cm/sec) is compatible with, but on the low end of, ascent rates calculated for mafic and ultramafic xenoliths in other alkalic magmas (Spera, 1984; Sachs and Stange, 1993).

There is no good constraint on the maximum possible depth of the source of the gneiss xenoliths. Their phase assemblage is not amenable to geobarometry. The garnets that are present, typically in trace amounts, are interpreted not to indicate elevated pressure, but rather are similar to garnets that occur in aluminous, S-type granitic rocks. The transit time is thus, at best, an order-of-magnitude estimate.

The mapped area of the pipes is approximately 3,000 m^2. For magma densities in the range 2,500–2,620 kg/m^3 and an assumed magma ascent rate of 1 cm/sec, the mass flux through the pipes is about 90,000 kg/sec. This is a lower bound because the magma ascent rate could be an order of magnitude greater. For an ascent rate of 1 cm/sec, it is likely that magma flow was laminar (Reynolds number <10). Even at an ascent rate of about 10 cm/sec, it is likely that the magma flow was in a transitional, and not fully turbulent, flow regime. This is consistent with the observed compositional heterogeneity, the poor mixing of the main mass of the pipes.

Unresolved Issues

Prior work (Sachs and Stange, 1993) suggests that felsic xenoliths can be preserved only in magmas of high viscosity, high yield strength, and high ascent velocities. They model xenolith transport from >15 km, with maximum xenolith sizes <40 cm, and minimum ascent velocities >0.5 m/s. For the Castle Creek xenoliths, preservation might reflect their shallower source and consequently low initial temperature, their larger initial size, and the mismatch between conductive heating—used here to estimate the time required for partial melting to 10 cm depth within the xenoliths—and more rapid advection of heat in a dynamic magma system. Short transit times militate against extensive melting of xenoliths, and geochemical data that suggest up to 40% of the host magma derives from assimilation are not consistent with a short transit time. Because such extensive assimilation also results in cooling and progressive crystallization of the host magma, and both cooling and crystallization increase viscosity, assimilation militates against high ascent velocity. In fact, the thermal balance of assimilation suggests that a magma cannot assimilate more than about 50% of its own mass (McBirney, 1979) before freezing. Thus, for the Castle Creek magma, the geochemical inference of the extent of assimilation suggests that the magma froze in its present location because of "heat death" due to assimilation.

Sparks and others (1977) show measured yield strengths of 70–400 Pa in basaltic magmas (their table 1), well above the range suggested by this study. Sparks and others also note that Bingham fluids can support an excess mass that is 5–7 times their yield strength. This suggests that, at Castle Creek, the break in the felsic xenolith size distribution should be above 20 cm. The xenolith size distribution at Castle Creek, if it reflects progressive ablation of the xenoliths, thus constrains the yield strength to relatively low values, and conflicts with the laboratory experiments that suggest that a much larger excess mass can be supported.

SECTION 2: CLINOPYROXENITE AND PERIDOTITE XENOLITHS

This section deals with peridotite and clinopyroxenite xenoliths that occur in a small MNS plug west of the Cottonwood Creek road (fig. 1). The xenolith-bearing plug is in the core of a larger intrusion, where the larger, surrounding MNS body contains no xenoliths. Though the host MNS is similar to that at Gordon Butte to the east (table 6), there is no obvious connection between the intrusions; the next small hill to the north, however, is on strike with a dike that radiates

Table 6. Chemical compositions and CIPW norms of selected MNS, Cottonwood Creek and Gordon Butte.

	COTTONWOOD CREEK		GORDON BUTTE			COTTONWOOD CREEK		GORDON BUTTE	
	CT-1 (data in wt. %)	CT-2	GB-36 chill zone	GB-61 main sill		CT-1 (data in ppm)	CT-2	GB-36 chill zone	GB-61 main sill
SiO_2	49.80	48.60	46.30	46.10	Rb	65.4	70	61.7	75
TiO_2	0.97	1.03	0.98	1.04	Sr	3335	3500	4100	3450
Al_2O_3	13.30	12.20	14.20	13.70	Ba	4600	4250	5950	3900
Fe_2O_3(T)	8.60	9.39	9.73	9.65	Y			40	40
MnO	0.15	0.15	0.18	0.17	Zr	230	190	280	240
MgO	6.52	6.95	5.05	6.19	Nb			85	55
CaO	10.20	11.00	9.13	10.80	Sc			12.7	16.73
Na_2O	4.74	4.27	6.72	5.27	Cr	120	125	50	100
K_2O	3.86	3.61	4.92	3.23	Co			29.3	31.7
P_2O_5	1.19	1.36	1.42	1.36	Ni	70	60	35	50
					Cu	104	87	135	105
Total	99.33	98.56	98.63	97.51	Zn	110	135	210	110
					Cs			2.06	1.39
CIPW Norms (wt. %)					Be			7.3	6.2
or	22.82	21.34	6.74	19.09	Hf			9.98	8.68
ab	9.54	7.78		2.88	Ta			4.23	1.99
an	3.61	3.45		4.18	Sb			0.12	0.105
ne	16.56	15.36	24.72	22.60	Th			45.2	29.9
lc			17.52		U			5.9	5.8
ns			1.14		La			326	255
ac			5.57		Ce			591	463
					Nd	179		221	185
fo	4.31	4.58	3.33	3.89	Sm	25.79		30.17	26.22
fa	2.68	2.94	3.38	2.89	Eu			7.10	6.42
					Tb			1.68	1.58
di	21.78	23.26	16.90	21.30	Yb			2.21	2.06
hd	10.71	11.80	13.59	12.51	Lu			0.307	0.283
mt	2.18	2.34		2.43					
ilm	1.84	1.96	1.86	1.98					
ap	2.60	2.97	3.10	2.97					

from the butte. Xenoliths range up to ~15 cm, and are predominantly clinopyroxenites, with some containing prominent biotite and apatite, and rarely olivine. No other minerals occur consistently in the clinopyroxenites. Peridotites are rare and typically smaller than 5 cm, and contain clinopyroxene, biotite, and chromite in addition to olivine. In thin section, the MNS shows quench textures along the contacts of some clinopyroxenites, indicating that the xenoliths were cooler than the magma liquidus at the time of entrapment. Many of the xenoliths are coated with biotite (fig. 10A). A few centimeter-sized xenocrysts of olivine, clinopyroxene, and biotite have also been found.

The clinopyroxenite xenoliths mostly have equigranular mosaic textures, and range from coarse (fig.

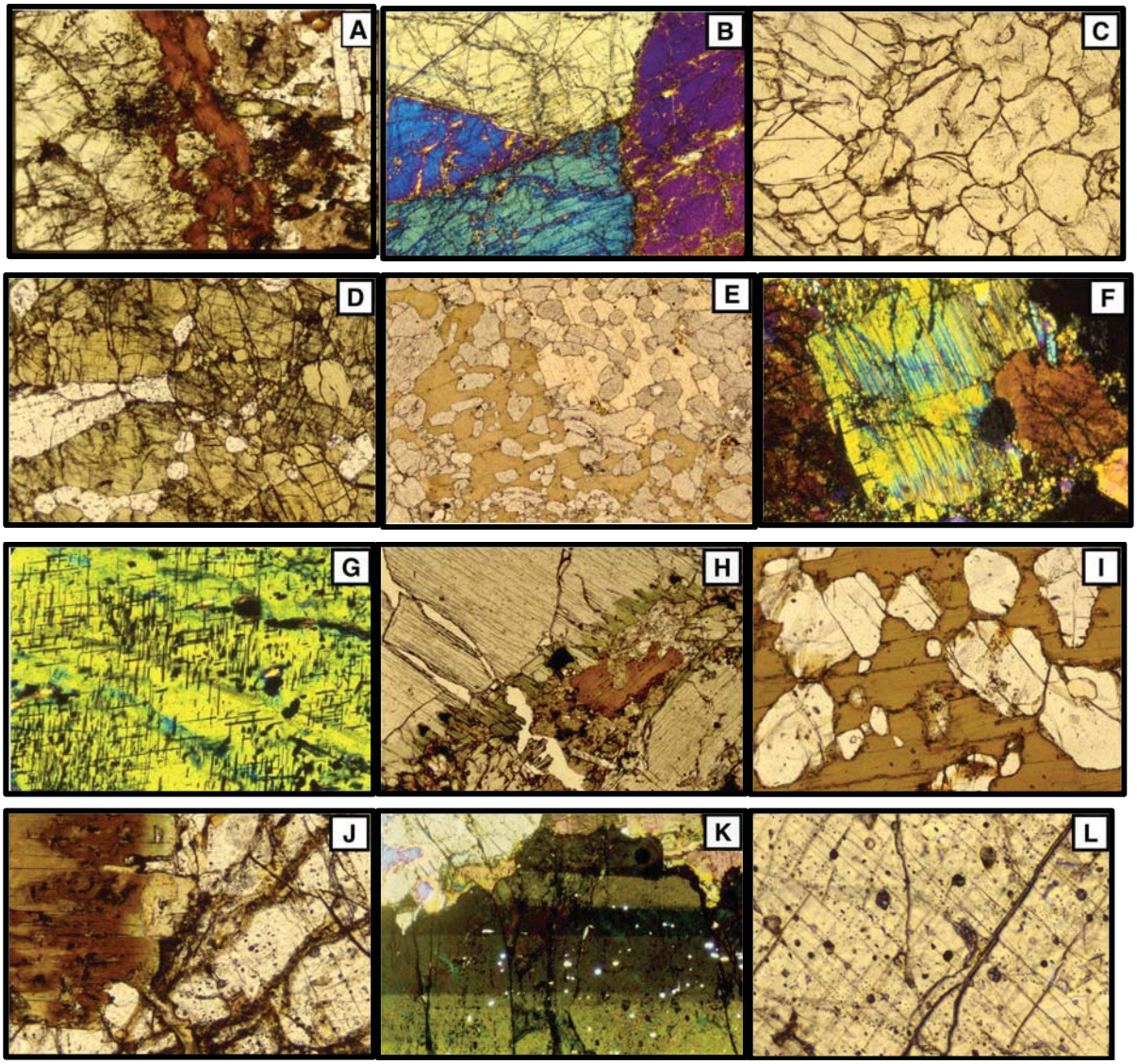

Figure 10. Photomicrographs of xenoliths from the Cottonwood Creek location. Images are 2.2 mm horizontally unless noted. A, Sample CT10A-2X. Biotite rims many clinopyroxenites; clinopyroxenite at left, host magma at right. B, Sample CT10B-2X. Coarse-grained clinopyroxenite. Crossed polarizers. C, Sample CT49-1X. Fine-grained clinopyroxenite. D, Sample CT9-4X. Porphyroclastic, apatite-rich clinopyroxenite. E, Sample CT53X. Coarse, oikocrystic biotite enclosing clinopyroxene. F, Sample CT9-4X. Exsolution in clinopyroxene occurs only in porphyroclastic xenoliths. Crossed polarizers. Image is 1 mm horizontally. G, Sample CT50X. Oxide exsolution in clinopyroxene. Crossed polarizers. Image is 0.7 mm horizontally. H, Sample CT5X. Clinopyroxene megacryst with a reaction rim of aegirine along the contact with enclosing MNS. I, Sample CT45X. Oikocrystic biotite enclosing olivine. J, Sample CT45X. Reversely pleochroic phlogopite forms light greenish margins on normally pleochroic, dark phlogopite. Image is 1 mm horizontally. K, Sample CT49-2X. Stress twinning in olivine. Crossed polarizers. Image is 1 mm horizontally. L, Sample CT45X. Fluid inclusions in clinopyroxene. Image is 0.7 mm horizontally.

10B; grain size 5 mm or larger) to fine-grained (fig. 10C). A few have slightly porphyroclastic texture with a range of grain sizes (fig. 10D). There is some suggestion of bands with accumulated apatite in the apatite-rich samples. Biotite is usually scattered throughout the xenoliths, but sometimes forms large oikocrysts surrounding clinopyroxene grains (fig. 10E) that remain in optical continuity.

Mineral Chemistry

A comparison of mineral compositions (table 7) in the xenoliths with those in the MNS helps to assess the relationship between the xenoliths and their host. The analyses selected for table 7 emphasize the range of compositions that occurs in each sample group. In the least fractionated MNS (AP4), phenocryst olivine contains ~90% Fo, whereas a cumulate sample upsection in the same intrusion (AP12) contains a fractionated composition with ~75% Fo. Other cumulate MNS samples (e.g., BB15) can have olivine phenocrysts with Fo up to 94%. Xenocrystic olivine in MNS is distinguishable from phenocrysts because it usually has a reaction rim of phlogopite around it. These xenocrysts are less magnesian, with Fo between 87% and 90%.

Table 7. Chemical compositions of minerals in MNS, xenoliths, and megacrysts from the Crazy Mountains.

	OLIVINE PHENOCRYSTS IN MNS			XENOCRYSTS IN MNS		PERIDOTITE XENOLITHS			MEGACRYST	PYROXENITE
	AP-4	AP-12	BB-15	GB-61	GB-103	CT8X-2	CT4X-2-1	CT6X-1	CT35X-2	CT45X-1
SiO_2	41.48	38.78	41.57	40.33	40.84	40.05	40.90	41.24	40.82	39.90
Al_2O_3			nd	0.04	0.05				0.04	nd
FeO (T)	9.70	22.15	6.41	11.70	9.98	17.09	12.99	10.06	10.87	15.55
MnO	nd	0.60	0.08	0.20	0.21	0.39	0.15	0.03	0.13	0.30
MgO	49.60	38.28	52.55	46.67	49.13	43.39	47.00	49.51	48.91	45.48
CaO	0.16	0.43	0.05	0.28	0.29	0.18	0.15	0.29	0.28	0.22
P_2O_5	0.06	0.05	nd	nd	nd	0.07	0.07	0.08	nd	nd
Cr_2O_3	nd	nd	0.11	0.07	0.04				0.04	nd
NiO	0.34	0.25	0.39	0.09	0.16	0.13	0.11	0.13	0.09	0.15
Total	101.36	100.53	101.20	99.37	100.76	101.32	101.37	101.30	101.20	101.63
Mg #	0.901	0.755	0.936	0.877	0.898	0.819	0.866	0.898	0.889	0.839

	CLINOPYROXENE PHENOCRYSTS IN MNS				PERIDOTITE XENOLITHS			CLINOPYROXENITE XENOLITHS				MEGACRYST	MEGACRYST
	CT5-2	CT5-4	GB36-1	GB61-4	CT4-2X-2	CT6X-3	CT8X-4	CT9-4X-1	CT9-4X-2	CT10A-1X-4	CT10A-2X-5	CT5X-5 (core)	CT5X-10 (rim)
SiO_2	52.60	51.10	53.02	51.49	54.12	53.66	54.00	49.45	52.16	53.41	52.19	53.11	52.56
TiO_2	0.63	0.80	0.62	0.60	0.18	0.20	0.11	0.69	0.38	0.16	0.34	0.26	1.49
Al_2O_3	1.32	2.05	0.89	2.04	0.67	1.48	1.05	3.97	1.77	1.24	2.21	1.14	0.63
FeO (T)	5.96	5.75	7.52	5.86	3.19	4.48	4.80	9.25	7.72	3.41	5.87	2.69	20.18
MnO	0.18	0.15	0.20	0.14	0.08	0.09	0.15	0.32	0.21	0.11	0.19	0.04	0.34
MgO	14.70	14.75	14.28	14.73	15.95	15.70	16.00	12.79	13.69	16.80	15.24	16.80	5.35
CaO	22.84	23.44	22.32	23.53	23.00	23.05	22.44	22.04	22.29	24.13	22.55	23.61	11.34
Na_2O	0.84	0.65	1.44	0.69	0.78	0.72	0.95	0.66	1.11	0.61	0.72	0.55	7.50
Cr_2O_3	0.03	0.07	nd	nd	0.22	0.20	0.33	0.10	0.04	0.37	0.13	0.87	0.12
NiO	nd	nd	0.14	nd		nd	nd	nd	0.04	nd	0.04		
Total	99.08	98.77	100.42	99.08	98.19	99.57	99.81	99.26	99.42	100.23	99.49	99.07	99.52
Mg#	0.87	0.92	0.90	0.92	0.90	0.86	0.86	0.71	0.76	0.90	0.82		

	BIOTITE PHENOCRYSTS IN MNS				PERIDOTITE XENOLITHS			CLINOPYROXENITE XENOLITHS			
	CT5-1	CT5-2	GB61-3	GB61-4	CT6X-2	CT6X-3	CT6X-6	CT10A-1X-4	CT10A-1X-3	CT10A-1X-6	CT10A-1X-2
SiO_2	35.21	38.36	37.42	35.36	42.56	36.37	42.14	38.74	39.00	38.33	36.73
TiO_2	4.74	4.52	4.02	4.95	nd	4.50	nd	1.57	2.09	3.38	4.14
Al_2O_3	13.14	10.39	8.71	13.05	11.07	12.80	10.50	12.80	14.07	12.65	13.54
FeO (T)	16.59	17.48	22.09	9.56	5.45	9.74	9.69	8.95	7.68	10.13	9.73
MnO	0.38	0.38	0.55	0.13	nd	0.09	0.06	nd	nd	0.03	0.03
MgO	12.97	13.88	10.37	16.57	25.75	18.72	23.31	20.71	21.54	19.22	18.59
Na_2O	0.56	0.52	0.31	0.52	0.30	0.38	0.47	0.21	0.50	0.52	0.50
K_2O	7.68	9.36	9.08	7.51	10.01	8.25	9.49	9.28	9.03	8.82	8.21
Cr_2O_3	nd	nd	nd	nd	nd	0.21	0.04	0.44	0.31	0.17	nd
NiO	0.04	nd	0.03	nd	nd	nd	nd	0.04	nd	0.08	0.05
BaO	3.96	0.56	nd	4.72	nd	3.58	nd	1.09	0.85	1.75	3.14
Total	95.29	95.48	92.59	92.36	95.18	94.64	95.70	93.82	95.08	95.07	94.66
Mg #	0.582	0.586	0.456	0.755	0.894	0.774	0.811	0.805	0.833	0.772	0.773
IV site def.	0.108	0.28	0.332	0.094							

Note. All data in wt.%. Data are averages of 3–6 spots on single grains; blank spaces indicate elements not analyzed; nd, not detected. Mg # for clinopyroxene is calculated after accounting for the acmite component; for olivine and biotite, Mg # is based on total Fe as FeO. Tetrahedral site deficiency for biotite is calculated for 22 cations, and would be equivalent to the tetraferriphlogopite component.

The olivine in peridotite xenoliths and xenocrysts from the Cottonwood Creek location varies between 82% and 90% Fo. In the single clinopyroxenite in which olivine was analyzed, the olivine has Fo ~84%. The xenolithic olivines thus are somewhat more fractionated than the phenocrysts of the least fractionated MNS. Many of the olivines contain >0.2 wt.% CaO, but have NiO <0.4 wt.%, clearly indicating that they are not derived from typical lherzolitic mantle. The olivine in clinopyroxene-rich xenoliths sometimes shows stress-twinning (fig. 10K), and some olivines also contain fluid inclusions (fig. 10L).

Clinopyroxene phenocrysts in the MNS are commonly optically zoned and contain melt or fluid inclusions, whereas those in the xenoliths are not zoned (Figs. 10B–10E), and are mostly free of inclusions. In a few xenoliths, clinopyroxene shows exsolution of a second pyroxene (fig. 10F), or of an oxide phase (fig. 10G) that could be Ti-Cr-magnetite or rutile. Exsolution has not been observed in the clinopyroxene phenocrysts of the MNS. Clinopyroxene in the MNS is diopsidic, with low TiO_2 (mostly <1 wt.%), Al_2O_3 (all analyses <4 wt.%), and Cr_2O_3 (typically <0.2 wt.%), but moderate Na_2O (mostly 0.5 wt.% and above), tending to aegirine at the rims. Analysis of a clinopyroxene megacryst (CT5X) from the Cottonwood Creek location shows a core that is relatively Cr-rich (0.87 wt.% Cr_2O_3) and magnesian, and a reaction rim that is aegirine (fig. 10H; 7.5 wt.% Na_2O). This clearly shows that at the time of entrainment, the clinopyroxene was not in equilibrium with the host magma.

Clinopyroxene in the peridotite xenoliths generally contains lower TiO_2 and Al_2O_3 than the MNS phenocrysts, but higher Cr_2O_3; Na_2O is relatively high in the peridotite clinopyroxenes (0.7–1.0 wt.%). Clinopyroxenes in all xenoliths are dominantly diopsides. In the clinopyroxenite xenoliths, TiO_2 tends to be lower and Al_2O_3 to be higher than it is in the MNS phenocrysts, and the xenolithic pyroxenes also have generally lower Mg numbers.

The dark mica in the MNS is highly variable. Most compositions fall into the biotite field ($Mg/(Mg^+Fe^{2+})$ <0.67), but are unusual in having high TiO_2 (many analyses with TiO_2 >4 wt.%) and BaO (up to 5 wt.%). Biotite is used here as a general term for the dark micas, though some compositions do fall in the phlogopite field. The F^- and Cl^- contents were not determined, but whole rock analyses suggest that the halogens may be important constituents, and this affects the interpretation of compositional variation. The biotites appear deficient in tetrahedrally coordinated (Si + Al) cations, and both optical features (reverse pleochroism: fig. 10J) and chemical analyses indicate that a tetraferriphlogopite component is present. The dark micas formed as reaction rims on olivine are commonly reversely pleochroic. Oikocrystic biotite can envelop olivine (fig. 10I) or clinopyroxene (fig. 10E). In the peridotite xenoliths, the micas are all phlogopitic, but include two compositional groups: one group, with elevated TiO_2 and BaO, is similar to biotites in the MNS, whereas TiO_2 and BaO are not detectable in the other group. This suggests that the peridotites contained phlogopite before they were entrained in, and reacted with, the MNS magma: there is evidence of two episodes of metasomatism of the peridotites. Biotites in the clinopyroxenites are similar to those in the MNS in many features, but are more magnesian, and are mostly phlogopites.

Bulk Xenolith Compositions

Table 8 presents major and trace element data for the xenoliths, and table 9 presents isotopic data. The peridotites contain 50–88 norm % olivine, with most of the balance being clinopyroxene. None of the analyzed samples contains sufficient silica to stabilize orthopyroxene, and the large ion lithophile elements (LILE) that occur in modal mica are present as nepheline and leucite in the peridotite norms. Though both Cr and Ni are slightly elevated, the compatible trace element content of the peridotites is well below that usually found in mantle lherzolites. The incompatible trace element content of the peridotites is also elevated, indicating that the peridotites derive either from a cumulate zone related to the alkaline magmatism of the Crazy Mountains, or from a metasomatized source within the mantle.

The clinopyroxenites contain varying proportions of clinopyroxene, biotite, and apatite, and this variation is reflected in their chemical compositions. The cleanest clinopyroxenites contain almost 90 norm % clinopyroxene (CT1CX), whereas those with abundant biotite and apatite (CT10A1X) contain as little as 55 norm % clinopyroxene. Though the modal amount of apatite approaches 15% in some samples, among those analyzed, the maximum apatite content is only 6.4 norm %. These mineralogical controls are reflected in the trace element data as well. The clean clinopy-

Table 8. Geochemical data and norms for Cottonwood Creek xenoliths.

	Peridotites			**Clinopyroxenites**			
	CT4-2X	CT6X	CT8X	CT1CX	CT9-4X	CT10A1X	CT10A2X
	(data in wt.%)						
SiO_2	44.30	40.40	40.50	52.60	47.90	48.50	51.40
TiO_2	0.26	0.26	0.16	0.45	0.43	0.80	0.37
Al_2O_3	1.90	1.78	1.19	2.60	3.03	6.24	3.17
Fe_2O_3 (T)				6.98			
FeO	8.12	9.77	14.20		4.10	4.52	3.68
Fe_2O_3	1.82	1.13	0.92		3.85	3.05	2.98
MnO	0.28	0.26	0.42	0.14	0.19	0.14	0.14
MgO	29.70	42.90	38.90	14.70	12.20	15.10	15.00
CaO	11.20	1.84	2.96	23.00	23.90	15.40	21.90
Na_2O	0.35	0.13	0.10	1.26	1.47	1.39	1.11
K_2O	0.68	0.86	0.61	0.13	0.35	2.83	0.29
P_2O_5	0.09	0.17	0.05	0.10	2.91	0.70	0.13
Total	98.70	99.50	100.01	101.96	100.33	98.67	100.17
CIPW Norm (wt. %)							
or				0.77	1.36	8.12	1.71
ab				0.55			0.09
an	1.60	1.73	1.00	1.05	0.63	2.43	2.81
ne	1.60	0.60	0.46	5.48	6.74	6.37	5.04
lc	3.15	3.99	2.83		0.56	6.75	
cs	2.44	1.42	1.19				
fo	41.88	74.48	65.90	0.78	0.09	11.24	3.06
fa	9.43	13.94	19.11	0.16	0.03	2.74	0.66
di	30.69	1.25	6.19	76.60	65.30	46.54	71.19
hd	5.46	0.19	1.42	12.51	15.09	8.97	12.12
mt	1.70	0.99	1.52	2.45	3.19	2.31	2.36
il	0.49	0.49	0.30	0.85	0.82	1.52	0.70
ap	0.20	0.37	0.11	0.22	6.36	1.53	0.28
	(data in ppm)						
Sc		7.13	8.63	67.6	35.5	37.1	66.7
Cr	1350	490	165	220	100	1720	650
Co		121	153	33.6	41.6	41.1	36.4
Ni	325	730	505	100	50	165	100
Cu	27	42	26	35	195	11	26
Zn	125	125	175	60	65	75	45
Rb	15.9	56.6	31.9	7.8	10.5	75.9	15.8
Cs		1.44	2.02	0.12	0.23	1.19	0.66
Sr	458	301	183	995	2215	1375	735
Ba	1110	2200	1125	230	1200	4100	420
Y	12	12	8			30	
Zr	90	70	70	110	35	140	50
Hf		0.92	0.46	2.45	3.64	2.83	1.46
Ta		0.32	0.15	0.15	0.31	0.59	0.226
Th		2.37	1.42	1.39	8.1	4.68	2.17
U		1.1	0.65	<0.4	0.9	1.47	0.8
La		24.7	11.3	37	206	82.7	26.3
Ce		44.9	22.4	88	414	172	65
Nd		18.6	10.6	52.1	199	86.5	43.6
Sm		2.69	1.61	8.88	28.28	12.3	7.63
Eu		0.648	0.418	2.39	6.87	3.01	2
Tb		0.153	0.09	0.58	1.6	0.73	0.52
Yb		0.28	0.25	0.86	1.77	1.12	0.88
Lu		0.037	0.033	0.111	0.241	0.148	0.106

Table 9. Isotopic data for Cottonwood Creek samples.

		Rb	Sr	$^{87}Rb / ^{86}Sr$	$^{87}Sr / ^{86}Sr$ (m)	$^{87}Sr / ^{86}Sr$ (i)	Sm	Nd	$^{147}Sm / ^{144}Nd$	$^{143}Nd / ^{144}Nd$ (m)	$^{143}Nd / ^{144}Nd$ (i)
Host Rock	CT1	65.4	3335	0.0568	0.705684	0.705644	25.79	178.6	0.0831	0.511820	0.511793
	GB36	61.7	4100	0.0435	0.705759	0.705728	30.17	221.2	0.0824	0.511920	0.511893
	GB61	75.2	3455	0.0629	0.705689	0.705644	26.22	185.3	0.0855	0.511959	0.511931
Peridotites	CT4-2X	15.9	458	0.1002	0.705811	0.705740					
	CT6X	56.6	301	0.5438	0.705771	0.705385					
	CT8X	31.9	183	0.5043	0.705919	0.705561	1.61	10.6	0.0929	0.511861	0.511831
Clinopyroxenites	CT1CX	7.80	995	0.0224	0.705684	0.705668	8.88	52.1	0.1031	0.511909	0.511875
	CT9-4X	10.5	2215	0.0136	0.705828	0.705818	28.28	199	0.0860	0.511971	0.511943
	CT10A1X	75.9	1375	0.1599	0.705861	0.705747					
	CT10A2X	15.8	735	0.0620	0.706395	0.706351	7.63	43.6	0.1057	0.511772	0.511737
Cpx Mega	CT5X	0.97	425	0.0066	0.705355	0.705350	5.55	30.1	0.1116	0.512002	0.511966
Bio Mega	CT39X	341	306	3.227	0.707765	0.705473					

roxenite has relatively low concentrations of Sr, Ba, and REE, whereas the apatite- and biotite-rich samples have enrichments of Sr and REE, and Ba, respectively. Enrichments of Cr and Ni, and HFSE do not follow a clear pattern.

The Sr and Nd isotopic data have been corrected to 50 Ma, the approximate age of intrusion. Both Sr and Nd isotopic values vary outside of expected analytical uncertainty (± 0.000030 2σ, for both Sr and Nd), and though there is overlap between the isotopic compositions of the host rocks and xenoliths (fig. 11), the data are not tightly clustered. The errorchron connecting Sr isotopic compositions of the clinopyroxene (CT5X) and biotite (CT39X) megacrysts yields an age of approximately 52 Ma; the peridotite CT6X falls on the same line.

Discussion

The correspondence between the Sr isotopic age of the megacrysts and the independently determined age of alkaline magmatism in the Crazy Mountains anchors this discussion of the xenoliths at the Cottonwood Creek location. Assuming that the megacrysts are dismembered fragments of rocks coming from the same source as the xenoliths (Righter and Carmichael, 1993), the age correspondence shows that the xenoliths are part of the same magma system as the MNS intrusions that host them. They are not fragments derived from an older magma system, nor from the underlying mantle. The distinctions in composition—both trace element (fig. 12) and isotopic composition (fig. 11)—however, indicate that the xenoliths are not cognate, in the strict sense, with the magma hosting them. The best interpretation is that the clinopyroxenite xenoliths and the olivine, clinopyroxene, and biotite megacrysts are samples of cumulates formed at depth from magmas similar to the MNS at the Cottonwood Creek location. The magmas parental to the clinopyroxenites in some cases, unlike the Cottonwood Creek MNS, were in equilibrium with olivine and generated cumulates containing olivine in addition to clinopyroxene, whereas others were more fractionated, and yielded clinopyroxenes with lower Mg numbers than those in the host Cottonwood Creek MNS.

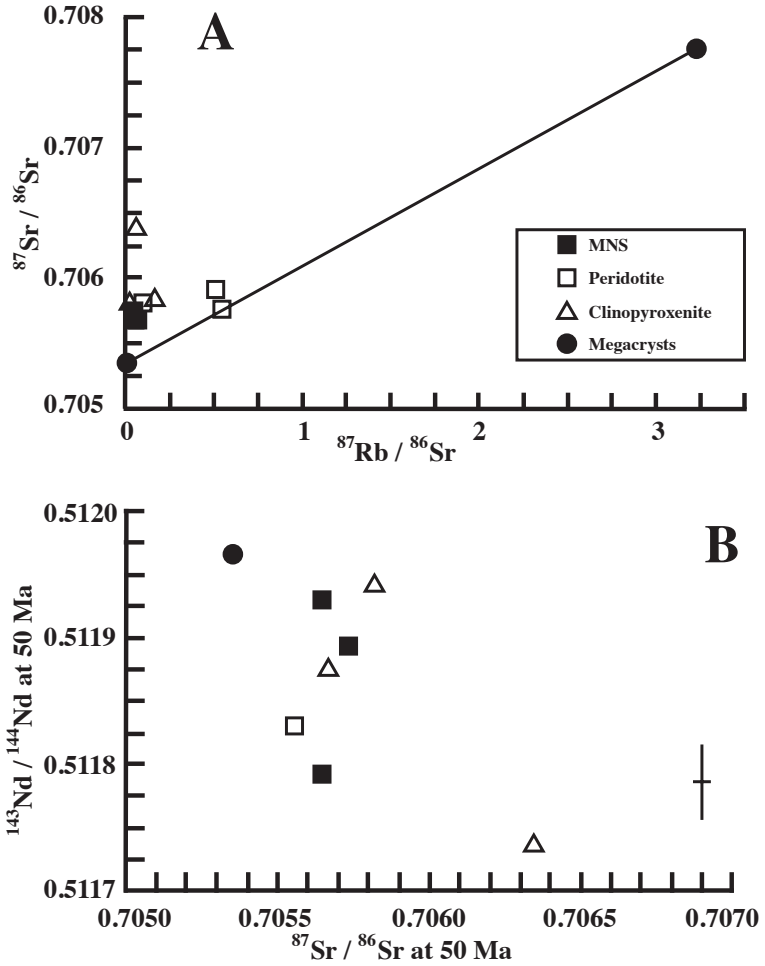

Figure 11. Radiogenic isotopic data for Crazy Mountains MNS and Cottonwood Creek xenoliths. A, $^{87}Rb/^{86}Sr$ vs. measured $^{87}Sr/^{86}Sr$ data.The data are not colinear, and xenoliths and host rocks have a range of compositions. The line connects megacrysts of biotite and clinopyroxene, and yields an approximate age of 52 Ma. B, Sr and Nd isotopic data corrected to 50 Ma. Both Sr and Nd vary outside of analytical uncertainty, indicating that the host rocks and xenoliths are not strictly cognate. 2σ analytical uncertainty is shown at right.

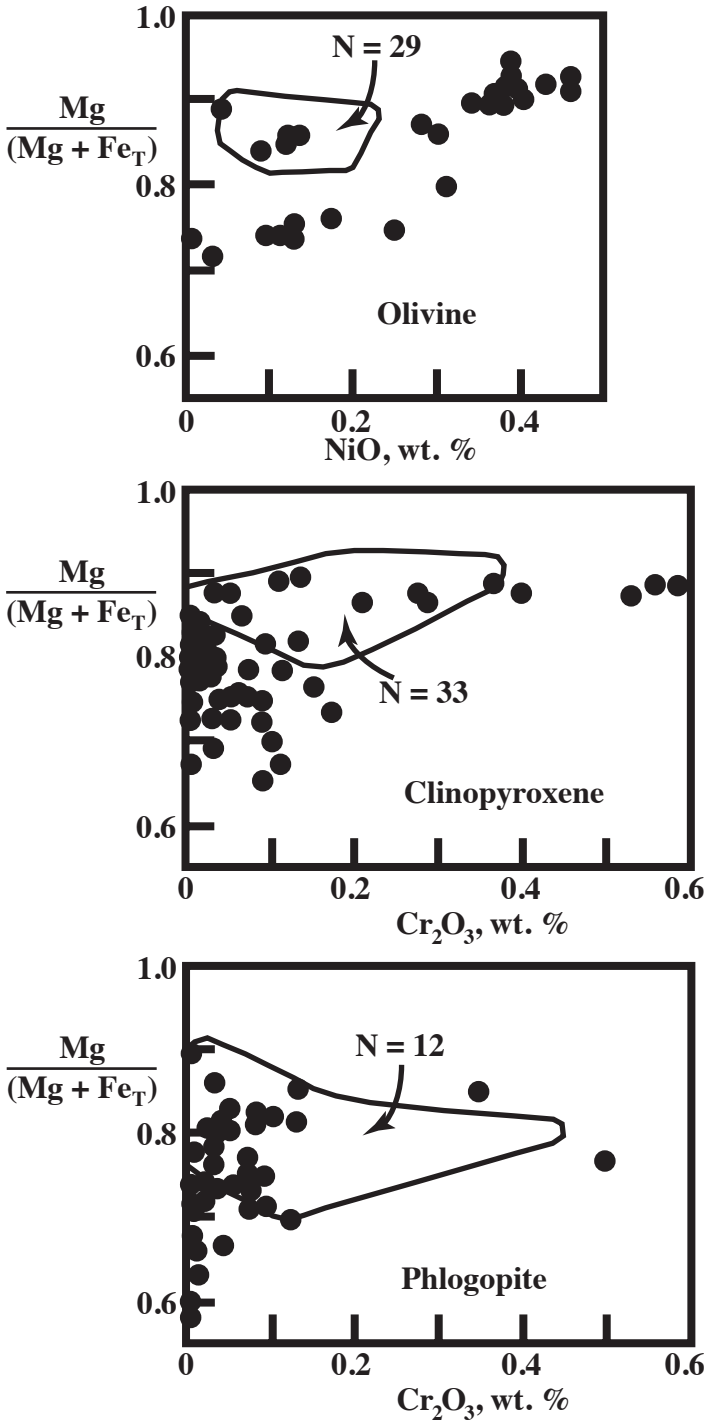

Figure 12. NiO and Cr_2O_3 concentrations in xenolith minerals are different from those in most MNS phenocrysts. Data from xenoliths are in the enclosed fields.

In many mantle-derived xenoliths, grain-boundary enrichment has produced enriched trace element profiles. In the case of these xenoliths, the enrichment appears not to be a grain-boundary phenomenon. The core of the clinopyroxene megacryst CT5X was sampled and analyzed for Sr and Nd concentrations and isotopic compositions. The Nd and Sm content of CT5X are near the maximum ever recorded for clinopyroxene, Ba, Sr, and Nd are about 20 times the primitive mantle concentration, and Rb and K are almost the same as in primitive mantle. These observations suggest that the clinopyroxenites are cumulates from alkaline magmas.

The relation of the peridotites to the clinopyroxenites is not clear. In particular, the occurrence of TiO_2- and BaO-free phlogopites in the peridotites indicates clearly that these xenoliths have a history separate from the MNS magmas, and that the distinction between olivine-bearing clinopyroxenites and olivine megacrysts on the one hand, and peridotites on the other, is not merely one of differing proportions of major phases.

The mineral assemblage in the clinopyroxenites and peridotites is not amenable to precise geothermometry and geobarometry. The variation of CaO in

olivine has been calibrated as a geobarometer (Adams and Bishop, 1986; Finnerty and Boyd, 1978). Figure 13 shows an interpretation of the Adams and Bishop calibration, contoured for CaO content. Among the peridotite xenoliths, the lowest measured CaO content was in CT4-2X, at 0.13–0.17 wt.%. The intersection of these CaO isopleths with the extrapolated liquidus of the least fractionated MNS (AP4) provides an estimate of both temperature (1,100–1,150°C) and pressure (10–16 kb) for olivine crystallization. The mantle–crust boundary in this part of Montana (~55 km depth; McCamy and Meyer, 1964) lies near the maximum estimated pressure preserved in peridotitic olivine, suggesting that the peridotite xenoliths were entrained near the mantle–crust boundary. The entrainment of these xenoliths in a strongly alkalic and relatively fractionated magma (it bears no olivine phenocrysts) then requires that MNS magmas formed and fractionated at mantle depth. Rapid rise of magma to the surface is required to transport the mafic xenoliths, so that fractionation along the intrusion path is probably not an important process.

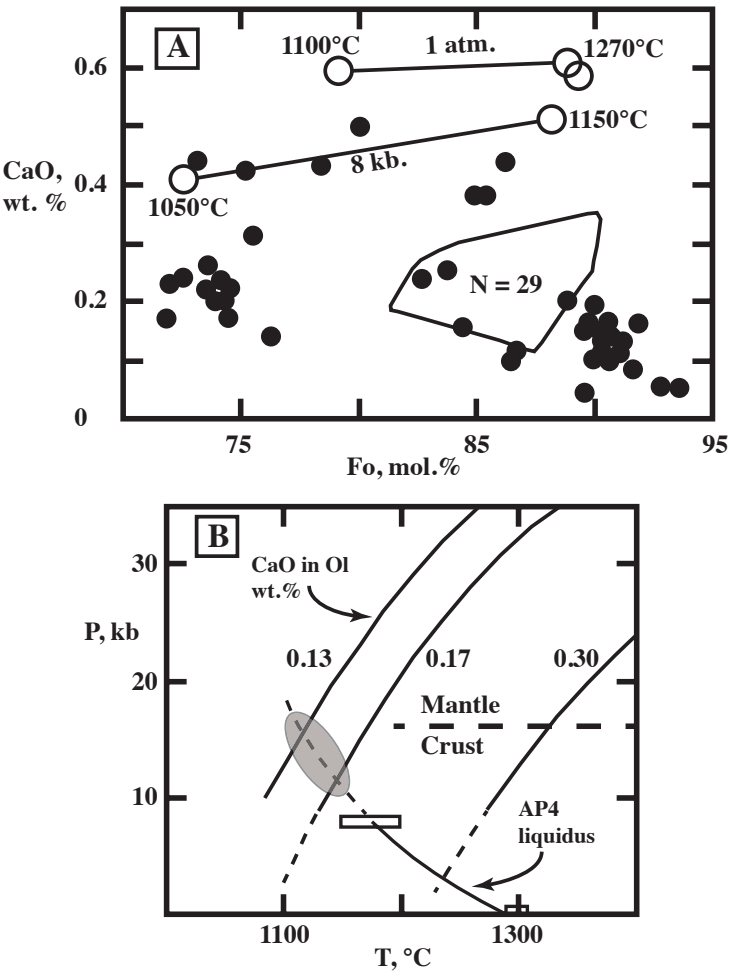

Figure 13. A, Data for CaO content in olivine. The enclosed field contains 29 analyses of olivine in peridotites. Solid circles are data for phenocrysts in MNS. Open circles are data from melting and crystallization experiments on AP4, the least fractionated MNS in the Crazy Mountains. B, Constraints on depth of peridotite xenolith equilibration. Isopleths of CaO content in olivine derive from data in Adams and Bishop (1986). The approximate pressure at the mantle–crust boundary (depth ~55 km; McCamy and Meyer, 1964) is shown at right. The liquidus of the least fractionated MNS from the Crazy Mountains (AP4) is constrained by experiments at 1 atm and 8 kb, and is extrapolated to meet the CaO-in-olivine isopleths. The shaded area is the potential range of T and P for olivine equilibration.

SUMMARY

Two locations in the northern Crazy Mountains, Castle Creek and Cottonwood Creek, have abundant xenoliths hosted by Eocene alkaline rocks that are part of the Central Montana Igneous Province. At Castle Creek, a census of xenoliths by lithology and size shows that 85% of the xenoliths are felsic gneisses; the xenoliths range from 7 to 142 cm in maximum dimension, and up to 0.68 m^3 in volume. Chemical data indicate that the host magma is monzonitic, and contains 15–40 wt.% admixture of material from the felsic xenoliths. There is also textural evidence of partial melting and disaggregation of the xenoliths, supporting the idea that the xenolith size distribution, particularly the size cut-off at 7 cm, is due to progressive ablation of the xenoliths. Calculations based on a Bingham trapping model, over a range of values for density contrast (10–200 kg/m^3), viscosity (1–500 Pa-s), and xenolith radius (2.5–20 cm), show that the yield strength of the magma is ≤ 20 Pa for the felsic xenoliths, and ≤ 60 Pa for denser, mafic xenoliths. These values are low compared to experimental measurements and theoretical expectations, but indicate that magma yield strength was insignificant in the transport of the xenoliths.

At Cottonwood Creek, the xenoliths are dominantly clinopyroxenites with variable biotite and apatite content, with a few peridotites. Isotopic analysis of megacrysts shows that these xenoliths are approximately contemporaneous with the host magma. Mineral chemistry shows that, though minerals in the clinopyroxenites are clearly derived from crystallization of mafic alkaline magmas, they are not strictly cognate with the host MNS. The peridotite xenoliths contain two generations of phlogopite, one of which, with low TiO_2 and BaO, is foreign to the mafic alkaline magmas. The P-T conditions of entrainment of the peridotite xenoliths are constrained to 10–16 kbar and 1,100–1,150°C, based on measurements of CaO content in olivine.

ACKNOWLEDGMENTS

Funding for part of this study was provided by a summer faculty research grant from Old Dominion University (ODURF 931009). Initial work was funded by NSF grant EAR-8307617 to D.H. Eggler at Pennsylvania State University. R. Lustwerk, R. Jensen, B. Weiner, and Y. Touysinhthiphonexay assisted with field work. Additional funding was provided by Tark Geosciences, Billerica, MA. Review and suggested modifications by Sandra Underwood helped materially to improve this paper.

REFERENCES

Adams, G.E., and Bishop, C.E., 1986, The olivine-clinopyroxene geobarometer: experimental results in the CaO-FeO-MgO-SiO_2 system. Contributions to Mineralogy and Petrology, 94:230-237.

Baker, D.W., and Berg, R.B., 1991, Guidebook of the Central Montana Alkalic Province: Geology, Ore Deposits and Origin. Tobacco Root Geological Society, 16th Annual Field Conference. Montana Bureau of Mines and Geology, Special Publication 100.

Bottinga, Y., Weill, D., and Richet, P., 1982, Density calculations for silicate liquids. I. Revised method for aluminosilicate compositions. Geochimica et Cosmochimica Acta, 46:909-919.

Chakhmouradian, A.R., and Mitchell, R.H., 2002, The mineralogy of Ba- and Zr-rich alkaline pegmatites from Gordon Butte, Crazy Mountains (Montana, USA): comparisons between potassic and sodic agpaitic pegmatites. Contributions to Mineralogy and Petrology, 143:93-114.

Corsaro, R.A., and Pompilio, M., 2004, Buoyancy-controlled eruption of magmas at Mt. Etna. Terra Nova, 16:16-22. doi: 10.1046/j.1365-3121.2003.00520.x

du Bray, E.A., and Harlan, S.S., 1996, The Eocene Big Timber stock, south-central Montana: Development of extensive compositional variation in an arc-related intrusion by side-wall crystallization and cumulate glomerocryst remixing. Geological Society of America Bulletin, 108:1404-1424.

Dudás, F.Ö., 1990, Petrogenesis and mantle source of igneous rocks in the Crazy Mountains, Montana. PhD thesis, Pennsylvania State University, State College, PA, 456 pp.

Feltis, R.D., 1985, White Sulphur Springs 1° x 509 2° quadrangle, west-central Montana. Structure contour (configuration) map of the top of the Madison Group. Montana Bureau of Mines and Geology, Geologic Map 39.

Finnerty, A.A., and Boyd, F.R., 1978, Pressure-dependent solubility of calcium in forsterite coexisting with diopside and enstatite. Carnegie Institution of Washington, Annual Report, 77:713-717.

Ghiorso, M.S., and Sack, R.O., 1995, Chemical mass transfer in magmatic processes IV. A revised and internally consistent thermodynamic model for the interpolation and extrapolation of liquid-solid equilibria in magmatic systems at elevated temperatures and pressures. Contributions to Mineralogy and Petrology, 119:197-212.

Giordano, D., Mangiacapra, A., Potuzak, M., Russell, J.K., Romano, C., Dingwell, D.B., and Di Muro, A., 2006, An expanded non-Arrhenian model for silicate melt viscosity: A treatment for metaluminous, peraluminous and peralkaline liquids. Chemical Geology, 229:42-56.

Gonnermann, H.M., and Manga, M., 2007, The fluid mechanics inside a volcano. Annual Review of Fluid Mechanics, 39:321-356.

Harlan, S.S., 2006, $^{40}Ar/^{39}Ar$ dates from alkaline intrusions in the northern Crazy Mountains, Montana: Implications for the timing and duration of alkaline magmatism in the central Montana alkalic province. Rocky Mountain Geology, 41:45-55.

Harlan, S.S., Geissman, J.W., Lageson, D.R., and Snee, L.W., 1988, Paleomagnetic and isotopic dating of thrust-belt deformation along the eastern edge of the Helena salient, northern Crazy Mountains Basin, Montana. Geological Society of America Bulletin, 100:492-499.

Harris, A.J.L., and Allen, J.S., 2008, One-, two-, and three-phase viscosity treatments for basaltic lava flows. Journal of Geophysical Research, 113, B09212.

Lange, R.L., and Carmichael, I.S.E., 1990, Thermodynamic properties of silicate liquids with emphasis on density, thermal expansion and compressibility. Reviews in Mineralogy, 24:25-64.

Longo, A., Barsanti, M., Papale, P., Vassalli, M., Montagna, C.P., Bisconti, L., and Saccorotti, G., 2009, A numerical code for the simulation of magma-

rocks dynamics. Communications to SIMAI Congress, 3:237 (12 pp). doi: 10.1685/CSC09237.

McBirney, A.R., 1979, Effects of assimilation. Chapter 10 in H.S. Yoder, Jr., ed., The Evolution of the Igneous Rocks, p. 307-338, Princeton University Press, Princeton, N.J.

McCamy, K., and Meyer, R.P., 1964, A correlation method of apparent velocity measurement. Journal of Geophysical Research, 69:691-699.

McMannis, W.J., 1965, Resume of depositional and structural history of western Montana. American Association of Petroleum Geologists Bulletin, 49:1801-1823.

Møller, P.C.F., Mewis, J., and Bonn, D., 2006, Yield stress and thixotropy: on the difficulty of measuring yield stresses in practice. Soft Matter, 2:274-283.

Petford, N., 2003, Rheology of granitic magmas during ascent and emplacement. Annual Review of Earth and Planetary Sciences, 31:399-427.

Righter, K., and Carmichael, I.S.E., 1993, Mega-xenocrysts in alkali olivine basalts: fragments of disrupted mineral assemblages. American Mineralogist, 78:1230-1245.

Robinson, J.D., 1965, The Cottonwood Creek Plugs, Crazy Mountains, Montana. B.S. Thesis, U. of Cincinnati, Cincinnati, OH. Unpublished.

Ross, C.P., Andrews, D.A., and Witkind, I.J., 1955, Geological map of Montana. U.S. Geological Survey.

Rust, A.C., Manga, M., and Cashman, K.V., 2003, Determining flow type, shear rate and shear stress in magmas from bubble shapes and orientations. Journal of Volcanology and Geothermal Research, 122:111-132.

Sachs, P.M., and Stange, S., 1993, Fast assimilation of xenoliths in magmas. Journal of Geophysical Research, 98:19741-19754.

Sahagian, D., 2005, Volcanic eruption mechanisms: Insights from intercomparison of models of conduit processes. Journal of Volcanology and Geothermal Research, 143:1-15.

Shaw, H.R., 1972, Viscosities of magmatic silicate liquids: An empirical method of prediction. American Journal of Science, 272:870-893.

Sparks, R.S.J., Pinkerton, H., and MacDonald, R., 1977, The transport of xenoliths in magmas. Earth and Planetary Science Letters, 35:234-238.

Spera, F.J., 1984, Carbon dioxide in petrogenesis III: Role of volatiles in the ascent of alkaline magma with special reference to xenolith-bearing mafic lavas. Contributions to Mineralogy and Petrology, 88:217-232.

Stein, D.J., and Spera, F.J., 1992, Rheology and microstructure of magmatic emulsions: theory and experiments. Journal of Volcanology and Geothermal Research, 49:157-174.

Walsh, S.D.C., and Saar, M.O., 2008, Numerical models of stiffness and yield stress growth in crystal-melt suspensions. Earth and Planetary Science Letters, 267:32-44.

Woodward, L.A., 1981, Tectonic framework of the disturbed belt of west-central Montana. American Association of Petroleum Geologists Bulletin, 65:291-302.

Woodward, L.A., 1982, Tectonic map of the fold and thrust belt and adjacent areas, west-central Montana. Montana Bureau of Mines and Geology, Geological Map 30.

Yoshinobu, A.S., Wolak, J.M., Paterson, S.R., Pignotta, G.S., and Anderson, H.S., 2009, Determining relative magma and host rock xenolith rheology during magmatic fabric formation in plutons: Examples from the middle and upper crust. Geosphere, 5:270-285.

FIELD TRIP GUIDES

GEOLOGY OF BIG SKY, MONTANA: ROAD LOG

James Rose and Kirk Waren

Montana Bureau of Mines and Geology

INTRODUCTION

Big Sky Resort is located in an area of spectacular geology on the east side of the Madison Range. This field trip will explore the geology extending from the unique ski peaks, south across the scenic valley, and north into the rugged wilderness. Highlights include one of southwest Montana's most prominent faults, Cretaceous stratigraphy, "Christmas tree" laccoliths, unusual tectonic structures, rock glaciers, glacial deposits, groundwater, and geologic hazards. Field trip stops are shown in figure 1. Figure 2 shows the regional geology.

GEOLOGIC OVERVIEW

Lone Mountain is the focus of Big Sky Resort, because of the ideal ski slopes it provides. Lone Mountain and similar peaks in the area—Fan Mountain, Cedar Mountain, and Pioneer Mountain—owe their conical shapes to dacite porphyry laccoliths (fig. 2). Swanson (1950) interpreted them as "Christmas Tree" laccoliths intruded as a central pipe (trunk) from which sills (branches) emanated along bedding planes in the sedimentary host rock. Gravity data suggest that Lone Mountain is the main intrusive center, and the other laccoliths are satellites (Tysdal and others, 1986).

The Spanish Peaks Fault, one of southwest Montana's most impressive Laramide faults, crosses the area north of Big Sky. The reverse fault's offset of at least 10,000 ft (3,050 m) to 13,500 ft (4,115 m) (Garihan and others, 1983; McMannis and Chadwick, 1964) placed Archean metamorphic crystalline rock over rock as young as the Cretaceous Frontier Formation. Archean meta-sedimentary, meta-igneous, and plutonic rock in the hanging wall of the fault produced the rugged terrain of the Spanish Peaks and adjacent country, in contrast to the less resistant rock in the footwall. Footwall Paleozoic and Mesozoic rock was tilted to the southwest and locally overturned.

Folds in the Big Sky Mountain Village area that have not been substantially eroded appear offset or truncated by an interpreted fault that parallels the Spanish Peaks Fault (Vuke, 2013a). The fault postdates the intrusion of the laccoliths.

The Big Sky area has features conducive to landslide development: steep mountain slopes, planes of weakness that dip downslope, alternating competent and incompetent rock, and moisture from heavy annual snowfall. The Mowry and Frontier Formations contain bentonite beds and bentonitic shale that facilitate landslide movement. Numerous landslides have been mapped within the resort boundaries (Vuke, 2013b). Geotechnical studies have confirmed that many landslides in the area are still active. Area seismicity and human activity compound the possibility of landslides (Vuke, 2013b). Building of homes and other structures on the flat upper surfaces of landslides, the construction of road cuts and water retention ponds, the application of irrigation, and the installation of drain fields may increase landslide potential in some areas.

ROAD LOG

The field trip stops are shown in figure 1. All GPS coordinates are in WGS84 Datum. Mileage is referenced from STOP 1.

CAUTION: Highway 191 from Bozeman to Big Sky and State Road 64 (Lone Mountain Trail) through Big Sky are both very busy routes with heavy car and truck traffic and no shoulders. Stay alert and stay off the roads when at the stops.

From the MSU campus at Bozeman to the first stop at the Big Sky Visitors Center is about 42 mi. As you approach Big Sky, look for mile marker 49 (on the left shoulder) at about 41 mi. At 0.2 mi past mile marker 49, Highway 191 crosses Dudley Creek. Dudley Creek flows into the Gallatin River from the west, along the trace of the Spanish Peaks Fault. Prior to crossing Dudley Creek, Gallatin Canyon and Highway 191 cut through Archean gneiss, schist, and meta-igneous basement rock in the hanging wall of the Spanish Peaks Fault. After crossing the fault at Dudley Creek, exposures of Paleozoic and Mesozoic sediments in the footwall of the fault form the canyon walls.

At mile marker 48, Highway 191 crosses a bridge

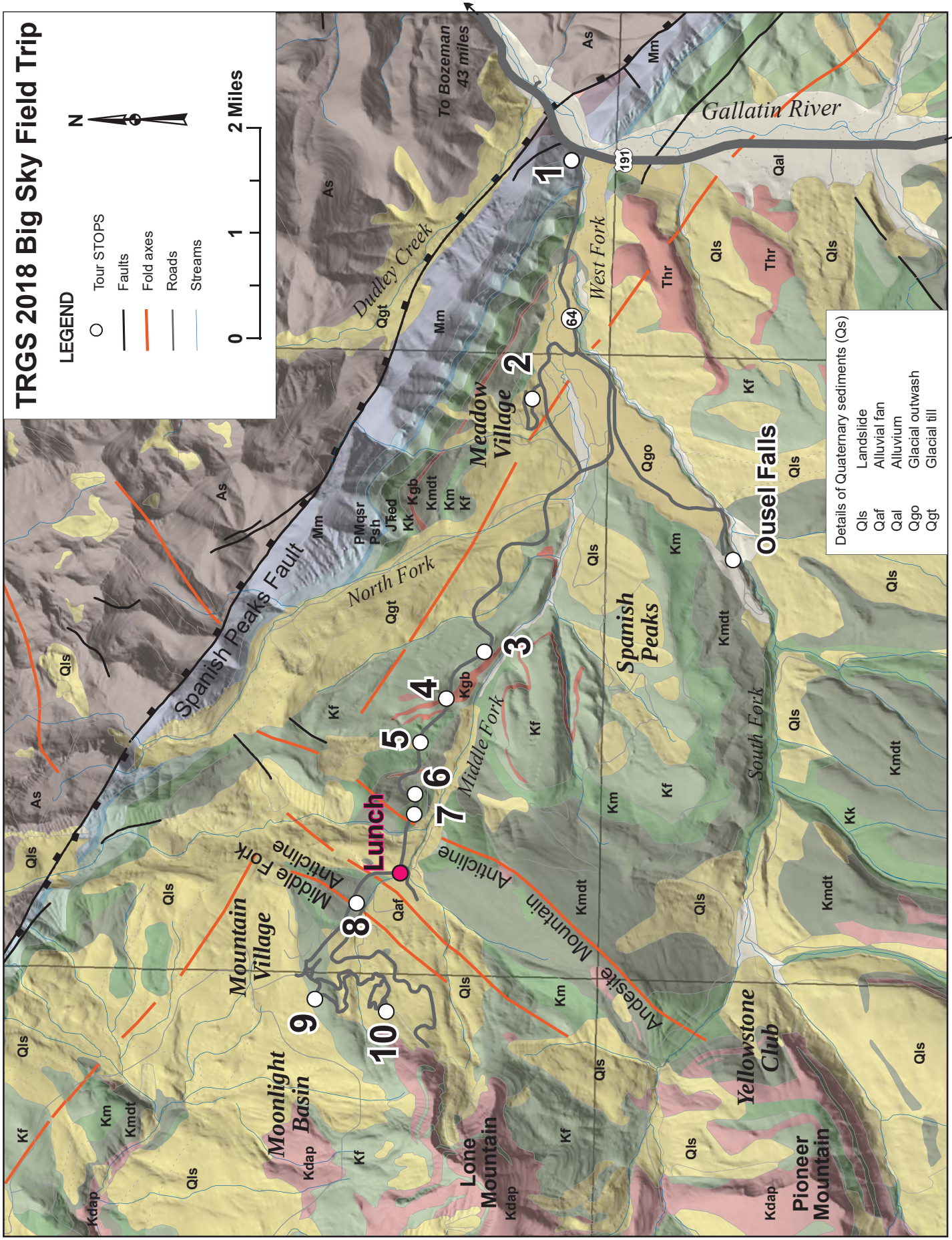

Figure 1. Detailed geologic map showing field trips stops. Geology from Vuke, 2013a.

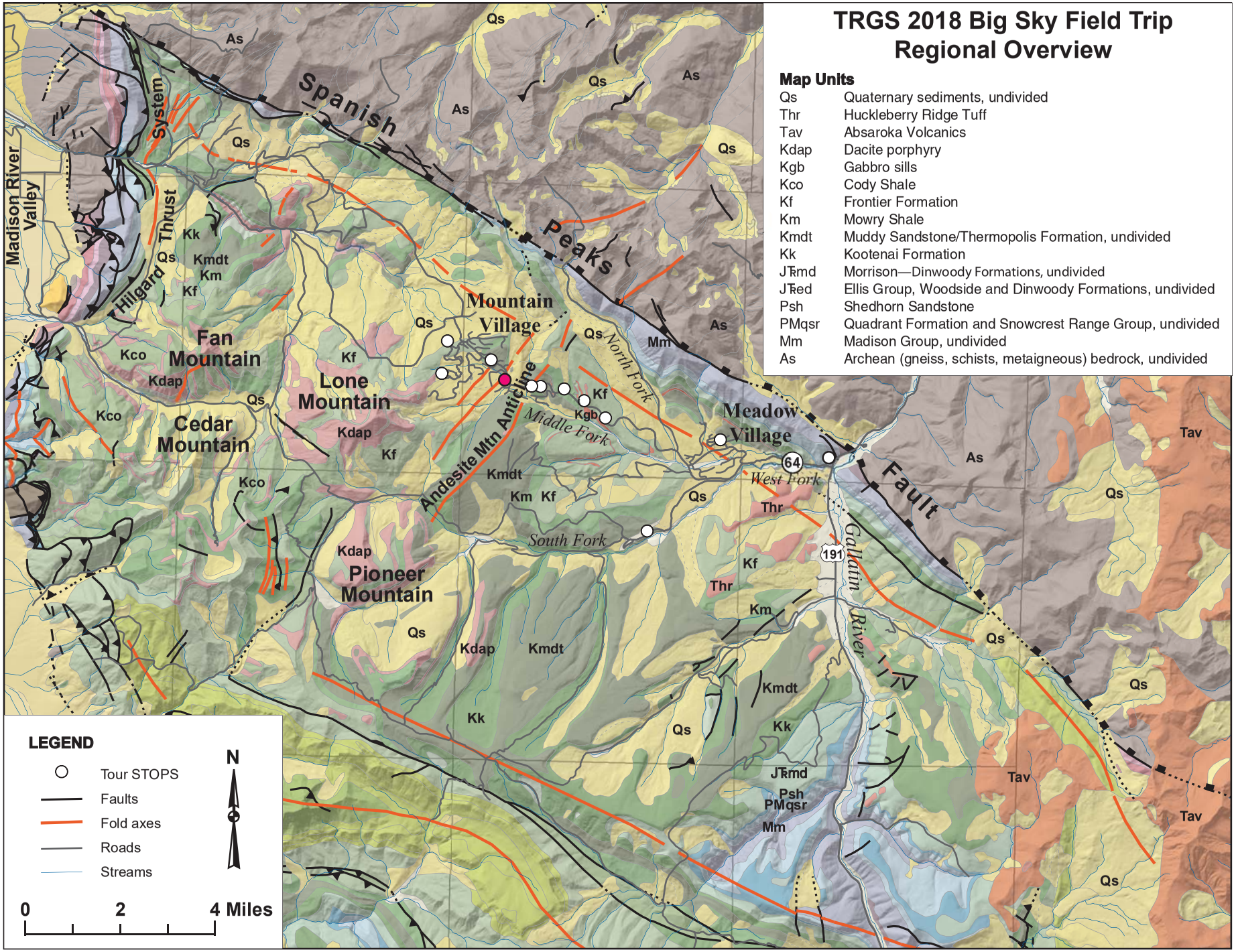

Figure 2. Regional geologic map of the Big Sky area (modified from Kellogg and Williams, 2000).

over the West Fork of the Gallatin River. Immediately past the bridge turn right at the stop light onto Lone Peak Trail (State Road 64). STOP 1 is the Big Sky Visitors Center, at the second turnoff to the right, about 125 yards past the Highway 191 turnoff.

STOP 1 Mile 0

(45.265299 N, -111.254726 W)

Geology

Big Sky Resort is located on an isolated segment of Cretaceous bedrock between the Madison Range to the south and the Spanish Peaks Range to the north (fig. 2). The Paleozoic and Mesozoic formations exposed at Big Sky are steeply folded by faulting along the Spanish Peaks Fault, located just north of the resort. The Spanish Peaks Fault is a regional reverse fault that extends from the northwest corner of Yellowstone Park located east of Big Sky, for about 30 mi northwest to the Madison River Valley. The Spanish Peaks Fault crosses the Gallatin River Canyon north of STOP 1, at the Dudley Creek drainage, but is mostly obscured by glacial till. The Spanish Peaks Fault thrusts Archean crystalline metamorphic rock in the hanging wall, southwest over Paleozoic and Mesozoic rock in the Big Sky area. The less resistant footwall rock is tilted to the south and southwest, and is locally overturned. Sedimentary rocks visible in outcrop south of the fault at Highway 191 to Meadow Village at Big Sky include, from the fault south, Devonian Jefferson Formation, Mississippian–Devonian Three Forks Formation, and Mississippian Madison Group, which is visible at STOP 1. From STOP 1 to Meadow Village exposures along State Road 64 include Pennsylvanian Quadrant Formation, Pennsylvanian–Upper Mississippian Snowcrest Range Group, Lower Permian Shedhorn Sandstone, Triassic Dinwoody Formation, Jurassic Ellis Group (Swift, Rierdon, and Sawtooth Formations), and the Jurassic Morrison Formation. Overlying the Morrison Formation are Cretaceous rocks that we will be examining during this trip, including the Kootenai, Lower Thermopolis, Upper Thermopolis, Muddy, Mowry, and Frontier Formations, along with Cretaceous gabbro sills related to the dacite Christmas tree laccolithic within Lone Mountain.

Groundwater and Surface water

In the Gallatin River Canyon, the steeply dipping outcrops of Mississippian Madison Limestone resulted from tight folding associated with the Spanish Peaks Fault. This nearly perpendicular bedrock ridge creates a narrow pinch point for the Gallatin River Valley. A number of springs drain into the Gallatin River from the upturned Madison Group limestone where the formation is exposed at the sides and bottom of the river canyon. Three significant springs are the Slow Vehicle Spring, located beneath Highway 191 on the west side of the canyon, about 0.5 mi south of mile marker 49, and two springs directly across the river at the east side of the canyon.

Stream gauging and water-temperature measurements from the Gallatin River (Schaffer, 2011), above and below where the Madison Group outcrops, show that the large springs, along with subsurface seeps beneath the river, contribute about 65 to 70 cfs year-round to the Gallatin River flow (table 1). This flow represents about 30% of the downstream Gallatin River discharge during low flow conditions.

From STOP 1 turn right on to State Road 64 and continue west 1.9 mi to Little Coyote Road at Meadow Village. Mile marker 2.0 is just beyond the turn. As you leave STOP 1, watch for bighorn sheep on the road and on the ridge to the north. The ridge is a continuation of the Paleozoic and Mesozoic rock deformed by the Spanish Peaks Fault. The units become younger towards Meadow Village.

At Little Coyote Road, turn right and follow the road around, crossing the West Fork of the Gallatin River. At 2.6 mi turn right on Two Gun White Calf Road, continue 0.6 mi around the first hairpin right turn. STOP 2, at 3.2 mi, is at the pullout on your right.

Table 1. Gallatin River flow.

	Gallatin River discharge above springs (cfs)	Gallatin River discharge below springs (cfs)	Difference/change/gain = ground water discharge (cfs)	Percent groundwater contribution to Gallatin River discharge
Early Spring	150.13	216.21	+ 66.08	31%
Fall	162.83	230.72	+ 67.89	29%

STOP 2 Mile 3.2
(45.272165 N, -111.302136 W)
Meadow Village Aquifer Discussion

STOP 2 is located on Pleistocene glacial outwash from the North Fork drainage located to the northwest. Glacial deposits in the valley are Pinedale glaciation (about 20–14 Ka) but may contain some till from Bull Lake glaciation (about 140–100 Ka). The outwash contains clasts of dacite porphyry, Lower Thermopolis quartz–arenite, other Cretaceous sandstones, and some Archean metamorphic clasts.

Beneath the Arnold Palmer-designed Meadow Village Golf Course directly below is the sand and gravel Meadow Village aquifer. The aquifer is the primary water source for the Meadow Village and Town Center to the south, and supplements the water supplies for the Mountain Village and Yellowstone Club. It also contains the best-quality drinking water in the area.

The sand and gravel Meadow Village Aquifer is a combination of glacial outwash and river alluvium. Well lithology logs indicate layers of cobbles and boulders, gravel, clay with gravel and very silty sand, and gravel intervals irregularly distributed in sediments beneath the golf course. The West Fork of the Gallatin River flows across the surface of the aquifer. The base of the aquifer is the tight black shales of the Frontier Formation that lies between 10 to 70 ft below the golf course. The deepest part of the aquifer is in a shale trough 30–70 ft deep that runs west-to-east beneath, and parallel to the West Fork of the Gallatin River. The Big Sky Public Water Supply System production wells are all located within this deep trough.

Return to Little Coyote Road (mile 3.8) and turn right; continue 0.9 mi to T-intersection with State Road 64, at mile 4.7. Turn right on State Road 64 toward Big Sky Resort. Most of the rest of field trip will be along this road.

Mile 7.0. Pull out on left.

STOP 3 Mile 7.0
(45.277911 N, -111.351293 W)
Upper Cretaceous Frontier Formation

The road cut exposes layers of near shore interbedded marine and non-marine sediments associated with sea level fluctuations within the Frontier Formation. The Frontier Formation is exposed at the land surface throughout much of the resort area. The formation is primarily black to gray shales with interbedded thin to thick, yellowish tan, cross-bedded sandstones. The shale to sandstone ratio is about 3:1. Some shales are coaly. The Frontier also contains several porcellanite and bentonite beds.

A landslide in the Frontier Formation is visible to the south.

Mile 7.6 Pull out on left.

STOP 4 Mile 7.6
(45.282958 N, -111.360511 W)
Cretaceous Gabbro Sill

STOP 4 is still within the Frontier Formation. At this stop we will examine sills of Cretaceous gabbro associated with the Lone Mountain laccolith.

Mile 8.1 Pull out on left at State Road 64 mile marker 7.0.

STOP 5 Mile 8.1
(45.286313 N, -111.369155 W)
Outcrops of Upper and Lower Cretaceous Mowry Shale

The Lower Vaughn Member of the Mowry Shale is a bentonitic mudstone with minor thin quartz sandstone beds and porcellanite beds. The bentonitic mudstone may be light gray, green, yellow, brown, light red, or cream colored, and likely represent accumulations of volcanic ash in a marine environment.

As you drive to STOPS 6 and 7 you will pass through poorly exposed Lower Cretaceous Muddy Sandstone. It is composed predominantly of clayey brown to brownish gray sandstones separated by shales. At mile 8.5 are sandstones and shales of the Upper Thermopolis Formation.

DRIVE TO PARKING AREA FOR STOP 7 (Mile 8.8) and walk back to STOP 6, staying off the road.

STOP 6 Mile 8.7
(45.286910 N, -111.379174 W)
Lower Cretaceous, lower Thermopolis Formation Marine Sandstone

The white to tan sandstone beds consist of clean quartz arenite with symmetrical ripple marks, visible in some of the rock faces along the road cut, rust-colored clots (hence the previous name “Rusty beds”), and black, fissile shale interbeds (these shales are very evident along the Ousel Falls Trail). The upper part of the Thermopolis Formation is black shale, which is poorly exposed in this area. Around the corner towards

STOP 7, the rust staining becomes more prevalent as we approach the Kootenai Formation contact.

Mile 8.8, just before State Road 64 mile marker 8.0.

STOP 7 Mile 8.8

(45.286965 N, -111.383045 W)

Lower Cretaceous Kootenai Formation

The non-marine Kootenai Formation marks the transition from a non-marine to a marine environment. An oolitic limestone with abundant gastropod fossils defines the top of the Kootenai and is visible as red-stained, thicker, more massive layers. The presence of gastropods and the oolitic texture of the limestone suggests a shallow sea depositional environment. The limestone unit is visible about 150 yards west of the corner at STOP 6, towards STOP 7.

Below the limestone are layers of red, purple, yellow, and gray shale, mudstone, siltstone, sandstone, and locally limestone. The shales are mostly gray at this road cut. The lower Kootenai is primarily a gray, salt-and-pepper sandstone (visible here) and often contains a chert-pebble conglomerate (also present in the road cut). This unit is the most popular drilling target for water wells in the Big Sky area. Fractures in the Kootenai provide some of the best water production and better water quality in the area.

Looking south across the Middle Fork of the West Fork of the Gallatin River, on the opposite hill slope, is a cross-section view through the Andesite Mountain anticline, perpendicular to the fold axis. Contacts on Andesite Mountain are much higher in elevation than seen on this side of the road at STOP 8, suggesting fault offset.

Continue west past Big Sky Resort Road, the entrance to Big Sky Resort Mountain Village on left (mile 9.6).

Drive past the fire station on your right (mile 9.9).

Two sandstone units form ridges in the land surface about 200 and 300 yards west of the fire station. The low, narrow ridges of near-vertical sandstone outcrops trend perpendicular to the road on the slopes to the north (right side) of the road. These are sandstones of the Cretaceous Muddy Formation on the east limb of the tightly folded Middle Fork anticline (STOP 8).

Look for the parking area for STOP 8 to your left, just past White Otter Road.

STOP 8 Mile 10.2

(45.294529 N, -111.400525 W)

Middle Fork Anticline

Looking across the road to the north, you are standing on the axis of the Middle Fork anticline (bearing N. 26° E.). The anticline consists of tightly folded beds of lower Thermopolis sandstones in the core, surrounded by upper Thermopolis, Muddy, Mowry, and Frontier Formations. The ground surface to the south, toward Big Sky Resort, is covered in Quaternary alluvial fan sediments that prevent tracing this anticline to the south. In addition, there is a steep east–west-trending drop-off in the hill slope, almost a vertical cliff, along the Middle Fork of the West Fork of the Gallatin River at White Otter Road, which may indicate a crossing fault. It is uncertain what relationship this fold has to others in the area. The west flank of the Andesite Mountain Anticline we viewed at STOP 7 is visible to the south and east, behind the resort hotels. The resistant rock capping the anticline is the lower Thermopolis sandstone. Some of the intrusive dacite sills are visible on Lone Mountain from this location. The sills appear as dark flat-lying bands across the mountain. The parking area contains numerous rock fragments from the T formations exposed in the anticline, as well as rounded cobbles of gneiss and schist from Archean basement rocks deposited on the land surface in till.

Mountain Village gets most of its drinking water supply from seven water wells in the Mountain Village basin. The best producing wells are completed in highly fractured dacite sills that produce high volumes of ground water. The non-reactive nature of the intrusive rock results in groundwater with a very low dissolved mineral content.

Continue west on State Road 64 on Lone Mountain Trail to end at mile 11.1. The road turns left and becomes Mountain Loop Road. Drive through Moonlight Basin entrance gate at mile 11.2. Continue south on Mountain Loop Road, through the roundabout, and crossing under a ski bridge. Continue through the tight left-hand hairpin turn and pull onto shoulder at mile 11.5, just past the Peaks View Road junction.

STOP 9 Mile 11.5

(45.299920 N, -111.419342 W)

From this stop, look north across Moonlight Basin to the Ridgeline at the north end of Big Sky Resort.

Although over 2.5 mi distant, the contact between the Archean metamorphic rocks at the top of the ridge and the upturned Mesozoic strata against the trace of the Spanish Peaks Fault is visible. In this area and to the northwest, the fault is located on the south side of the ridge and the fault trace gradually descends in elevation to the northwest. Just below the fault trace, you might be able to see a large landslide scarp that exposes red beds of the upper Kootenai Formation. The red color provided the opportunity to trace the distance the landslide moved downslope, which was 1 mi.

Return back down Mountain Loop Road towards the Moonlight Basin Entrance. Turn right on to the lower portion of Mountain Loop Road (mile 11.7), before the roundabout. Follow Mountain Loop road past the T-junction at mile 12.2, continue straight on Diamond Hitch Road to Hackamore Road, mile 12.9. Turn left onto Hackamore Road and continue to the end of the cul-de-sac at mile 13.0. Park on shoulder of road at the end of the street. A rock glacier is visible directly behind the last house at the end of the road.

STOP 10 is located in a subdivision and the land is all private property. Please respect the landowners and do not trespass.

STOP 10 Mile 13.0

(45.290123 N, -111.421423 W)

Rock Glacier

The top of the rock glacier is flat or even slightly depressed in places, suggesting there is no longer an ice core, and the glacier is inactive. This is one of several rock glaciers, some active, some inactive, on the flanks of Lone Mountain.

This is the final field trip stop. Return to Diamond Hitch Road (mile 13.1), continue straight through the T-junction (mile 14.1), and on to Mountain Loop Road, driving west to the next T-junction (mile 14.6) at Mountain Loop Road. Turn right and right again at the roundabout, taking the cutoff road back to Lone Mountain Trail (mile 14.7). Turn right on Lone Mountain Trail (State Road 64) and continue to Lake Levinsky at Big Sky Mountain Village Resort.

Lunch

Stop at the pullout at Lake Levinsky, just before Big Sky Resort Road and the entrance to Big Sky Mountain Village Resort (45.288671 N, -111.394512 W).

OPTIONAL AFTERNOON FIELD TRIPS

Big Sky Tram Base: Construction on an Active Rock Glacier

After lunch, the group will meet with a member of Big Sky Mountain Operations. We will make our way up to the base of the Big Sky Tram for a discussion about construction of the tram base which sits on an active, ice-cored rock glacier.

Ousel Falls Self-Guided Hike

The easy hike to the waterfalls is about 1.6 mi round trip from the trailhead parking lot. The trail is a well-maintained gravel path with some gentle up and down hill sections.

To get to Ousel Falls from the Big Sky Resort Mountain Village entrance, turn right onto State Road 64 and return down the mountain to the stoplight at Town Center, across from the Meadow Village Golf Course. Turn right onto Ousel Falls Road. Continue southwest 1.8 mi to the Ousel Falls Trailhead parking lot on the left (45.244158 N, -111.332401 W).

Ousel Falls trail is constructed through the Lower Cretaceous Thermopolis Formation (much better exposure than at STOP 6 of the Road Log).

The trail starts in fissile shales with very thin sandstone beds of the Lower Thermopolis Shale. The shales are heavily weathered and crumbly at the surface, and the sandstones are dirty brown. Below the bridge at the trail crossing of the South Fork of the West Fork of the Gallatin River, ripple marks in red-tan clean quartz sandstone ledges mark the lower Thermopolis Formation. After crossing the bridge, the trail climbs toward the falls and stays in the lower Thermopolis Formation. Waterfalls of the South Fork of the West Fork of the Gallatin River spill off sandstone ledges. The trail ends at the upper waterfall.

Bedding at Ousel Falls is dipping about 9 degrees northeast, towards the large synclinal fold axis beneath Meadow Village. The north limb of this fold forms the steeply dipping Paleozoic and Mesozoic rock in the footwall of the Spanish Peaks Fault. The Kootenai Formation is exposed upstream about 1/2 mi from the end of the trail.

REFERENCES

Balster, Clifford A., Editor, 1970, Catalog of Stratigraphic Names for Montana, Montana Geological Society and Montana Bureau of Mines and Geology, 448 pgs.

Garihan, J.M., Schmidt, C.J., Young, S.W., and Williams, M.A., 1983, Geology and recurrent movement history of the Bismark-Spanish Peaks-Gardiner fault system, southwest Montana, *in* Lowell, J.D., ed., Rocky Mountain Foreland Basins and Uplifts, p. 295–314.

Hall, William B., 1961, Geology of part of the Upper Gallatin Valley of Southwest Montana: Laramie, University of Wyoming Ph.D. dissertation, 239 pgs.

James, H.L., and Hedge, C.E., 1980, Age of Basement Rocks of southwest Montana, Geological Society of America Bulletin, Part I, v. 91, pg. 11–15.

Kellogg, K.S., and Williams, V.S., 2000, Geologic map of the Ennis 30'x 60' quadrangle, Madison and Gallatin Counties, Montana, and Park County, Wyoming: U.S. Geological Survey Geologic Investigation Series I-2690, scale 1:100,000.

McMannis, W.J., and Chadwick, R.A., 1964, Geology of the Garnet Mountain quadrangle, Gallatin County, Montana: Montana Bureau of Mines and Geology Bulletin 43, 47 p.

Schaffer, Mark, 2011, Field Validation of the Hydrologic Model used to delineate the Yellowstone National Park Controlled Ground Water Area near Big Sky Montana: Senior Thesis, Montana State University, Department of Earth Science, 20 pgs.

Swanson, R.W., 1950, Geology of part of the Virginia City and Eldridge quadrangles, Montana: U.S. Geological survey Open-File Report 51-4, 12 p.

Smith, Larry N., 2008, Road Tour Log, Hydrogeology of the Big Sky area, MT. Montana AWRA Conference Tour, October 2, 2008, 3 pgs.

Tysdal, R.G., Marvin, R.F., and DeWitt, E.H., 1986, Late Cretaceous stratigraphy, deformation, and intrusion in the Madison Range of southwestern Montana: Geological Society of America Bulletin, v. 97, p. 859-868.

Tysdal, R.G., Dyman, T.S., Nichols, D.J., and Cobban, W.A., 1990, Correlation chart of Frontier Formation from Greenhorn Range, southwestern Montana, to Mount Everts in Yellowstone National Park, Wyoming, Miscellaneous Field Studies Map MF-2116 pamphlet, 16 pgs.

Tysdal, R.G., 1991, Depositional Environments for Strata of Composite Section of Frontier Formation, Madison Range, Southwestern, Montana, United States Geological Survey Bulletin 1949, 23 pgs.

Vuke, S.M., 2013a, Geologic map of the Fan Mountain, Lone Mountain, and Gallatin Peak 7.5' quadrangles, Madison Range, Madison and Gallatin Counties, Montana: Montana Bureau of Mines and Geology Open File Report 633, Map, 1:24,000.

Vuke, S.M., 2013b, Landslide map of the Big Sky area, Madison and Gallatin Counties, Montana: Montana Bureau of Mines and Geology Open-File Report 632, scale 1:24,000.

GEOLOGY AND THERMAL FEATURES OF THE GARDINER BASIN, PARK COUNTY, MONTANA

Alan R. English

Montana Bureau of Mines and Geology

INTRODUCTION

The Middle Yellowstone River corridor between Gardiner and Livingston, Montana, includes the Paradise Valley, Yankee Jim Canyon, and the Gardiner Basin. The river corridor was travelled by the Hayden Expedition in 1871, and has long been a popular route for geology field trips, including past TRGS and GSA trips. While many past geology field trips have focused on the Paradise Valley, this field trip will focus on the geology of the northwest-trending Gardiner Basin, between Mammoth Hots Springs, Wyoming, and the south end of Yankee Jim Canyon (fig. 1). We will view and discuss the major structural features of the basin, the Quaternary surficial geology of the basin, and the geothermal features in the basin. If scheduling allows, we will also meet Dr. Jeffery Hungerford, staff Geologist for Yellowstone National Park. A detailed trip log will be provided to participants, which will include geologic maps, summaries of the geology at each stop, and references.

OVERVIEW OF FIELD TRIP STOPS

STOP 1

LaDuke Hot Springs and Devils Slide

Here we will first discuss the major structural features of the Gardiner Basin, including the Gardiner Reverse Fault and Tertiary Extensional faults. We will view and discuss the famous Devils Slide on Cinnabar Mountain, and the structure of the southwest end of the basin. We will also inspect and discuss LaDuke Hot Spring (LaDuke) and other nearby geothermal discharge points nearby. The water chemistry of LaDuke will be summarized and we will discuss possible flow paths for the geothermal water that discharges at LaDuke. We will finish with a short hike to view a strange deposit just above LaDuke, and briefly look at outcrops of Archean Basement rocks exposed in the hanging wall of the Gardiner Reverse Fault. A restroom is available at this stop.

STOP 2

Gardiner Airport

At this stop we will take a short hike to look at near-vertical exposures of Mesozoic sedimentary rocks exposed in the footwall of the Gardiner Reverse Fault. The stratigraphy of the Mesozoic formations in the area will be reviewed and we will discuss which formation(s) is exposed at the stop. We will also view and discuss basalt flows and travertine deposits that overlie the Mesozoic formations, and view slumps and landslide features near the stop.

STOP 3

Gardiner Travertine Bench

This stop will be focused on viewing the Gardiner Travertine deposits and discussing the origin and age of the deposits. We will look at some of the depositional facies seen in the travertine deposits and discuss possible relationships between these travertine deposits, Mammoth Hot Springs, and the travertine deposits that form Terrace Mountain, southwest of Mammoth Hot Springs. If scheduling allows, we will also meet with the Park Geologist at this stop.

STOP 4

Bear Creek Overlook

At this stop we will take a short hike from the Jardine Road to view the lower reach of Bear Creek where it joins the Yellowstone River. Here the projected trace of the Gardiner Reverse fault changes from southeast to a more southerly direction, and consists of an imbricate fault zone that cuts Paleozoic and Mesozoic formations. At the mouth of Bear Creek the Archean basement is exposed, and a large travertine mound has been deposited by hot springs at the mouth of Bear Creek.

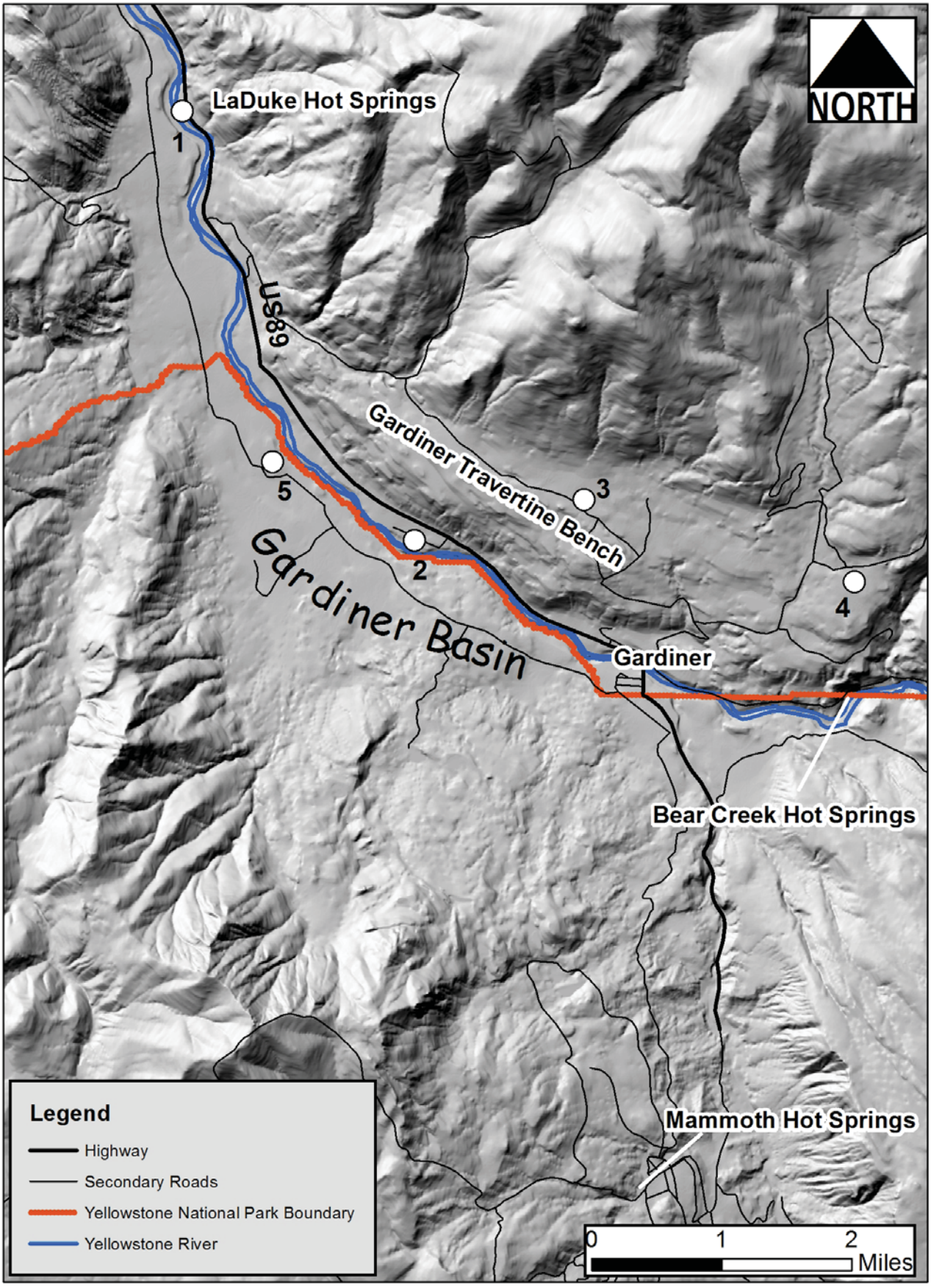

Figure 1. Locations and order of planned fieldtrip stops in the Gardiner Basin. Each stop will involve a short hike to view local geologic features.

STOP 5

Stephens Creek Area

The last stop will be along the gravel road leading northwest out of Gardiner, along the southwest side of the Yellowstone River. We will view some features that are considered to be mega ripples formed during glacial outburst floods that occurred as the Yellowstone Outlet glacier retreated from the area. We will also discuss other surficial deposits visible in the area, and discuss efforts by the National Park Service to develop a ground-water supply to support the Stephens Creek Corrals, which are used by the Park Service to quarantine bison that migrate out of the Park.

ROAD LOG TO THE STRUCTURAL GEOLOGY OF THE LEWIS AND CLARK STATE PARK AND SURROUNDING AREA, SOUTHWESTERN MONTANA: SOME NEW IDEAS AND MORE QUESTIONS

Christopher Schmidt,[1] S. Christopher Whisner,[2] and Jennifer B. Whisner[2]

[1]Department of Geosciences, Western Michigan University, Kalamazoo, MI 49008
[2]Department of Environmental, Geographical, and Geological Sciences, Bloomsburg University of Pennsylvania, Bloomsburg, PA 17815

INTRODUCTION

This road log and field guide explores the structural geology of the well-known boundary between the Cordilleran thrust belt and the Rocky Mountain foreland between the towns of Three Forks and Whitehall in southwestern Montana. This boundary trends southwest–northeast to west–east and consists of numerous faults and folds collectively known as the southwest Montana transverse zone (SWMTZ, fig. 1A). In this guide we will examine two major faults, and associated folds, in this zone: the Cave fault and the Jefferson Canyon fault (fig. 1B). The Cave and Jefferson Canyon faults form the southern, lateral ramp boundary of the Lombard thrust sheet (Schmidt and others, 2014).

We would like to focus on the following questions:

1. What is the nature of control of the Mesoproterozoic Willow Creek fault (Robinson, 1963) on the Cave–Jefferson Canyon fault system?
2. What control did Rocky Mountain foreland structures have on the geometry and kinematics of the SWMTZ in this area?
3. What is(are) the mechanism(s) of the major hanging wall and footwall folds in this region?
4. How can we explain the change in trend and plunge of the major hanging wall folds from north to south and from west to east in this region?
5. What is the basic structural relationship between the Cave and Jefferson Canyon faults?
6. Which of the two basic sub-Lombard thrust interpretations of the Devil's Fence anticline is the more compatible with the field relationships in this region?

We will propose some answers to these questions, but because they are all open questions, we encourage challenges, discussion, and suggestions.

By way of background, the trend and geometry of the SWMTZ must have been profoundly influenced by the Mesoproterozoic Willow Creek fault of Robinson (1963). Though not exposed, the position of this fault, or fault zone, is inferred from the distribution of the thick (>2,400 m) arkosic diamictites of the LaHood Formation of the Belt Supergroup. These rocks, which occupy the hanging walls of the Cave and Jefferson Canyon faults, indicate that east–west-trending normal fault-bounded highlands, composed of Archean metamorphic basement rocks, shed clastic (dominantly turbidite) sediments to the north into an east–west-trending embayment of the Belt basin. Vuke and others (2014) identify six different facies of the LaHood Formation, from submarine fan, shelf, and slope facies to alluvial fan and fan delta facies. We will examine some of these different facies at Stops 2–5 and 7. The La Hood Formation is absent to the south of the Cave and Jefferson Canyon faults (except, possibly, at one location along Stop 7) and is everywhere allochthonous. We will discuss alternative interpretations of the relationship of the Cave and Jefferson Canyon faults to the Willow Creek fault at Stop 2.

The field trip route along I 90 takes us along the southern part of the Lombard thrust sheet. Besides the details of faulting and folding at Stops 1 and 2, we can consider implications of recent discussions of the "folding" of the Lombard sheet by sub-thrust imbrications, producing the Devil's Fence anticline (culmination) to the north of our route (figs. 1B, 1C). Most participants will be familiar with the Kimpton Ranch well that was drilled into this structure. Alternative interpretations of the well focus on whether it penetrated Cretaceous shales (Ballard and others, 1993; Burton and others, 1996) (fig. 1C) or Mesoproterozoic shales (Schmidt and others, 1990) beneath the thrust.

We will first visit the hanging wall rocks of the Cave–Jefferson Canyon fault system (Stops 1–6) and then the more complicated footwall rocks along a short traverse in Jefferson Canyon (Stop 7 start to

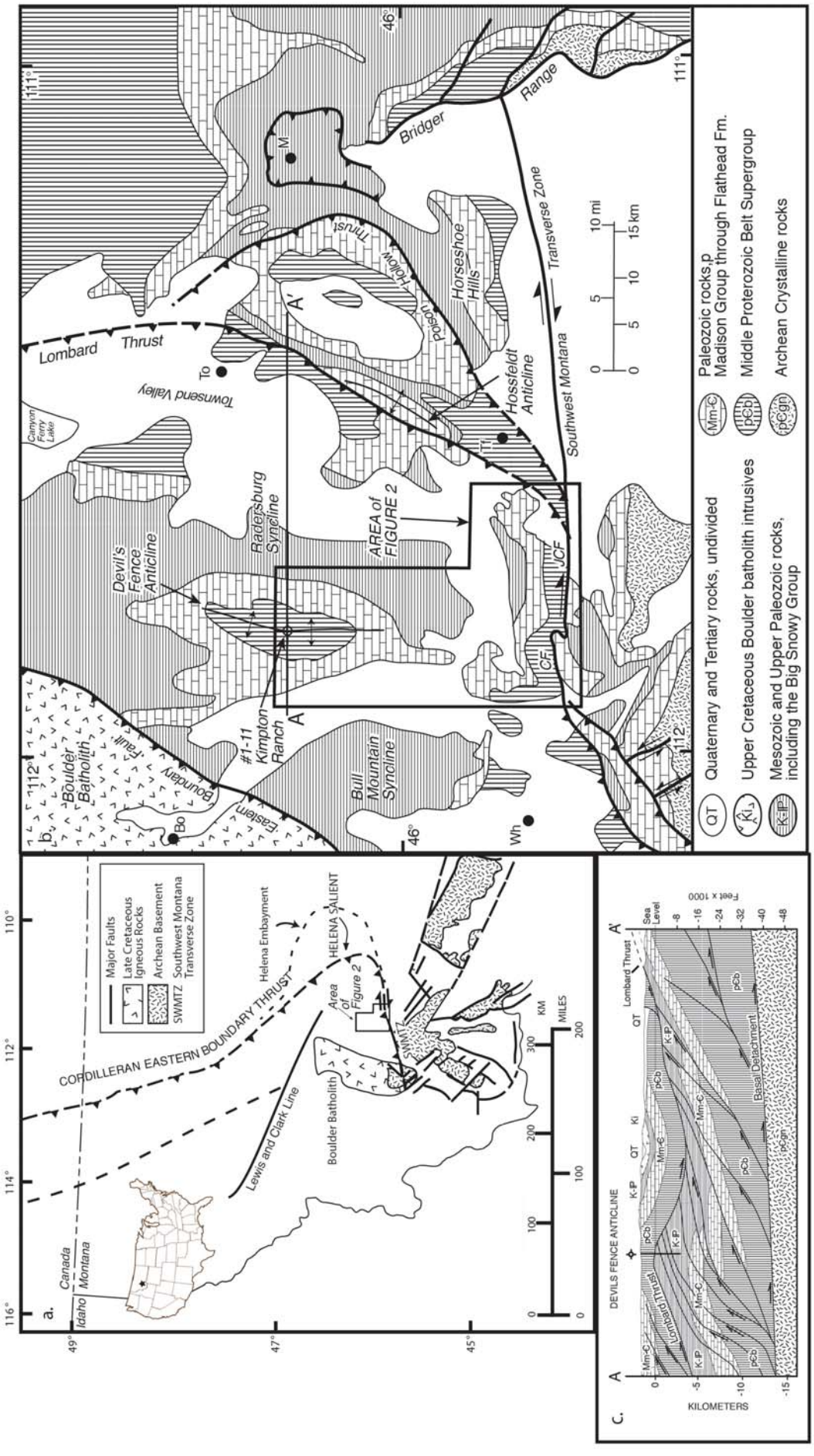

Figure 1. A, Location map showing the position of the study area along the leading edge of the Cordilleran thrust belt in Montana. B, Geologic map of the southern Helena salient and southwest Montana transverse zone showing location of regional section and more detailed map (fig. 2) CF, Cave fault; JCF, Jefferson Canyon fault; Bo, Boulder; M, Maudlow; Tf, Three Forks; To, Townsend; Wh, Whitehall. Modified from Burton and others, 1996. C, Seismically controlled cross section across the eastern Lombard thrust sheet and Devils Fence anticline. After Burton and others, 1996.

Stop 7 end). The final stops (8 and 9) will be on lesser deformed hanging wall rocks. Some of the stops included herein were discussed in a GSA Centennial Field Guide (Schmidt and others, 1987), but the interpretations have changed. Most of the figures have been recycled or modified from recent interpretations of the structure (Schmidt and others, 2014; Whisner and others, 2014).

Although this road log considers only the Cave and Jefferson Canyon faults of the SWMTZ, the zone continues eastwardly to the Pass fault in the Bridger Range where this Rocky Mountain foreland uplift has folded the fault contact between Archean rocks and La Hood rocks (Lageson, 1989) (fig. 1B). It also continues southwesterly across the northern flank of the Tobacco Root Mountains where the principal fault carrying LaHood rocks over the Phanerozoic section is the NE–SW-trending Mayflower Mine fault (Schmidt and Hendrix, 1981). The connection between the Mayflower Mine fault and the Cave–Jefferson Canyon fault system is buried below Cenozoic deposits (fig. 1B).

ROAD LOG

Travel from Bozeman on I 90 East to the intersection with US 287 (about 34 mi). We travel northwestwardly from Bozeman, and near the town of Manhattan, we cross the SWMTZ, which is buried below the Gallatin River Valley–Three Forks basin. Thrusts and folds in LaHood Formation and Phanerozoic rocks are on the north in the Horseshoe Hills (fig. 1B), and rocks (tuffaceous siltstone interbedded with coarse sandstone and conglomerate) of the Madison Valley Member of the Miocene Sixmile Creek Formation are on the south. The structures in the southern Helena salient, from the Lombard thrust eastward to the eastern Horseshoe Hills, were originally mapped by Verrall (1955) and are included in the Bozeman 30′ x 60′ quadrangle (Vuke and others, 2014). The road log begins at the north onramp to I 90 at the intersection of I 90 and US 287.

STOP 1 Mile 0

(45.918°N,111.597°W)

The purpose of this stop is to discuss the regional setting and overview of the Lombard thrust and the mechanism of folding related to thrusting (figs. 1B, 2, and the Bozeman 30′ x 60′ quadrangle).

The trace of the Lombard thrust runs northeast–southwest about 1 km east of this location, below rocks of the Climbing Arrow Member of the Eocene Renova Formation. To the northeast the Lombard thrust and associated folds outcrop in the low-lying hills east of US 287. This area was mapped by Robinson (1967) and is shown on the Bozeman 30′ x 60′ quadrangle. It is along the line of regional cross section E–E′ (to be shown and discussed and eventually included with the geologic map). A southwest-plunging syncline in Upper Cambrian through Mississippian rocks on the hanging wall is thrust over a southeast-verging overturned anticline (Hossfeldt anticline) in rocks of the same age. This anticline was interpreted to be a “kink detachment fold” by Mitchell and Woodward (1988). That interpretation prompted a comment by Schmidt (1988), who argued that the detachment fold idea was incorrect because, among other things, there were no other documented examples of detachment folding with the same wavelength and amplitude in the area, and the LaHood Formation was an unlikely candidate for the thick deformed zone of weak rocks that is required for a detachment fold mechanism. This comment, and the subsequent reply by the authors (Mitchell and Woodward, 1988) led me to a reevaluation of folds that I had assumed to be fault-propagation folds. I concluded (Schmidt and others, 2014; Whisner and others, 2014) that, in fact, there are many other examples of detachment folds in the Lombard thrust sheet and the other thrust sheets east of it. Also, the numerous fine-grained graded beds in facies of the thick LaHood Formation make it ideal for the development of detachment folds above basement. However, the same argument cannot be made for folds in the Phanerozoic section resting unconformably on basement south of the Mayflower Mine, Cave, and Jefferson Canyon faults where no LaHood rocks are present. In cross section E–E’, to be included in the Bozeman quadrangle, I have drawn a section that clearly agrees with the detachment fold interpretation of Mitchell and Woodward (1988). The important observation is that the amount of shortening by faulting is considerably smaller than shortening by folding. We will examine some excellent examples of detachment folding at Stop 2. Dip separation, and presumably net slip, by restoring hanging wall cutoffs to footwall cutoffs on the Lombard thrust, is only about 1.5 km here.

To the southwest of Stop 1 is the Milligan Canyon area, which we will visit at the end of the trip (Stops 8 and 9). In this area the east–west-trending Jefferson Canyon fault is inferred to bend toward the northeast

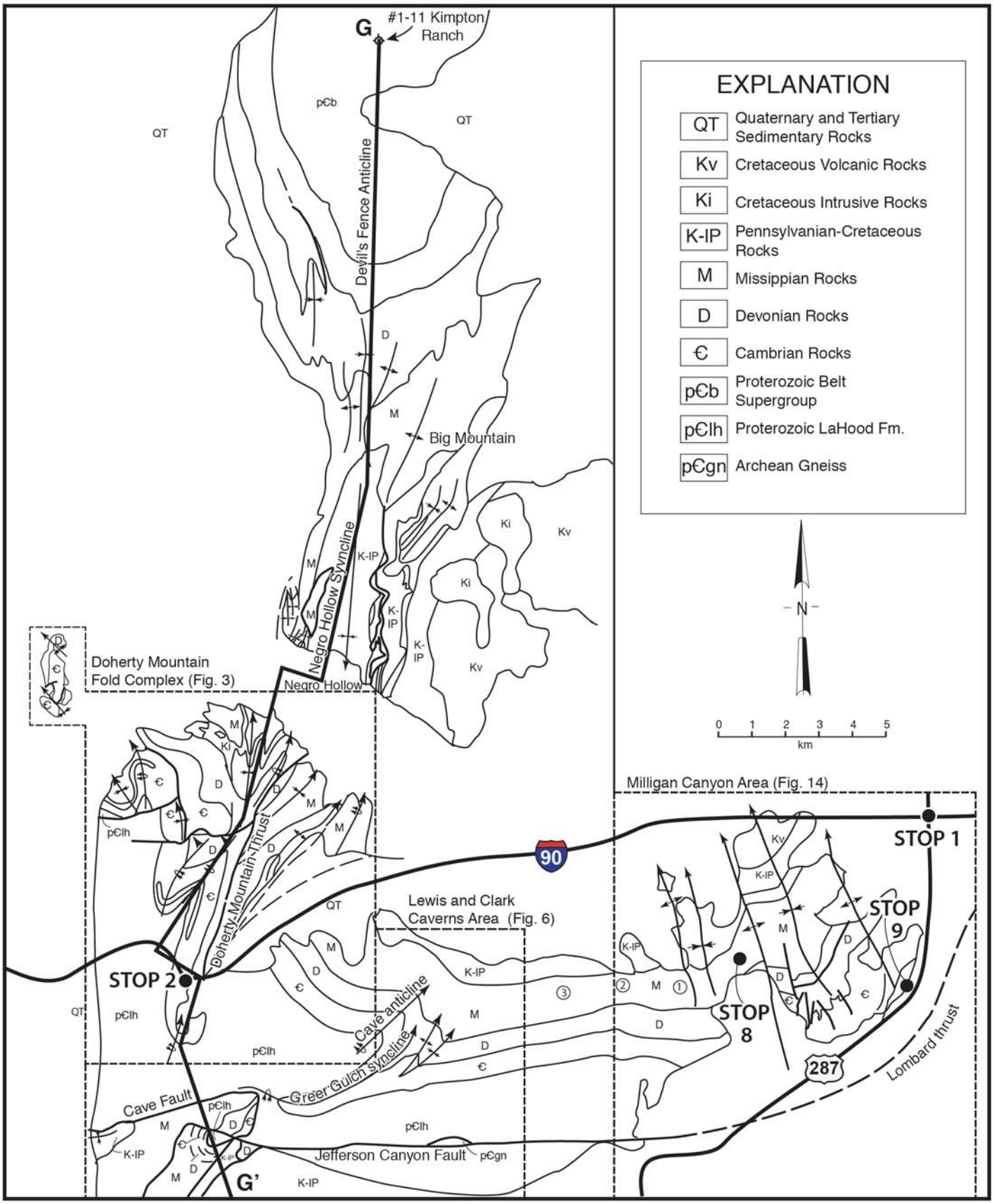

Figure 2. Geologic map of folded rocks of the Lombard thrust sheet from the southern Devils Fence anticline to the Cave–Jefferson Canyon fault system and Milligan Canyon area showing the location of more detailed maps (figs. 3, 6, and 14), the location of the north–south regional cross section (fig. 5), and the locations of cleavage measurements (1, 2, and 3). Northernmost part of map modified from Klepper and others (1957).

to become the Lombard thrust. Whatever value is ultimately chosen for displacement on the Lombard must be compatible with estimates of net eastward translation on the Jefferson Canyon fault.

On the route to Stop 2 we traverse rocks of the Eocene Renova Formation. The hills on the south side of the interstate compose the north-dipping homoclinal panel of LaHood Formation and Paleozoic rocks above the Jefferson Canyon fault. The highest ridge is the Mississippian Mission Canyon Limestone.

STOP 2 Mile 15.3

(45.876°N, 111.894°W)

Pull off on the right shoulder of I 90. Proceed with extreme caution. This stop is an overview of the Doherty Mountain fold complex (DMFC of Whisner and others, 2014) and the Doherty Mountain thrust (DMT) (figs. 2–5).

The DMFC is the southernmost and westernmost set of folds on the hanging wall of the Cave fault (fig. 2). It is composed of a train of at least 14 close to tight (wave length about 2 km), asymmetrical to overturned, east-verging folds (figs. 3, 4). Stop 2 is a few tens of meters west of the hinge of syncline S12 (fig. 3) near the contact between the Cambrian Flathead Sandstone and an outer submarine fan facies of the La Hood Formation (Vuke and others, 2014). We will be able to compare the LaHood facies here with those at Stops 3 and 4 in Jefferson Canyon near the Cave fault. Looking north from here we can see the adjacent fold pair (anticline A10 and syncline S9). The massive Cambrian Meagher Limestone is the cliff former, and the underlying rocks are the Wolsey Shale, Flathead Sandstone, and LaHood Formation. The following discussion of fold orientation, style, and mechanism(s) was extracted from Whisner and others (2014).

Thinned limbs and thickened hinges are common in the DMFC, especially in the less competent formations such as the Cambrian and Devonian shales. Folds vary from concentric to similar in style [class 1b –class 2 (Ramsay, 1967) depending on units involved], with class 1c being the most common style. Fold geometries are frequently distorted by discontinuous, mostly concordant intrusions of intermediate to mafic composition and of Cretaceous age (77 Ma biotite; Harlan and others, 2008). Paleomagnetic fold tests applied to folded sills indicate that most of the folding and all the thrusting was post intrusion, but sills appear to have behaved in a ductile fashion during folding. Although pi-diagrams of poles to bedding for all the folds in the DMFC indicate that the average fold axis orientation is 41°N, fold trend lines converge to the south, and the trend and plunge directions of individual folds are rotated about both vertical and horizontal axes, fanning from northwest to northeast across the area. The change in fold orientation across the DMFC suggests a change in shortening direction across the area from W–E to WNW–ESE. This change will be addressed again at Stop 6.

The geological map, stereonet patterns, and cross sections C–C′, D–D′, and E–E′ (figs. 3, 4) clearly indicate that much of the faulting in the DMFC occurred after significant folding. This is based on the observation that the east-trending fault (decollement) between Regions II and IV cuts across fold hinges and displaces them eastward, and on the inference that movement on thrusts has rotated fold axes toward the northwest, producing the observed dispersion in the pattern of fold axis orientations. In addition, attempts to restore the cross sections make it clear that several folds and fold pairs are entirely missing, likely because they have been cut out by thrusting. The existence of well-developed footwall synclines in the western part of Regions II and III further supports thrusting after folding (e.g., McNaught and Mitra, 1993). This, combined with the dominance of fold shortening over thrust shortening in the area, suggests that the folds began as detachment folds above the Cave fault and were later modified by faulting across fold hinges and steep fold limbs or out of tight synclines. The extreme tightness of the folds and out-of-sequence thrusting here indicates a general increase in internal shortening compared to the areas farther north (Negro Hollow syncline and Devil's Fence anticline). Restoration of section C–C′, for example, indicates an internal shortening of about 55% (24 km) across the DMFC. This does not even account for very early layer-parallel shortening indicated by layer normal cleavage in the Lodgepole Limestone (discussed at Stop 8) and deformed ooids in the Meagher Limestone in the westernmost folds (A1 and S2) (Hendrix and Stellavato, 1976).

The plunge of folds in this part of the Lombard thrust sheet changes systematically from the southern Devil's Fence anticline (DFA culmination) on the north to the DMFC on the south. Folds on the southern DFA plunge gently south and continue their southerly

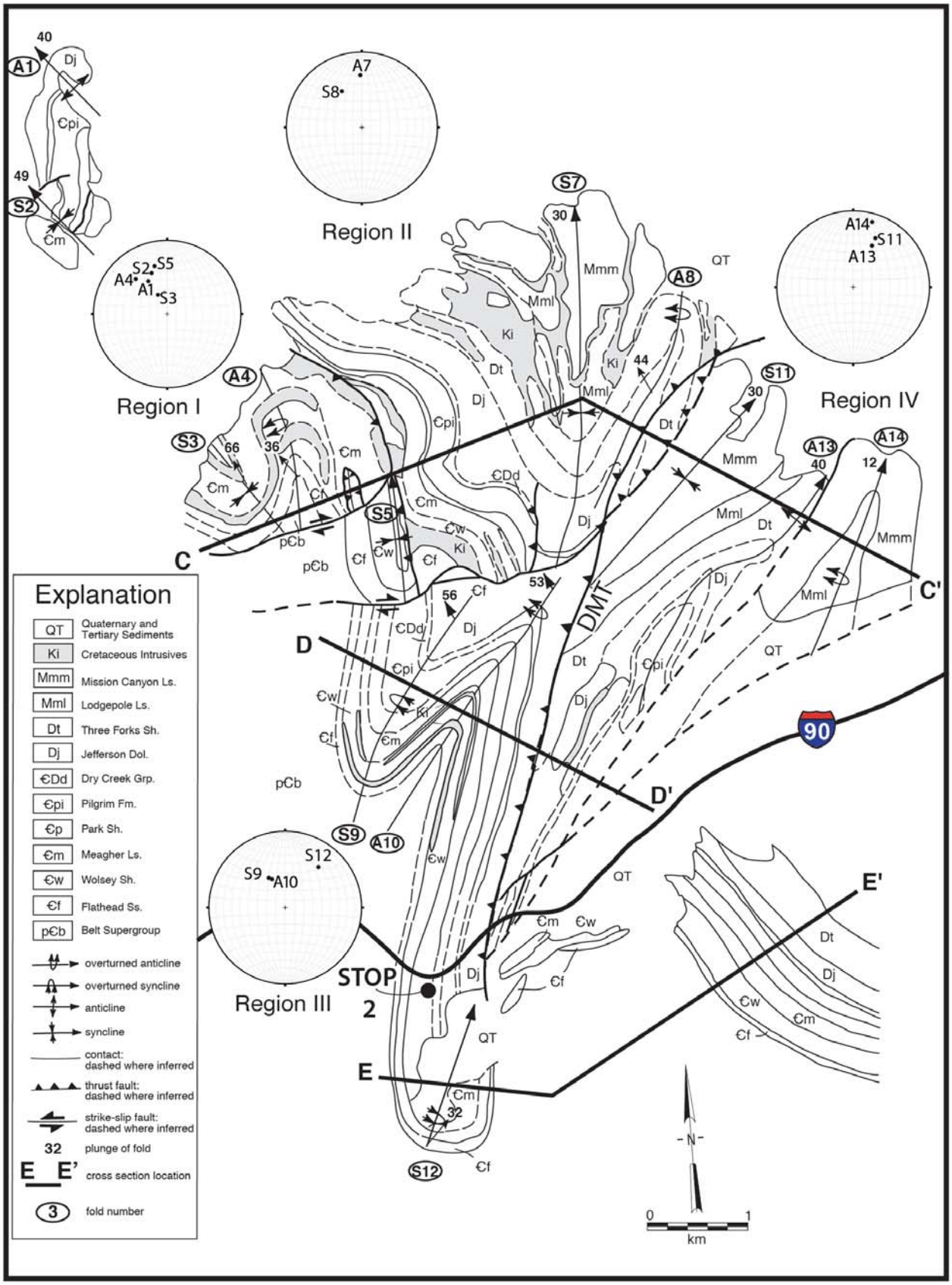

Figure 3. Geologic map of the Doherty Mountain fold complex showing location of subareas (regions I–IV) and cross sections C–C', D–D', and E–E' (fig. 4), and orientations of numbered folds. S, syncline; A, anticline; DMT, Doherty Mountain Thrust.

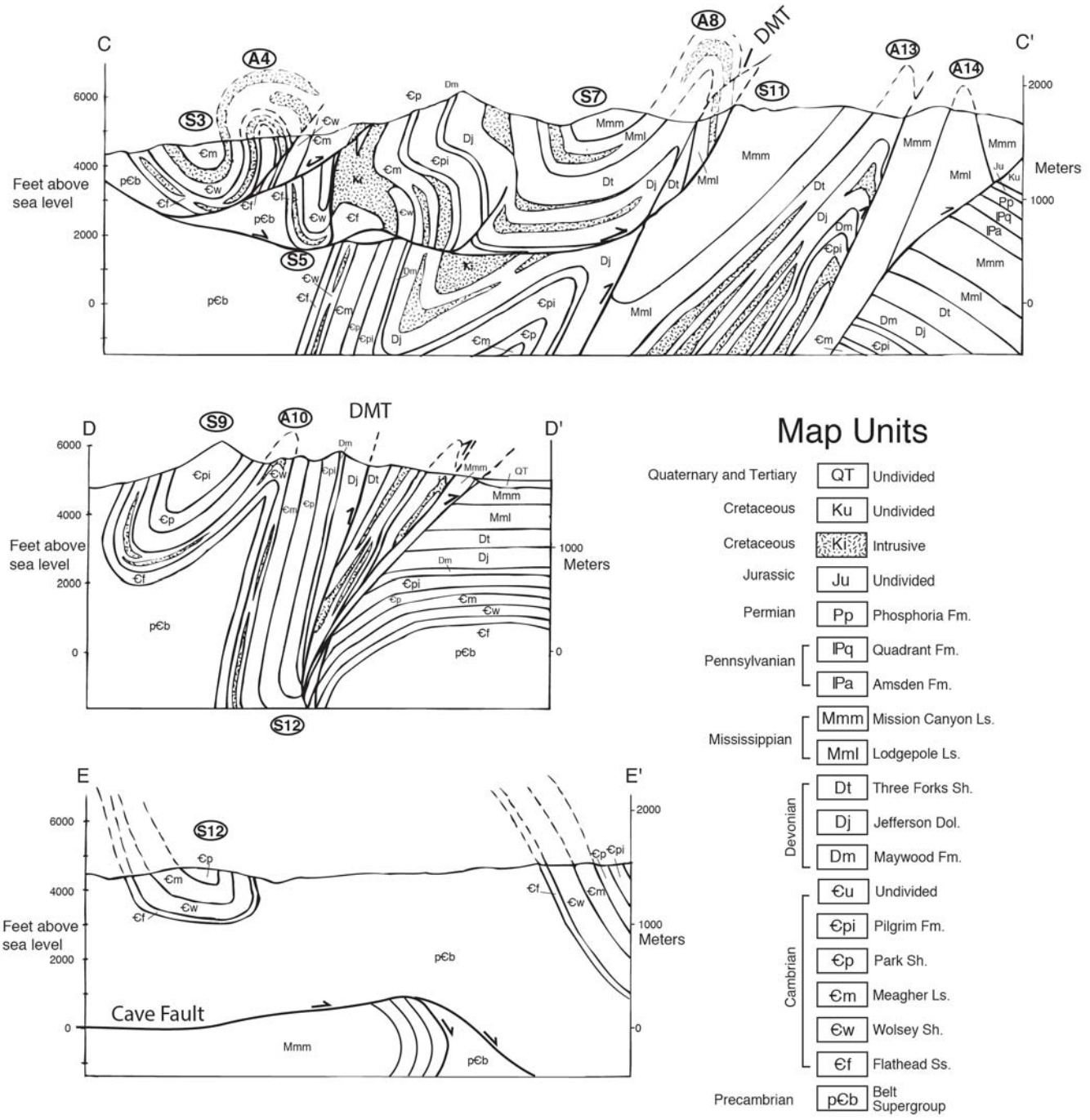

Figure 4. Cross sections C–C', D–D', and E–E' in Doherty Mountain fold complex. DMT, Doherty Mountain Thrust.

plunge in the Negro Hollow syncline (fig. 2). In the DMFC the plunge is reversed towards the north. This change in fold plunge is interpreted to be related to "folding" of the Lombard thrust sheet by upward rotation of Belt and Phanerozoic rocks by the emplacement of the lateral ramp that surfaced as the Cave and Jefferson Canyon faults (Whisner and others, 2014). The N–S cross section (fig. 5) that shows the resulting geometry is an interpretation of the DFA with Cretaceous rocks below the folded Lombard sheet (after Burton and others, 1996). An alternative explanation (Schmidt and others, 1990) has only repeated sections of Belt Supergroup rocks below the Lombard thrust in the DFA culmination. In either case we interpret the basal decollement between Belt rocks and basement to intersect and become the Lombard thrust below the DMFC as it climbs southward above down-dropped steps in the Mesoproterozoic Willow Creek normal fault zone. We consider the alternative explanation, that the Belt rocks were simply inverted along the same normal fault, as in many cases of tectonic inversion, to be less likely, but worthy of further discussion.

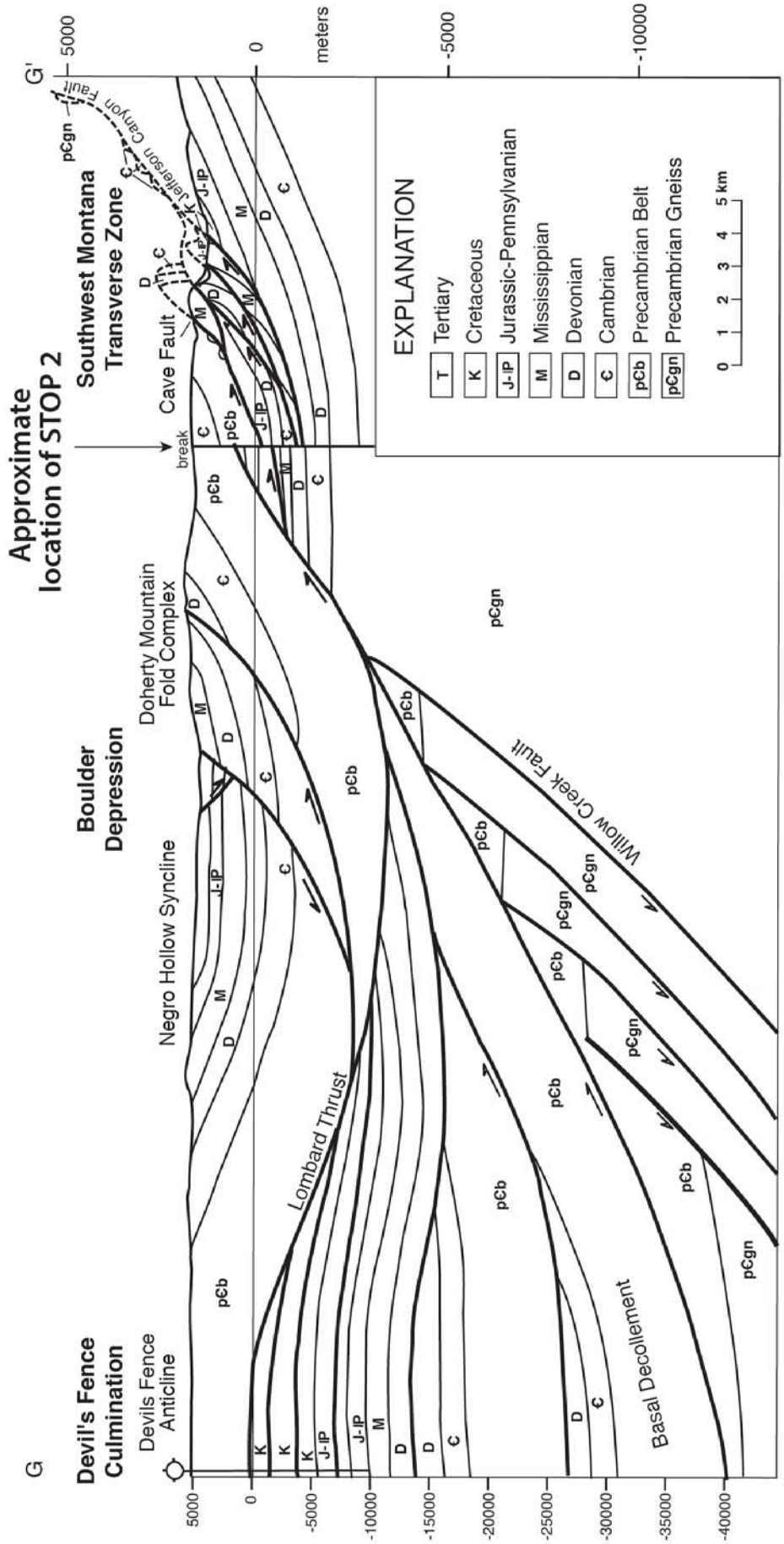

Figure 5. North–south cross section (G–G') from the Devils Fence anticline to the footwall of the Jefferson Canyon fault. Line of cross section shown in figure 2.

Continue 3.3 mi on I 90 to the Cardwell exit and take Montana 2 back east toward Jefferson Canyon. We cross the Starrets Ditch normal fault at mile 20.2 and enter Jefferson Canyon (fig. 6) According to Aram (1981) at least 450 m of down-to-the-west dip separation has occurred on this fault since mid-Pliocene time. This forced the ancestral Jefferson River to abandon its former position and cut down to its present level. This entrenchment is interpreted to have created the canyon and initiated the development of the Lewis and Clark caverns. (See further details in Schmidt and others, 1987.) LaHood Park at mile 20.9 is the site of an old hotel and gas station (destroyed by fire) that played an important role in housing CCC workers who built the original facilities at Lewis and Clark Caverns State Park (Stops 5 and 6).

STOP 3 Mile 21.5

(45.845°N, 111.917°W) (fig. 6)

Park on broad shoulder on the east side of the highway. This stop has been termed "type section gulch" after Hawley and Schmidt (1976). The type section of the La Hood Formation, first described by Alexander (1955), begins about 600 m up this gulch. We will examine a "typical" exposure of this facies, interpreted as a submarine fan. A massive "rubble bed"/olistostrome can be seen on the rocky bluffs to the east with pegmatite blocks from 15 to 30 m across.

The LaHood Formation was defined by McMannis (1963) as "all dominantly coarse Belt strata along the southern margin of the Belt geosyncline" (basin). Hawley (in Schmidt and others, 1987) estimated that the LaHood Formation is at least 2,400 m thick in this area, allowing for folding and the fact that the section is continuous from the Starrets Ditch fault to the contact with the Cambrian Flathead Sandstone in syncline S12 (fig. 6). Hawley also noted that the angular discordance between the Flathead and the LaHood varies from place to place between 17°and 51°. There are also places (e.g., Stop 7 traverse and Stop 9) where the Flathead is absent and the LaHood is in depositional contact with the Woolsey Shale, an indication of "islands" or high areas of LaHood rocks above the transgressing Cambrian sea (Robinson, 1963; Graham and Suttner, 1974).

Several tight, SE-verging, NE-plunging, asymmetrical to overturned folds in the LaHood here mark the southern extent of the detachment folds of the DMFC on the hanging wall of the Cave fault (fig. 6). These folds were mapped with the aid of facing direction in graded beds. The facing direction of the vertical beds here in this outcrop is reasonably clear.

STOP 4 Mile 22.4

(45.835°N, 111.910°W) (figs. 6–10)

The purpose of this stop is to view, describe, and review the significance of the Cave fault. The following description below is modified from Schmidt and others (2014). The Cave fault (Alexander, 1955) strikes ENE and dips steeply NNW (55–75°). Measurements of minor folds on the footwall and of slickenlines on the fault surface at two locations indicate that the latest movement on the Cave fault was oblique slip with nearly equal components of dextral and reverse slip. Dip separation is between 900 and 1,800 m along most of the fault where the LaHood Formation is in fault contact with overturned Mississippian Mission Canyon Limestone (fig. 7). Net slip is between 1,200 and 2,400 m (Schmidt and others, 1987). The hanging wall structure due north of the Cave fault is the tightly folded NNE-plunging train of large folds of the DMFC in the LaHood formation and lower Paleozoic rocks (fig. 6).

One of the large NW-plunging basement-cord anticlines (London Hills anticline) of the Rocky Mountain foreland plunges beneath the Cave fault (figs. 6 and 8), but the fault cuts straight across the northernmost part of this earlier structure (Schmidt and others, 1988), suggesting that most of the regional dips of the Paleozoic and Mesozoic rocks on the footwall of the Cave fault were produced before most or all of the movement on the fault.

The principal fault-related structure on the footwall of the Cave fault is a very tight overturned syncline (Cave syncline) in Upper Paleozoic and Mesozoic rocks (figs. 7, 9, 10, section A–A′). Where the fault and fold are best exposed (fig. 7), the fault zone contains a large overturned horse block of Cambrian Meagher and Woolsey Formations above the syncline. Because of the westerly plunge of the syncline, progressively older rocks are exposed on the footwall of the Cave fault as the fault is traced northeastward. The faults on the southeastern side of section A–A′ will be considered at the end of the traverse at Stop 7. The footwall syncline of the Cave fault and the fault-fold relationships shown on the southeast side of

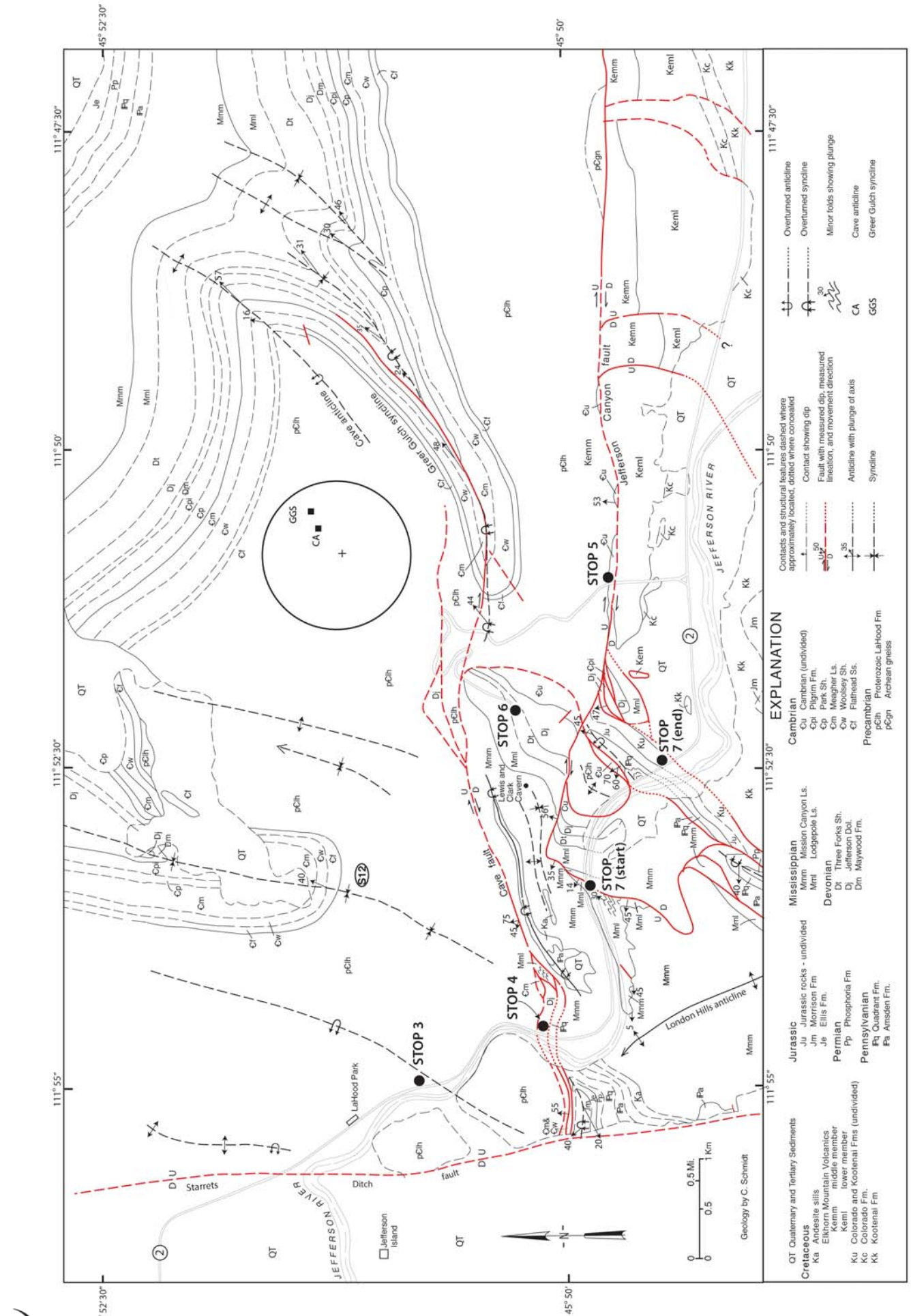

Figure 6. (Simplified) geologic map of the Lewis and Clark Caverns area showing locations of Stops 3–7. Stereonet plot of the orientation of axes of the Cave Anticline (57°, 42°) and Greer Gulch syncline (36°, 50°). Modified from Schmidt and others, 1987.

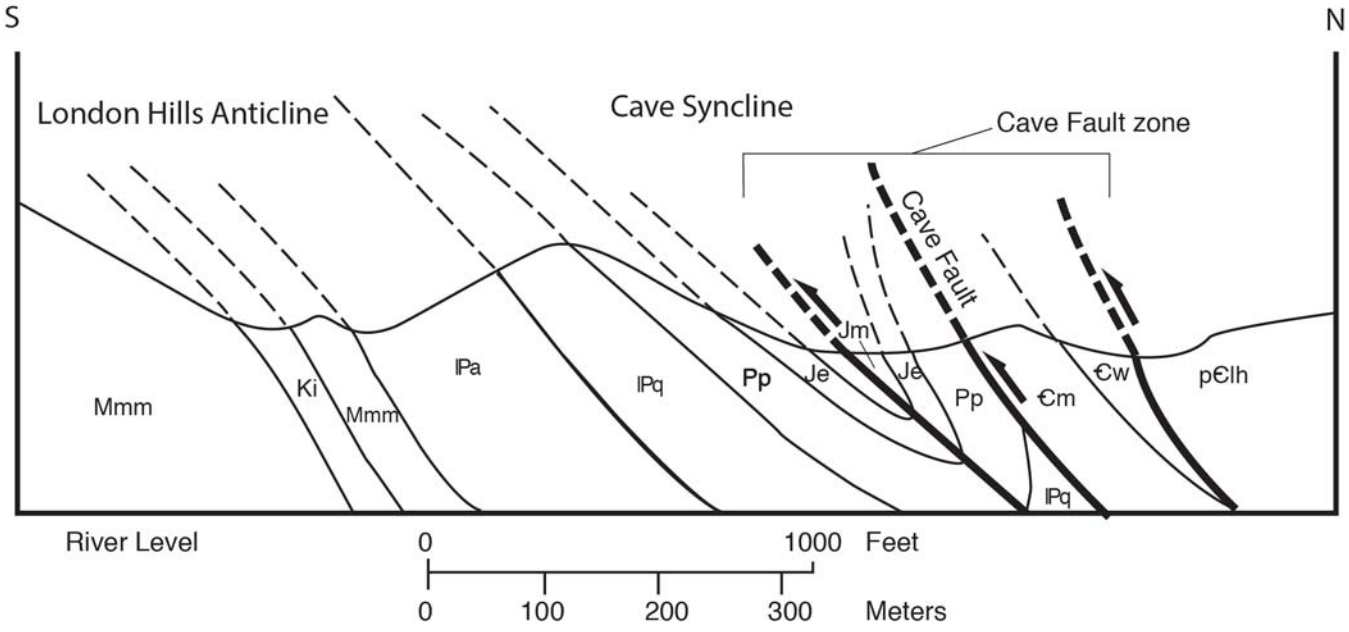

Ki	Andesite sill	Je	Ellis Group
Mmm	Mission Canyon Limestone	Jm	Morrison Formation
IPa	Amsden Formation	Ꞓm	Meagher Limestone
IPq	Quadrant Formation	Ꞓw	Wolsey Shale
Pp	Phosphoria Formation	pЄlh	LaHood Formation

Figure 7. Sketch cross section and photograph (looking west) of the Cave fault zone and Cave syncline. North dips of the Mississippian through Jurassic section are inferred to be on the northern part of the London Hills anticline and were present before the emplacement of the Cave fault.

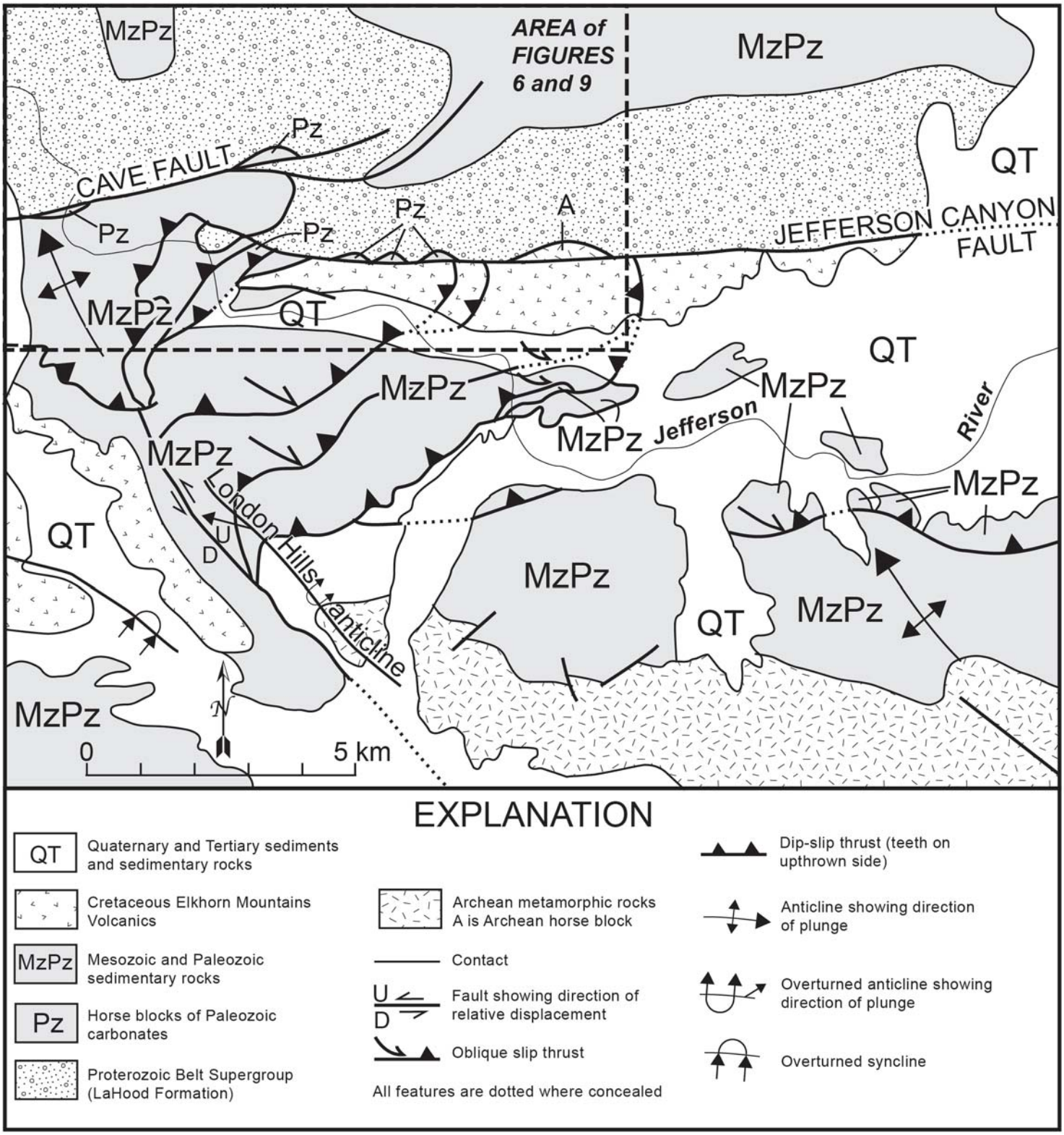

Figure 8. Geologic map of the structural elements of the Jefferson Canyon fault system and their relationship to the basement-cored London Hills anticline and other footwall structures in the south. Location of figures 6 and 9 is shown. Adapted from Schmidt and O'Neill (1983).

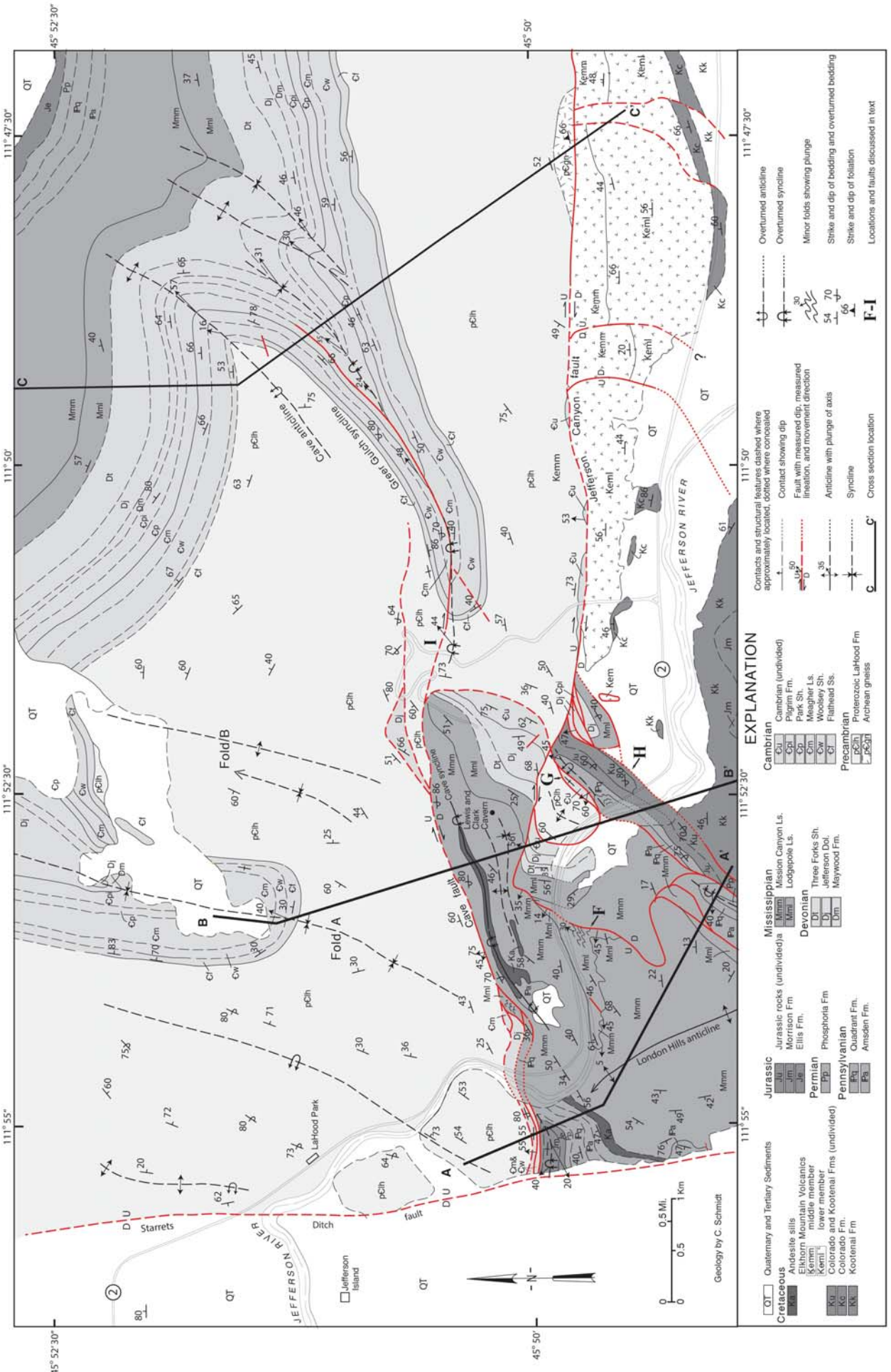

Figure 9. Detailed geologic map along Jefferson Canyon and Cave fault. Cross sections are figure 10 (A–A' and B–B') and figure 12 (C–C'). Detachment folds A and B are discussed at Stop 6 and are shown in figure 13.

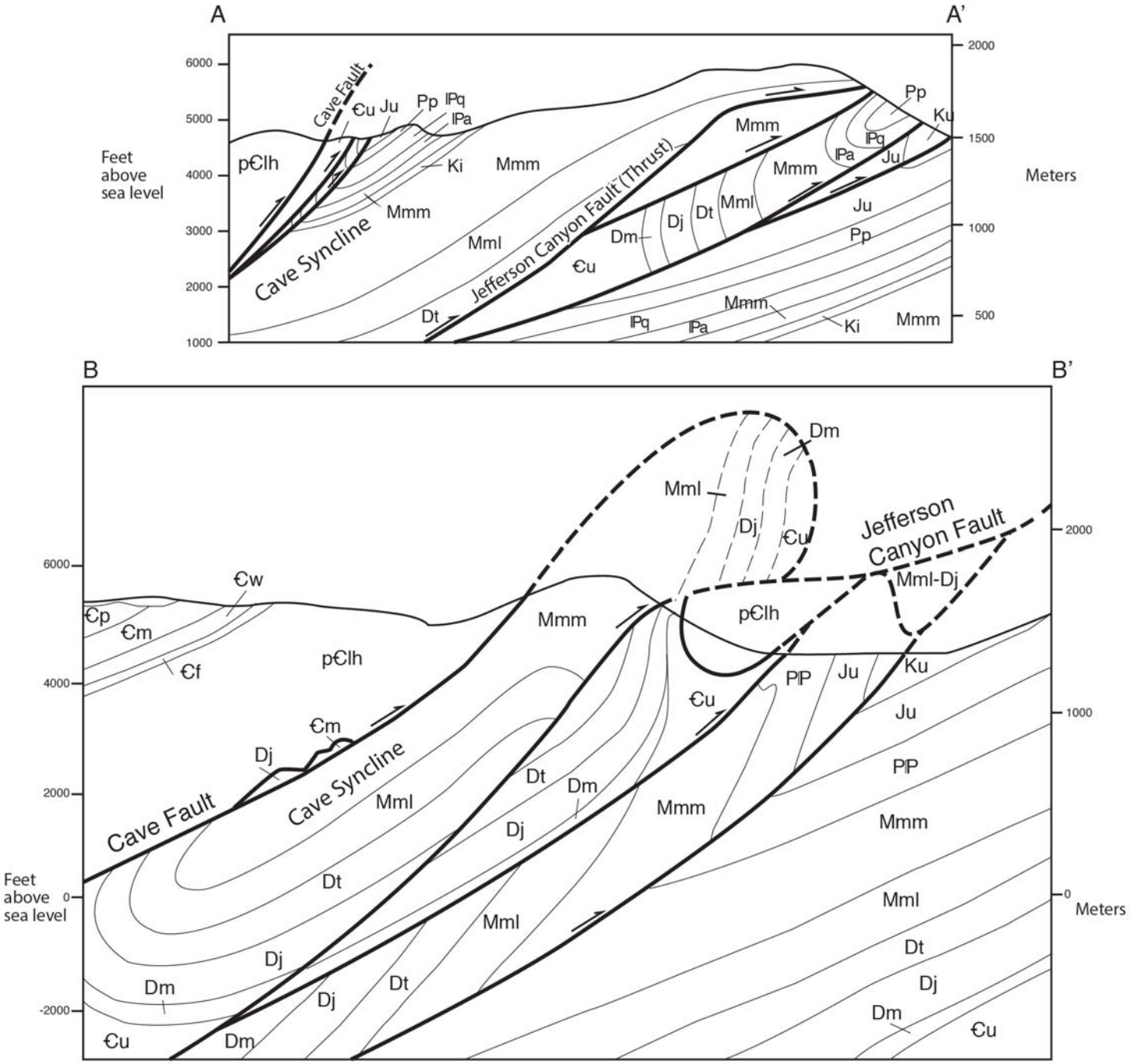

Figure 10. Cross sections A–A' and B–B'. Cross section locations shown in figure 9. Large horse block of Mmm in A–A' is assumed to have been derived from the lowest footwall rocks in the section and indicates out-of-sequence faulting. Section B–B' shows folding of the Cave–Jefferson Canyon fault system and later reactivation of the Jefferson Canyon fault.

the cross section have a geometry that is much more compatible with a fault-propagation fold mechanism, as opposed to the detachment fold mechanism that is ubiquitous on the hanging wall of the faults containing the LaHood Formation at the base of the stratigraphic section. This observation is true for the folds in the SWMTZ across the northern Tobacco Root Mountains as well. The folds and faults in the Phanerozoic rocks south of the Mayflower Mine fault are more compatible with a fault-propagation mechanism than those containing LaHood rocks on the hanging wall of the Mayflower Mine fault.

The Cave fault changes trend from E–W to NE–SW in less than a kilometer east of Stop 4 (fig. 6) and ultimately splits into four segments, two of which we will examine at Stop 6. The change in trend is probably related to the folding of the Cave fault that we will discuss at Stop 6.

Continue south and east on Montana 2 past the location of Stop 7 (mile 23.8), which is on the footwall

of the Cave–Jefferson Canyon fault system. At mile 26 turn left (north) at the entrance to the Lewis and Clark Caverns State Park and proceed on the park access road to Stop 5, 0.5 mi north of the entrance.

STOP 5 Mile 26.5

(45.828°N, 111.851°W)

The park access road cuts through the Jefferson Canyon fault here. The purpose of this stop is to examine the fault zone and the carbonate rocks caught within it. The LaHood Formation (submarine fan facies) and a sliver/horse block of Cambrian rock are faulted against mudflows of the Upper Cretaceous Elkhorn Mountains Volcanics, the youngest rocks to be involved in thrusting. The Cambrian rocks caught in the fault zone are probably mostly the "Silver Hill" member of the Woolsey Shale. The fault here strikes E–W and dips about 40° to 60°N. Based on the position of similar rocks on the footwall in Jefferson Canyon (at Stop 7), the strike separation is about 3 km. Dip separation is indeterminant, but the N–S cross section (fig. 5) may give a rough idea. Stratigraphic separation is about 5 km. Orientation of 115 slickenlines in the fault zone on fault-parallel fractures in this area and approximately 10 km east of here indicates the latest movement was oblique slip (right-reverse), with the dip-slip component slightly greater than the dextral component (Schmidt and Hendrix, 1981). Horse blocks of Cambrian, Devonian, and Mississippian carbonates, as well as a large (700 m x 200 m) block of Archean basement (4 to 5 km east of Stop 5), are caught in the fault zone. These blocks are interpreted to have been "picked off" one or more down-dropped hanging wall blocks of the Willow Creek fault zone as depicted in figure 5. They are all intensely fractured and brecciated, especially in the brittle dolostones of the brittle Devonian Jefferson Formation. These blocks may have been significant in impeding or locking the early movement along the Cave–Jefferson Canyon fault system, leading to folding of the Cave fault (discussed at Stop 6). Continue via the park access road to Stop 6.

STOP 6 Mile 29.2

(45.839°N, 111.851°W)

Park in the lower parking lot of Lewis and Clark Caverns State Park. At this stop we will consider the hanging wall structure of the Cave fault, large folds (Cave Anticline and Greer Gulch syncline on the hanging wall of the Jefferson Canyon fault), the footwall rocks of the Cave fault, and the hypothesis that the Cave fault and Jefferson Canyon fault are different parts of the same detachment modified by folding.

Hanging wall of the Cave fault: Although the stop is on the footwall of the Cave fault, we can talk about the hanging wall structure and point to a map from here. The map pattern (figs. 6, 9) is critical to the interpretation of the relationship between the Cave and Jefferson Canyon faults. Our interpretation is that the Cave fault is the folded western part of a once continuous E–W-trending detachment surface (Schmidt and others, 2014). The hanging wall structures on the north side of the prominent ridge of the Mission Canyon Limestone largely reflect the later movement on the Cave fault portion of the detachment. The detachment folds of the DMFC that we observed at Stop 2, and discussed again at Stop 3, intersect the ENE-trending Cave fault obliquely, suggesting a NW–SE shortening direction resulting in right-hand reverse slip on the fault. Slickenlines in the fault zone indicate the same sense of oblique slip (fig. 6). Initial movement on the Cave fault was likely to have been largely right-hand strike slip (before folding) when it trended E–W.

The Cave fault loses displacement toward its northeastern trace immediately north of this stop, perhaps cutting across a footwall high, and begins cutting down section in the transport direction. The fault also splays into several segments here. Two of the splays surround a large horse block of Devonian Jefferson Formation. Another splay cuts through the synclinal hinge of a large NE-plunging fold pair about 2 km directly east of us, and another turns abruptly south and can be traced directly east of us.

Hanging Wall Structure of the Jefferson Canyon Fault

The following discussion is extracted from Schmidt and others (2014). The principal hanging wall structure of the Jefferson Canyon fault is a fold pair called the Cave anticline and Greer Gulch syncline (Schmidt, 1975). It is the easternmost pair of the fold train described above on the hanging wall of the Cave-Jefferson Canyon fault system (fig. 6). The orientation and geometry of this fold pair is significantly different from that of the detachment folds of the DMFC in that both fold axes trend 20° to 40° more easterly and the axial surfaces strike much more easterly. The anticlinal axis is somewhat more steeply plunging (57°)

than the synclinal axis (21° to 44°). The synclinal axis is progressively more gently plunging in the younger formations up to the Devonian Jefferson Formation (fig. 6).

A down-plunge profile of the fold pair was constructed using the mean trend and plunge (41°, 48°). (This profile is not in the field guide but will be shown.) The profile shows a nearly concentric fold style in most of the formations of the anticline, but considerable thinning (30%) occurs on the overturned part of the forelimb just above the Greer Gulch thrust. As previously mentioned, this fault is a splay of the Cave fault that cuts across the mutual limb and parallels the hinge surface of the Greer Gulch syncline. The position of the Greer Gulch thrust relative to the hanging wall anticline and footwall syncline is well-exposed in two places within the Cambrian Meagher Limestone (fig. 11). Massive beds of the Meagher on the gentle limb of the Greer Gulch syncline dip 40°N and are folded tightly to 80°N overturned. These overturned beds are cut by the north-dipping Greer Gulch thrust with a footwall cutoff angle of about 50° (fig. 11A). The exposed hanging wall rocks are overturned and dip gently 30° to 40°N. At approximately 50 m up section and 100 m to the east, the massive, overturned, hanging wall beds in the limestone parallel the Greer Gulch thrust just below the hinge of the Cave anticline (figs. 11B, 11C). The vertical footwall beds consist of thinly bedded Meagher formation. These beds contain bedding-normal calcite veins as much as 2 cm thick (fig. 11C) and represent approximately 20% layer-parallel extension on the vertical limb below the thrust. The footwall cutoff angle is 65–68°. The thrust is oriented 280°, 22°N, and well developed; slickenlines on the hanging wall fault surface trend N 5°E, nearly down dip. The fault is thrust-slip with N–S shortening at this position in the Cave–Greer Gulch fold pair. The total amount of slip probably does not exceed 100 m. There is not nearly enough fault slip here to accommodate the large amplitude of the fold pair. Although

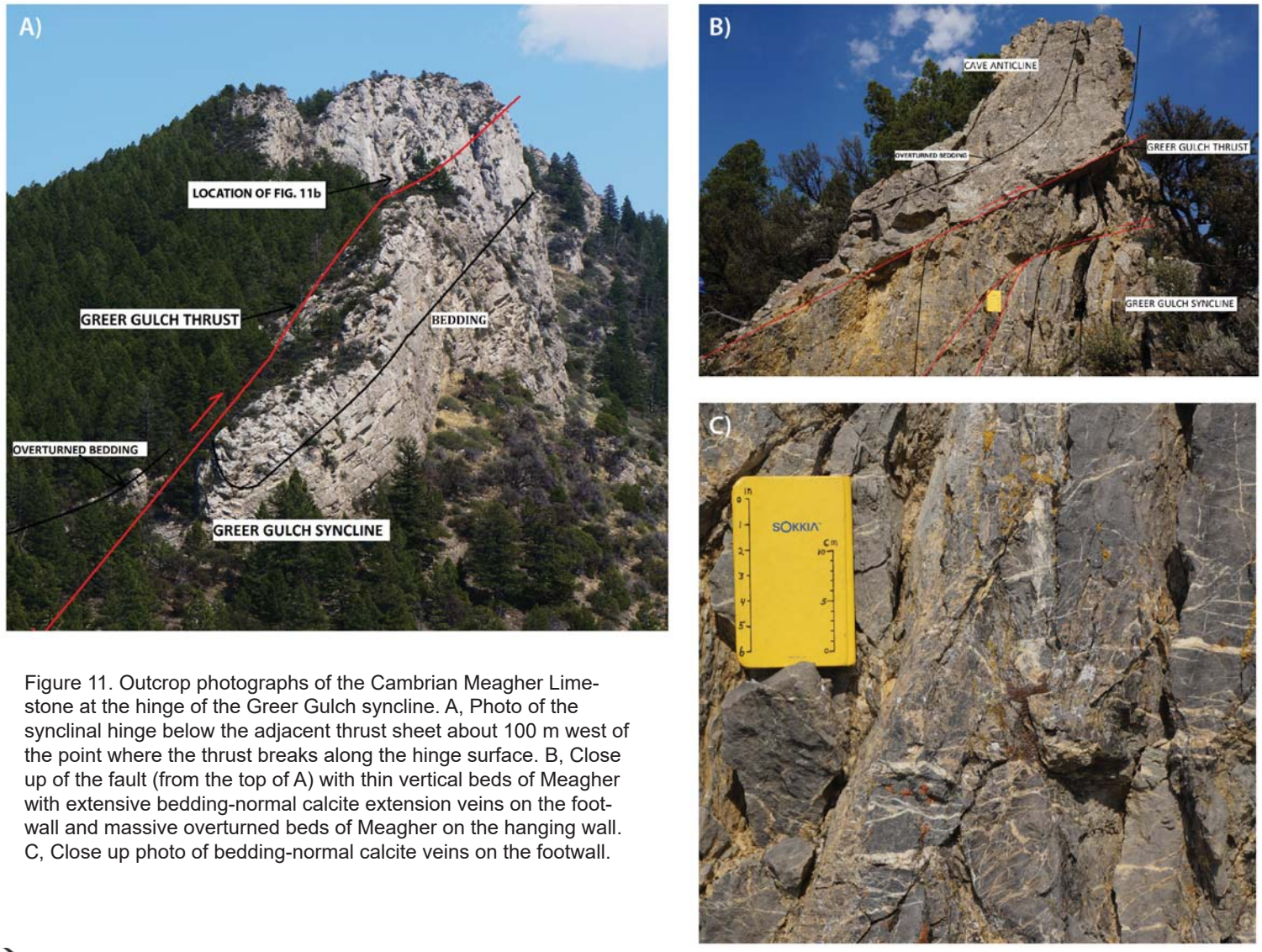

Figure 11. Outcrop photographs of the Cambrian Meagher Limestone at the hinge of the Greer Gulch syncline. A, Photo of the synclinal hinge below the adjacent thrust sheet about 100 m west of the point where the thrust breaks along the hinge surface. B, Close up of the fault (from the top of A) with thin vertical beds of Meagher with extensive bedding-normal calcite extension veins on the footwall and massive overturned beds of Meagher on the hanging wall. C, Close up photo of bedding-normal calcite veins on the footwall.

there are observed examples of fault-propagation folds in which fold limbs are broken as a result of continued tip propagation (e.g., Alonso and Teixell, 1992), the Greer Gulch thrust very likely cut through the steep limb of the fold after nearly all of the folding was completed and was active after the mutual limb of the fold pair was overturned. Like the rest of the folds in the DMFC, this fold pair likely initiated as detachment folds and was rotated significantly to a more easterly trend.

The structure section of the fold pair (C–C′, fig. 12A) was constructed from the down-plunge section (see Schmidt and others, 2014, for details). We area-balanced the fold pair between the pin lines shown using estimates of the original thicknesses of the thinned units (fig. 12B). The section will help to explain the inferred connection between the Cave fault and the Jefferson Canyon fault.

Footwall Structure of the Cave Fault

The final splay of the Cave fault bends southward where it diverges away from the Greer Gulch thrust splay. It crosses the park access road about 0.5 km north of this stop location, and we will take a short hike to look at the highly deformed footwall in the Mississippian Lodgepole Limestone in the fault zone. South from this location the fault cuts down section in the footwall to where it bends sharply eastward and is cut by the Jefferson Canyon fault. (figs. 6, 9). We will examine this part of the fault at Stop 7.

The relationship between this segment of the Cave fault and the Greer Gulch fold pair was suggested to us by the up-plunge region of the down-plunge profile we constructed to draw cross section C–C′. It is apparent from the cross section that the Cave fault was folded along with the folding of the fold pair. Removing the later movement on the Jefferson Canyon fault (moving intersection point C back to B) produces an inferred folded Cave–Jefferson Canyon detachment (inset section of fig. 12A) that closely mimics the shape of the folded Flathead Sandstone in the fold pair above it. Restoration of the folding and faulting, using dashed lines X–X′ and Y–Y′ as pin lines, indicates that about 900 m (18%) of shortening occurred on the Cave–Jefferson Canyon fault before the detachment itself was folded (details described by Schmidt and others, 2014). By this reasoning the Cave and Jefferson Canyon faults are part of the same fault that was folded after some amount of earlier movement had occurred along it and some amount of detachment folding had occurred above it. The inferred sequence, shown in a diagrammatic map view (fig. 13), indicates initial layer-parallel shortening (fig. 13A, as indicated by cleavage in the Lodgepole Limestone, discussed at Stop 8) followed by initiation of detachment folding in LaHood and younger rocks. Folding of the Cave fault section of the detachment began when movement on the Jefferson Canyon section of the detachment became locked, perhaps because of "resistance" to movement created by the presence of large horse blocks in the fault zone or by initiation of faulting from below (fault F, fig. 13C). Lockup of movement on the Jefferson Canyon fault segment initiated regional right-hand simple shear that caused detachment folds above the Cave fault segment to tighten and start to rotate. The mutual limb of the Cave anticline–Greer Gulch syncline rotated and thinned between fixed hinges and younger formations above the Cambrian Meagher Formation were disharmonically folded in the hinge region of the syncline (figs. 13C, 13D). Folding of the Cave fault segment stalled but movement was resumed on the upper, unfolded, part of the Cave fault, translating the horse block of Jefferson Formation (labeled Dj) about 100 m eastward on the northernmost splay, followed by initiation of the Greer gulch splay and propagation into the Greer Gulch syncline about 100 m, tipping out in Cambrian shales on the overturned limb (fig. 13E). Movement on fault F on the footwall of the Jefferson Canyon fault continued and linked up with that fault, producing approximately 700 m of additional right lateral displacement on the Jefferson Canyon fault segment (fig. 13F). We will examine and discuss this later movement along a traverse beginning at Stop 7. Return to the park entrance and turn right (west) and proceed back into Jefferson Canyon.

STOP 7 Mile 36.6

(45.831°N, 111.866°W)

Pull off on the right side (north) on the gravel parking area just west of Stop 7 below the abandoned Limespur quarry, where Mission Canyon Limestone was quarried in the early 1900s for flux material in Butte smelters. The following description, extracted from Schmidt and others (1987), applies to a west to east traverse just east of the parking area. Please use caution on this narrow part of Montana 2.

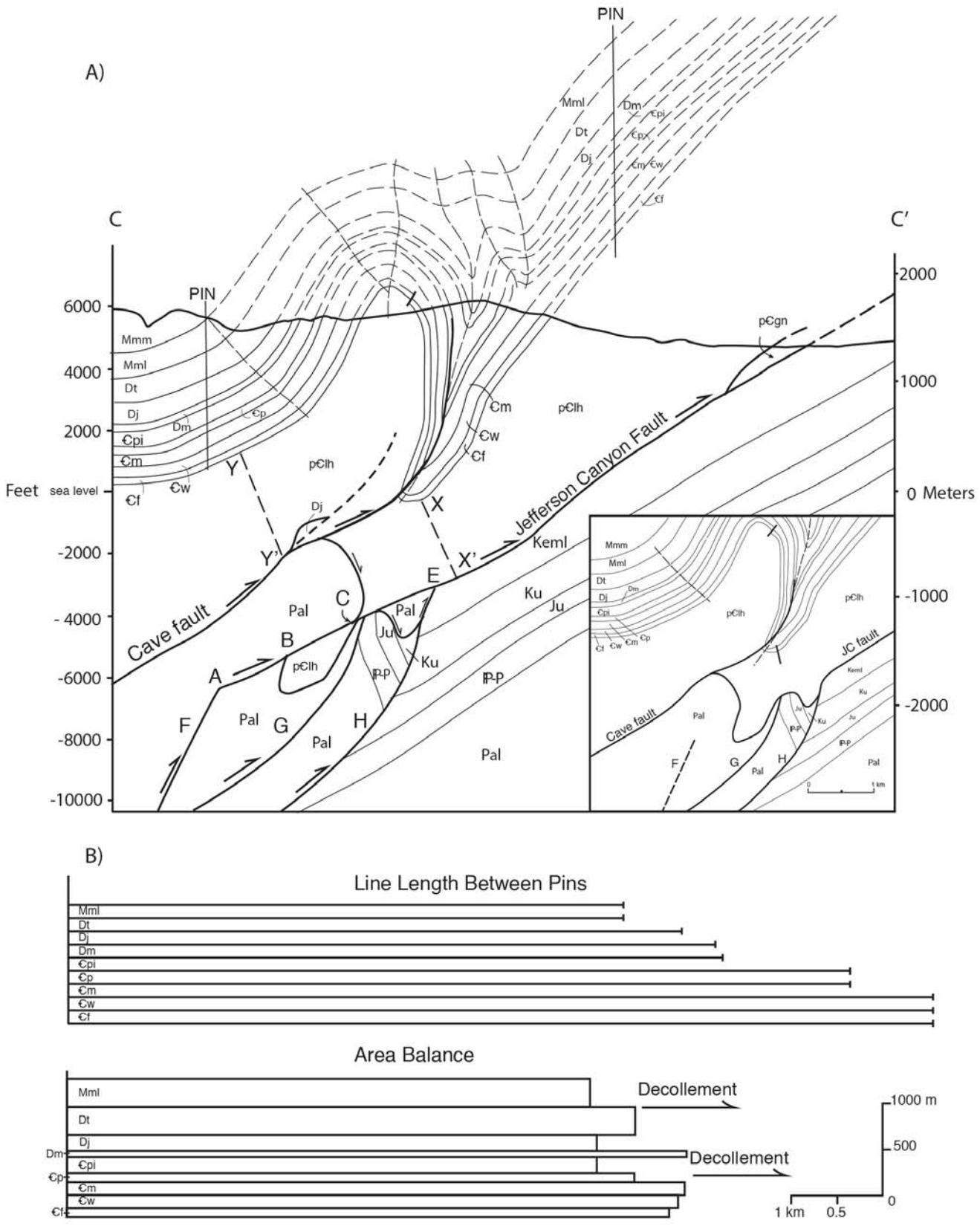

Figure 12. A, Cross section C–C' of the Cave–Greer Gulch fold pair and Cave–Jefferson Canyon fault system based on a down-plunge section (to be shown at Stop 6). Pin lines were chosen for area balance of the fold pair (fig. 12B). Reference lines X–X' and Y–Y' are discussed in text (Stop 6). Locations A–E and faults labeled F–H are also discussed in text. Inset map is the inferred configuration of the faults and folds prior to the last movement on the Jefferson Canyon fault when intersected by fault F. B, Line lengths and areas for the cross section between the pin lines shown in A.

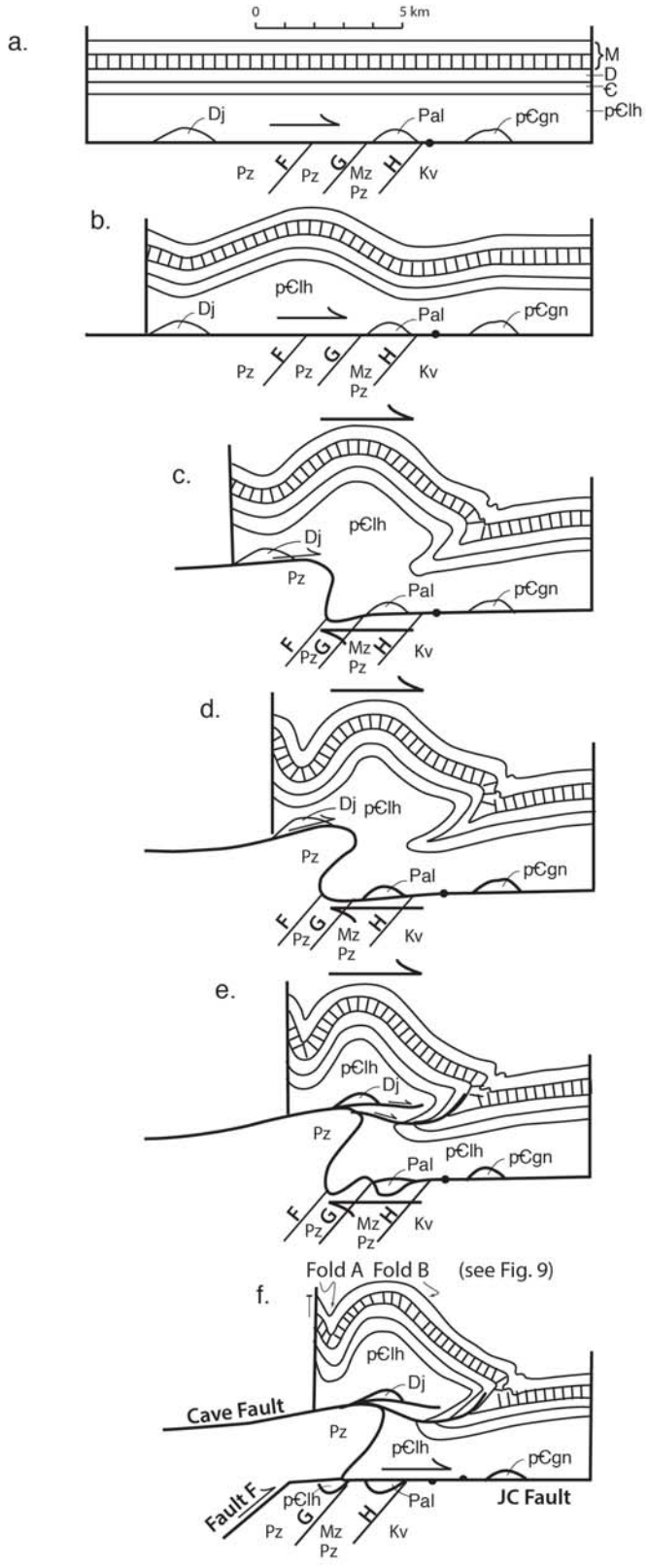

Figure 13. Sequence diagram showing initial detachment folding, folding of the detachment, and modification of the Greer Gulch fold pair. Sequence is discussed in text. Cleavage in Mississippian Lodgepole limestone shown schematically with layer-parallel lines. Horse blocks are Dj (Jefferson Formation), Pal (Paleozoic, principally Mississippian and Devonian rocks), and pCgn (Precambrian basement gneiss). F, G, and H are thrusts (from fig. 9) on footwall of the Jefferson Canyon fault. Pz, Paleozoic rocks; Mz, Mesozoic rocks; Kv, Cretaceous volcanic rocks.

At the starting point near the quarry the massive bedding of the Mission Canyon Limestone dips 30°–50° NW on the northeastern flank of the London Hills anticline. The contact between the Mission Canyon Limestone and the underlying, more thinly bedded Lodgepole Limestone is easily recognized in the cliff face along the highway. A short distance eastward from this contact is the first exposure of the Jefferson Canyon fault. Here the fault dips 58°W and follows bedding in the Lodgepole which is thrust over the more massive and pervasively fractured lower portion of the Mission Canyon. Stratigraphic throw is only about 61 m. The fault (thrust) is also exposed across the river on the south side of the canyon. Numerous minor folds are developed in the Lodgepole on the hanging wall, and several may be seen from the highway. The folds verge east and trend parallel to the fault, suggesting primarily dip-slip movement. This is confirmed by down-dip slickenlines on the fault lines at one location. Along the highway, the contact between the Mission Canyon and Lodgepole may be observed again on the footwall, a very short distance east of the fault.

Just east of the last roadcut of the Lodgepole, the Jefferson Canyon fault bends sharply eastward in the cliffs above the highway. The fault dips 35°W before the abrupt bend and 56°N after it bends eastward. The hanging wall rocks are the steep cliffs of Mission Canyon Limestone. On the footwall an entire vertical section, from Lodgepole on the west to LaHood Formation on the east, strikes north into the east–west trace of the fault. Near the fault the section is bent into a more easterly strike, which probably reflects a significant dextral movement. Portions of the stratigraphic section are absent because of tectonic thinning but the conspicuous absence of the Flathead Sandstone above the highway is due to non-deposition, and the Woolsey Shale is in contact with the LaHood Formation (Graham and Suttner, 1974).

For nearly 1.6 km along the trace of the fault, younger rocks are thrust on older rocks and stratigraphic throw increases rapidly eastward between here and the state park access road (fig. 6). The younger-on-older relationship is likely related to the same sub-thrust structural high that caused the folded Cave fault section to cut down section in the transport direction. We have no reasonable explanation for the sub-thrust structural high, as it does not have an orientation that would make it related to another Rocky Mountain

foreland-type uplift.

Approximately midway along the traverse, as the highway bends gradually southward, there is a roadcut through the rocks of the LaHood Formation, the only occurrence of the LaHood on the footwall side of the Cave–Jefferson Canyon fault system. Schmidt and others (2014) proposed that the contact is a very tightly folded part of the Cave fault (discussed at Stop 6) which was cut by the later movement on the Jefferson Canyon fault at this location (figs. 6, 9, 12, 13). This explanation makes the LaHood here allochthonous and originally part of the hanging wall of the Cave–Jefferson Canyon fault system. This explanation has a couple of difficulties: First, it makes the folded fault extremely, perhaps unrealistically, tight; second, the LaHood here is not highly sheared as might be expected in a highly folded thrust fault zone, although the fault could follow the stratigraphic contact between the LaHood and overlying Woolsey Formation. The alternative explanation is that the Cave fault simply bends into the E–W fault zone created by renewed movement on fault F and the yet unexplained structural high (anticline) underneath this fault was cored by LaHood formation.

After the LaHood roadcut both the LaHood and Woolsey Formations are thrusted over an overturned anticline in the Upper Paleozoic section (fault G, figs. 9, 12, 13). The Pennsylvanian Amsden and Quadrant formations are replete with minor folds that have hinges plunging north and parallel to the thrust indicating NW–SE shortening. The last rocks along the highway at the end of the traverse are gastropod-rich carbonates of the Cretaceous Kootenai Formation and black shales of the Colorado Formation. In the adjacent valley another thrust (fault H, figs. 9, 12) trends to the northeast and is cut by the Jefferson Canyon fault. At the head of the valley, along the intersection of the two faults, a large, intensely fractured and hydrothermally altered horse block of Cambrian Pilgrim Limestone through Mississippian Lodgepole Limestone is folded into the early Cave–Jefferson Canyon fault zone and cut by the later movement on the Jefferson Canyon fault (fig. 10, B–B´).

In the cliffs south of the highway across the Jefferson River from this position, the Jefferson Canyon fault dips very gently west and becomes a hanging wall flat (fig. 10, A–A´). This fault corresponds to the E–W-trending fault in the cliffs above the highway and must be the part of the Jefferson Canyon fault that was the last to move. The Jefferson Canyon at this location cuts through a flat portion of the Jefferson Canyon fault/thrust sheet, with the ramp portion of the sheet exposed at the beginning of the traverse. Older rocks, folded before the emplacement of the thrust sheet, are exposed in the lower parts of the canyon along the traverse. It is likely that this later Jefferson Canyon thrust, which is in the footwall of the Cave fault here, played a role in the folding of the Cave fault in "duplex fashion." Although Schmidt and others (2014) attributed folding of the Cave fault to lock up of movement of the Jefferson Canyon fault because of the resistance provided by large horse blocks in the fault zone, the actual initiation of folding was likely the later thrust movement described above. An interesting outcrop of Lodgepole Limestone (across the canyon) on the hanging wall of this thrust, on top of an overturned syncline in Pennsylvanian and Permian rocks (fig. 5, 9, 10, A–A´), contains a 10-m-scale refolded isoclinal syncline, indicating a very complex history of deformation. Here, as elsewhere along the thrust, shortening direction was demonstrably NW–SE.

Return to vehicles and proceed east on Montana 2. At 39.8 mi, Upper Paleozoic and Mesozoic rocks south of the Jefferson Canyon fault (and immediately south of the highway) are folded and faulted in a faulted anticline–syncline pair (Vuke and others, 2014). The fold-fault geometry strongly suggests a largely fault-propagation fold, as opposed to the detachment folds on the hanging wall of the Cave–Jefferson Canyon fault system. Turn left (north) at the intersection of Montana 2 with US 287 at mile 42 and proceed to Milligan Canyon (figs. 2, 14). Turn left onto the Milligan Canyon road at mile 47.2. Proceed north to Stop 8 (2.3 mi).

STOP 8 Mile 49.5

(45.878°N, 111.680°E)

The purpose of this stop is to examine some minor faults in the Lodgepole Limestone and to discuss other minor structures and broad folds on the hanging wall of the Jefferson Canyon fault near to where it bends northward to become the Lombard thrust (fig. 14). We will have a look the faults and slickenfibers (figs. 15a, 15b) first and then gather for a review of these and other relevant structures. The structure between the Cave anticline–Greer Gulch syncline fold pair and this location, a distance of about 8.5 km, is a simple homoclinal panel in LaHood and Phanerozoic rocks

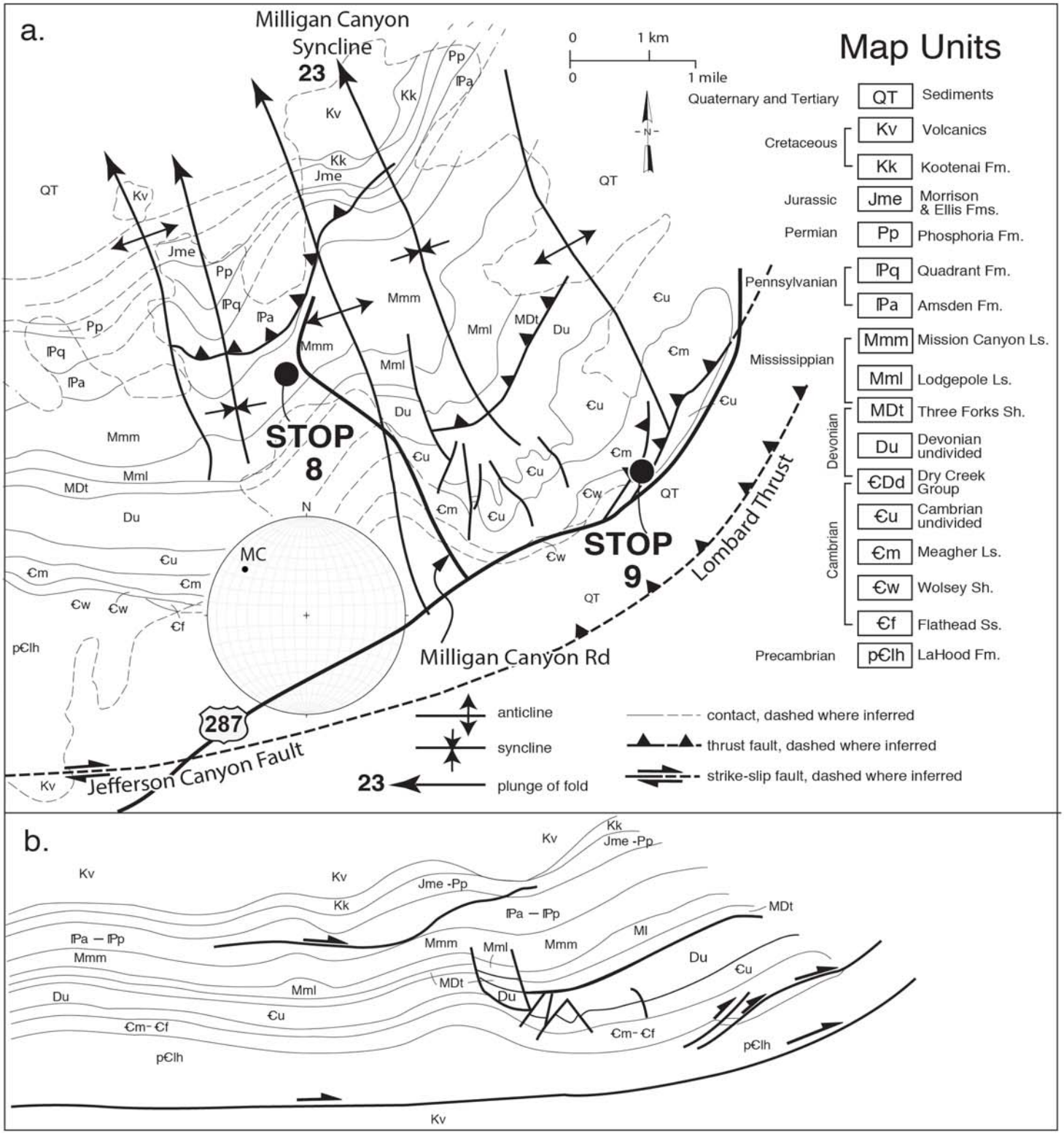

Figure 14. a, Geologic map of the homoclinal panel and folds in the Milligan Canyon area showing location of Stop 8 (where movement on minor faults was measured) and a stereoplot of the fold axis of Milligan Canyon syncline. B, Down-plunge section of the Milligan Canyon area.

Figure 15. a, Photograph of slickenfibers in Mississippian Lodgepole Limestone in Milligan Canyon area at Stop 8 (fig. 14). B, Photograph of a minor fault in Milligan Canyon area.

on the hanging wall of the Jefferson Canyon fault (fig. 2). Along this homoclinal panel a spaced cleavage fabric, both stylolitic and anastomosing, is ubiquitous in the Lodgepole Limestone and probably reflects the earliest internal (layer-parallel) shortening in the Lombard thrust sheet. This same cleavage is folded in the folds of the DMFC and Cave–Greer Gulch fold pair. We measured the cleavage at three stations along the homoclinal panel (locations 1, 2, and 3, fig. 2) spaced about a mile apart. The poles to cleavage are assumed to represent the shortening direction during the development of the cleavage. The easternmost location (#1) has a shortening direction that is slightly rotated (clockwise) with respect to the other two locations (fig. 16 Aa) because bedding was rotated slightly clockwise due to folding in the area. When restored for this folding mean poles to cleavage at all three locations are consistent with a shortening direction oriented 15°, 290° (fig. 16 Ad). Clustering of poles is not as tight when data is rotated to horizontal, suggesting that cleavage developed in the north-dipping panel, perhaps during translation of the Lombard sheet. The cleavage represents an early WNW–ESE shortening direction that is more E–W than that for the folding event for the Greer Gulch fold pair (290°compared to 318°, and even N–S during the last movement on the Greer Gulch thrust), providing further evidence that the Cave–Greer Gulch folding was a late event that occurred when movement on the Jefferson Canyon fault became locked and the Cave fault part of the system was folded.

The broad folds in the Milligan Canyon area are anomalous in that they plunge NNW (fig. 14a). The best defined of these folds, the Milligan Canyon syncline, is oriented 23°, 307°. A down-plunge section of the area (fig. 14b) shows the open shape of the folds and suggests that they are detachment folds above the Jefferson Canyon fault–Lombard thrust ramp. The simplest explanation for the anomalous NNW trend and gentle plunge is that this area is located at the transition from a lateral ramp to an oblique ramp and is the result of a backward rotation of the folds due to movement of the Lombard sheet on this oblique ramp.

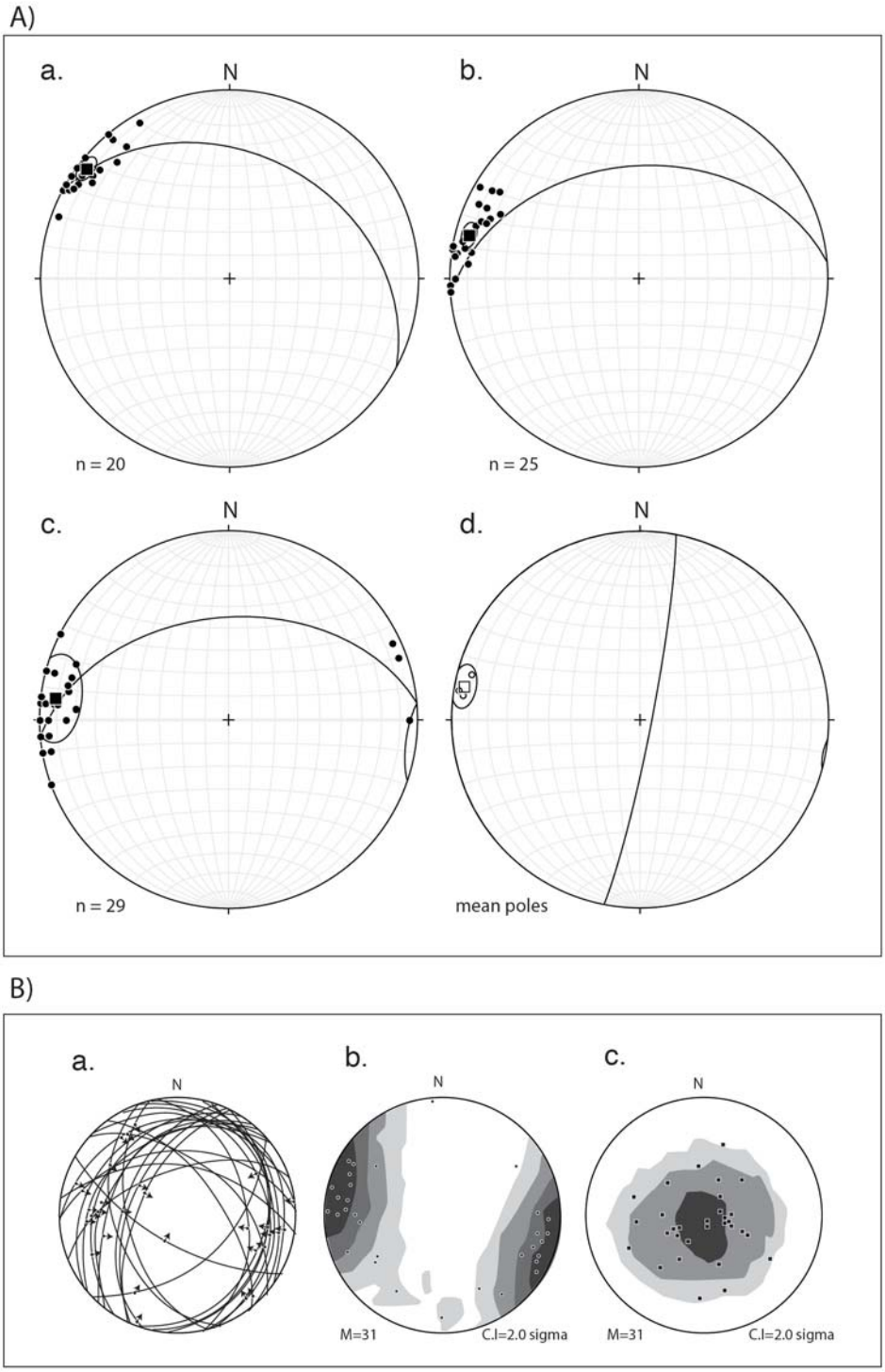

Figure 16. A, Stereoplots of poles to cleavage in the Mississippian Lodgepole Limestone in the homoclinal panel west of Milligan Canyon. In A–C, great circles are mean bedding orientation at each station; mean pole orientation is shown as a square. Stations are spaced 1 mi apart (see locations 1, 2, and 3, in fig. 2). Location 1, nearest to Milligan Canyon, has a different bedding orientation due to gentle folding of the panel. When rotated to an E–W strike, this and the other two stations have nearly identical cleavage orientations. A, Location 1, bedding orientation 300°, 34N; mean cleavage 38°, 85SE. B, Location 2, bedding orientation 85°, 40N; mean cleavage 15°, 82SE. C, Location 3, bedding orientation 85°, 45N; mean cleavage 7°, 82SE. D, Unfolded bedding position of mean cleavage orientations for locations 1, 2, and 3. Great circle is mean cleavage orientation (11°, 85SE). B, a) Stereonet of 31 minor fault orientations and slip directions in Milligan Canyon at Stop 8 on figs. 6, 10, and 14. b) Calculated shortening directions (Mean 3°, 285°). c) Calculated extension directions (Mean 85°, 155°).

Shortening direction can also be estimated from the numerous well-exposed minor bedding plane thrust faults with well-developed slickenside striae that occur as fibers on fault surfaces in the Lodgepole Limestone here (fig. 15). The kinematic analysis method of Marrett and Allmendinger (1990) was applied to 31 of these minor faults for which the direction and sense of slip could reasonably be determined. Data were analyzed using the program FAULTKIN, which calculates shortening (P) and extension (T) compatible with slip. The maximum concentration of P axes is at 3°, 285°, and for T axis it is 85°, 155° (fig. 16B). When the P and T axes were rotated by unfolding and unplunging the NW-plunging fold on which the minor faults are located, a small (10°) more northerly change was observed in the P-axis orientation and they were more scattered by the fold test, suggesting that the minor faults developed after folding. The shortening direction for these minor faults is within 4°of that indicated by cleavage in the Lodgepole. The cleavage is pre-folding and the faulting is probably post folding, suggesting that the shortening direction did not change significantly after folding at this location.

Return to US 287. Turn left (NE) onto 287.

STOP 9 Mile 54.1 (45.871°, 111.620°W) (figs. 2 and 14)

Pull off on highway turnout on right. At this stop we will examine the so-called “highway trust” of Robinson (1963), for its proximity to US 287. Robinson interpreted this to be a continuation of the Jefferson Canyon fault, with Cambrian Woolsey Formation on the hanging wall over LaHood Formation on the footwall

(younger on older). Graham and Suttner (1974) interpreted it as an unconformable contact with Woolsey above La Hood and an absence of Cambrian Flathead Sandstone due to a LaHood "island" in the Cambrian seaway. There is clearly faulting here, but it is relatively minor. The trace of the Jefferson Canyon fault is inferred to be below the Jefferson River approximately 1 km to the south of the highway where it must bend northward to become the Lombard thrust (figs. 2, 14).

CONCLUSIONS

(Discussion of these is best made at the end of Stop 8.)

Details of the internal shortening within the Lombard thrust sheet across the Devil's Fence anticline compared to the internal shortening along the southern lateral ramp boundary are discussed by Whisner and others (2014). They conclude: "The difference in the amount of internal shortening by disharmonic folding above the Lombard thrust near the Devils Fence anticline (4 km) and by extreme fold tightening of detachment folds and thrust faulting across fold hinges and limbs near the southernmost border of the salient (55%, 24 km) is similar to the difference in west–east thrust translation (20 km) between the center and southern edge of the sheet (fig. 1B, C). This suggests that a similar amount of shortening is experienced by the entire thrust sheet, but it is consumed primarily by thrust translation to the north and primarily by folding and less thrust translation to the south." We noted, in our discussion at Stop 1, that the dip separation on the Lombard thrust at the position of the Hossfeldt anticline is only about 1.5 km. This calls into question the estimates of a large amount of strike slip movement on the Cave–Jefferson Canyon fault system prior to and during internal deformation. Estimates of strike separation by Schmidt and Hendrix (1981), based on offset isopach lines of Jurassic and Cretaceous rocks on either side of the SWMTZ, vary between 21 and 32 km. The basin margin detachment (Cave–Jefferson Canyon fault system) is inferred to continue eastward past the Lombard thrust to the Bridger Range (Lageson, 1989) and perhaps beyond. The estimates of strike separation may represent the separation over the entire SWMTZ and not just the Lombard sheet.

We proposed/asked five questions to consider in the introduction to this field guide. Below we provide very brief answers to these questions based on what we can infer from the field evidence. We encourage alternate answers to these questions.

1. What is the nature of control of the Willow Creek fault on the Cave–Jefferson Canyon fault system? The buried Neoproterozoic Willow Creek normal fault zone had one or more down-dropped blocks that provided a depocenter for the LaHood Formation. The basal detachment of the Lombard thrust sheet and its southern lateral ramp exploited the north facing basement-LaHood contact, "picking off" pieces of the hanging wall block(s) and incorporating them as horse blocks in the Cave–Jefferson Canyon fault zone at the base of the lateral ramp.

2. What, if any, was the control of Rocky Mountain foreland structures on the geometry and kinematics of the Cave–Jefferson fault system? The only Rocky Mountain foreland structure to intersect the SWMTZ in this area was the NE-plunging London Hills anticline, which preceded the development of the Cave–Jefferson Canyon fault system. The northeast-dipping Upper Paleozoic and Mesozoic rocks of the anticline were cut by the Cave fault (figs. 7–10). Besides the preexisting dips to the southern limb of the Cave syncline, the effect of the preexisting structure appears to be relatively minor. This question deserves more scrutiny, however, considering that the out-of-sequence footwall thrust responsible for initiating folding of the Cave fault developed on the northeast flank of the London Hills anticline.

3. What is the principal fold-fault relationship of the major hanging wall folds? All the major folds we have studied involving the LaHood Formation within the hanging wall of the Cave–Jefferson Canyon fault system, the Lombard thrust, and thrust sheets to the east of the Lombard thrust appear to have had significant folding before faulting and are likely to be mostly detachment folds within the LaHood and younger rocks above Archean basement. The nature of the fold-fault relationships in the Phanerozoic section south of the Mayflower Mine–Cave–Jefferson Canyon system, where the LaHood is absent, is different and better fits a fault-propagation fold mechanism.

4. How do we explain the change in plunge of the major hanging wall folds from north to south and the change in trend of the folds from west to east at the southern boundary of the Lombard sheet? The change in plunge from north to south in the western part of this area was caused by the formation of the DFA culmination on the north, which produced south plunging folds within the Lombard thrust sheet, and by the lateral thrust ramp on the south, which pro-

duced north-plunging folds. The area between is a depression or sag in the sheet (Boulder depression) (figs. 2, 5). The change in trend of the folds on the hanging wall of the Cave fault, and the western part of the Jefferson Canyon fault, was produced by a change in the shortening direction. The initial shortening direction was W–E to WNW–ESE, producing folds that were mostly N- to NNE-trending. Locking of movement on the Jefferson Canyon segment of the fault and faulting from below caused the folding of the Cave fault segment by regional simple shear. This also caused the developing detachment fold axes to be progressively rotated clockwise (in map view). Shortening direction changed locally to NNW–SSE (and finally to N–S). On the far southeastern part of the Lombard sheet folds were produced on the hanging wall of the oblique ramp transition from the Jefferson Canyon fault to the Lombard thrust and were rotated backwards and to the NE by movement up the ramp. Other changes in fold trends (depicted in fig. 17) can be attributed to backwards rotation of some of the folds in the DMFC due to later thrusting, changing their initial north trend to a more northwest trend.

5. What is the basic structural relationship between the Cave and Jefferson Canyon faults? The Cave fault and the Jefferson Canyon fault are different parts of the same detachment modified by folding and by later thrust faulting (fig. 13). The Cave fault (western segment of the detachment) was folded by thrusting from below and/or lock up because of the "resistance" to moving large horse blocks in the fault zone. The Jefferson Canyon fault was later modified by thrusting along the same fault that may have initiated folding of the cave fault segment.

6. Which of the explanations of thrusting below the Lombard sheet at the DFA is more compatible with the observations along the southern boundary of the sheet? One explanation is that the thrusts responsible for the DFA culmination involve Paleozoic and Mesozoic rocks (fig. 1C). The other is that the thrusts only involve Mesoproterozoic Belt rocks. I do not think the field observations alone can resolve this question. Although it appears that the Lombard thrust sheet is probably not a "far-traveled" feature, the question of the age of the rocks involved in the sub-Lombard sheet thrusts responsible for the DFA culmination is still an open question. It is a relatively important question, not just for potential oil exploration, but for estimates of the amount of shortening that occurred in the Lombard system below the Lombard sheet. It is interesting that Paleozoic rocks,

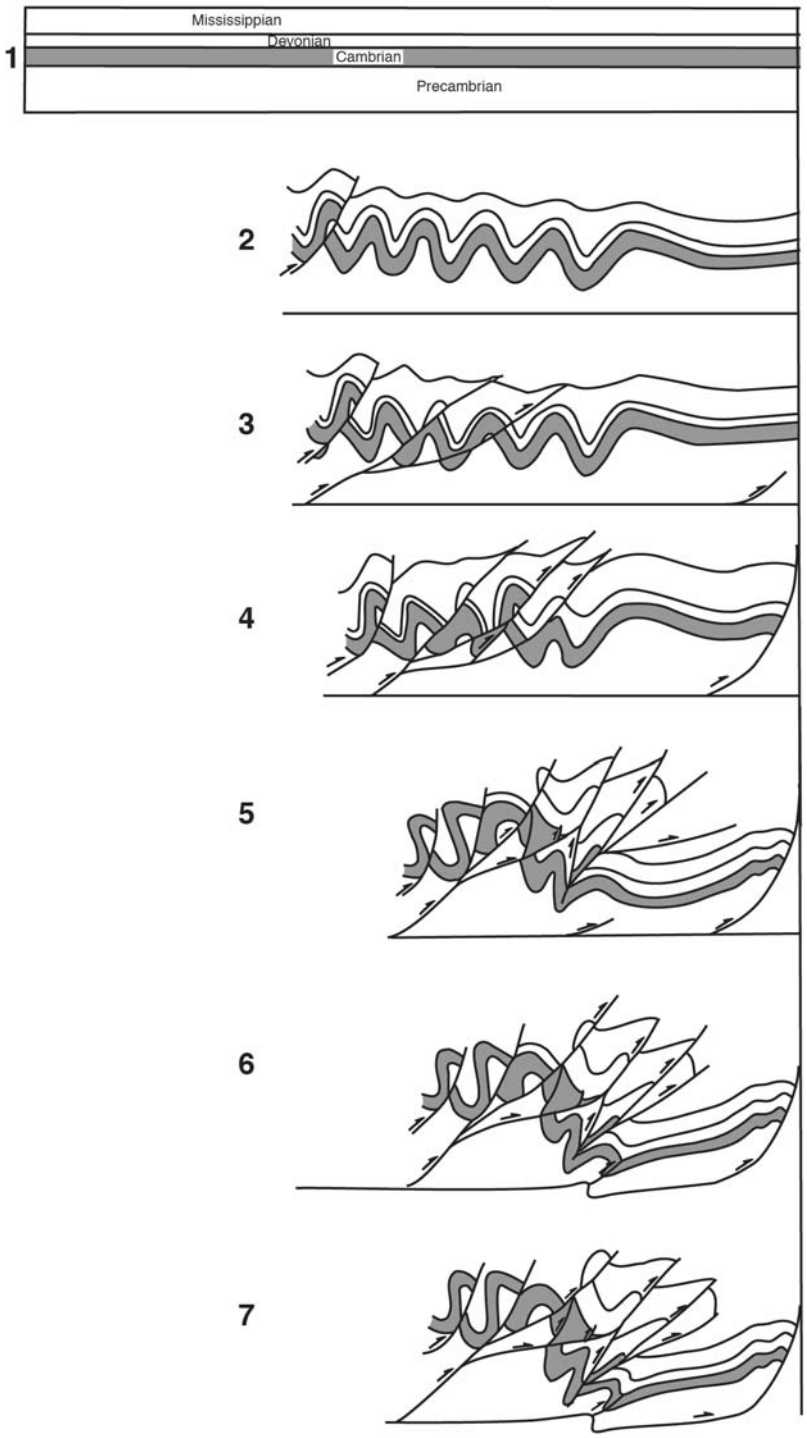

Figure 17. Schematic W–E sequential cross-section evolution of the folds and faults in the Doherty Mountain fold complex and Lewis and Clark Cavern and Milligan Canyon areas. Lowermost thrust is Cave–Jefferson Canyon–Lombard fault.

and possibly LaHood rocks below them, exist as a sub-thrust high below the Jefferson Canyon fault in Jefferson Canyon, although an actual connection between these rocks and those below the DFA is impossible to determine.

ACKNOWLEDGMENTS

Thanks and appreciation to the following people and groups who have been very helpful in both ideas and encouragement supporting our continuing work on the complicated geology of the area described in this field guide: Susan Vuke, Rich Aram, Nick Woodward, Ned Sterne, the people who work at the Lewis and Clark Caverns State Park, and the Tobacco Root Geological Society. Thanks also to Thomas Howe, Department of Geosciences, Western Michigan University for help with the field trip diagrams. Thanks to Sandy Underwood for very careful editing of the manuscript.

REFERENCES

Alexander, R. G., 1955, Geology of the Whitehall area, Montana: Yellowstone-Bighorn Research Project Contribution 195, 111 p.

Alonso, T.L., and Teixell, A., 1992, Forelimb deformation in some natural examples of fault-propagation folds: in McClay, K. R., ed., Thrust Tectonics: Chapman and Hall, London, p. 175-180.

Aram, R. B., 1981, Geologic history of Lewis and Clark Caverns, Montana: in Tucker, T.E., ed., Field conference and symposium guidebook to southwest Montana: Montana Geological Society, p. 285-300.

Ballard, D.W., Burton, B.R., Lageson, D.R., and Warne, J.R., 1993, Drilling experiences at Devil's Fence anticline, Jefferson County, Montana: Baseline data for future activities in a promising overthrust province: Montana Geological Society 1993 Field Conference Publication, p. 159-168.

Burton, B.R., Lageson, D.R., Schmidt, C.J., Ballard, D.W., and Warne, J.R., 1996, Large magnitude of the Lombard thrust system of the Helena salient, Montana fold and thrust belt: implications for emplacement of the Boulder batholith and reconstruction of the Belt basin: in Berg, R., ed., Proceedings of the Belt Symposium III: Montana Bureau of Mines special publication, 229-243.

Graham, S.A., and Suttner, L.J., 1974, Occurrence of Cambrian Islands in Southwest MT: Mountain Geologists, vol. 11, no. 2, p. 71-84.

Hawley, D., and Schmidt, C.J., 1976, Road log 4 Belt rocks and structural geology in the Northern Tobacco Root Mountains: Montana Bureau of Mines and Geology Special Publication 73, p. 151-175.

Harlan, S.S., Geisman, J.W., Whisner, S.C., and Schmidt, C.J., 2008, Paleomagnetism and geochronology of sills in the Doherty Mountain area, southwestern Montana: Implications for timing of fold-and-thrust belt deformation and vertical-access rotations along the southern margin of the Helena salient: Geological Society of America Bulletin, v. 120, p. 1091-1104.

Hendrix, T.E, and Stellavato, N., 1976, Pervasive deformation of the Meagher Oolitic limestone, North Bolder Valley, Montana: in Montana Bureau of Mines and Geology Special Publication 73, p. 131-139.

Lageson, D.R., 1989, Reactivation of a Proterozoic continental margin, Bridger Range, southwestern Montana: in French, C.E., and Grab, R. F., eds, Geologic resources of Montana: Montana Geological Society Field Conference Guidebook Montana. Montana Centennial Edition, v.1, p. 279-298.

Marrett, R.A., and Allmendinger, R.W., 1990, Kinematic analysis of fault-slip data: Journal of Structural Geology, v. 12, p. 973-986.

McMannis, W.J., 1963, LaHood Formation: A coarse facies of the Belt Series in southwestern Montana: Geological Society of America Bulletin, v. 74, p. 407-436.

McNaught, M.A., and Mitra, G., 1993, A kinematic model for the origin of footwall syncline: Journal of Structural Geology, v. 15, p. 805-808.

Mitchell, M.M., and Woodward, N. B., 1988, Kink detachment fold in southwest Montana fold and thrust belt: Geology, v. 16, p. 162-165.

Mitchell, M.M., Woodward, N.B., 1988, Comment and reply "kink detachment fold in southwest Montana fold and thrust belt", reply: Geology, v. 16, p. 1054.

Ramsay, J.G., 1967, Folding and Fracturing of Rocks: McGraw-Hill, New York, 568 p.

Robinson, G.D., 1963, Geology of the Three Forks quadrangle, Montana: U.S. Geological Survey

Professional Paper 370, 143p.

Schmidt, C.J., 1975, An analysis of folding and faulting in the northern Tobacco Root Mountains, southwestern Montana: Bloomington Indiana, Indiana University, Ph.D. dissertation, 450 p.

Schmidt, C.J., 1988, Comment and reply "kink detachment fold in southwest Montana fold and thrust belt", comment: Geology, v. 16, p. 1052-1054.

Schmidt, C.J., and Hendrix, T.E., 1981, Tectonic controls for thrust belt and Rocky Mountain foreland structures in the northern Tobacco Root Mountains, Jefferson Canyon area, southwestern Montana: in Tucker, T.E., ed., Montana Geological Society Field Conference Guidebook to Southwestern Montana, p. 176-180.

Schmidt, C.J., Aram, R., and Hawley, D., 1987, The Jefferson River Canyon area, southwestern Montana: in Geological Society of America Centennial Field Guide-Rocky Mountain Section, p. 63-68.

Schmidt, C.J., O'Neill, J.M., and Brandon, W.C., 1988, Influence of Rocky Mountain foreland uplifts on the development of the frontal fold and thrust belt, southwestern Montana: in Schmidt, C.J., and Perry, W.J., eds., Interaction of the Rocky Mountain Foreland and Cordilleran Thrust Belt: Geological Society of America Memoir 171, p. 171-202.

Schmidt, C.J., Smedes, H.W., and O'Neill, J.M., 1990, Syncompressional emplacement of the Boulder and Tobacco Root batholiths (Montana-USA) by pull-apart along old fault zones: Geological Journal, v. 25, p. 305-318.

Schmidt, C.J., Whisner, S.C., and Whisner, J.B., 2014, Folding of a detachment and fault-modified detachment folding along a lateral ramp, southwestern Montana, USA: Journal of Structural Geology, v.69, p. 334-350.

Verrall, P., 1955, Geology of the Horseshoe Hills area, Montana: Princeton, New Jersey, Princeton University Ph.D. dissertation, 261p.

Vuke, S.M., Lonn, J.D., Berg, R.B., and Schmidt, C.J., 2014, Geologic map of the Bozeman 30' x 60' quadrangle, southwestern Montana: Montana Bureau of Mines and Geology Open File Report 648, 44 p., 1 sheet, scale 1: 100,000.

Whisner, S.C., Schmidt, C.J., and Whisner, J.B., 2014, Structural analysis of the Lombard thrust sheet and adjacent areas in the Helena salient, southwestern Montana, USA: Journal of Structural Geology, v. 69, p. 351-376.

GEOMETRY AND KINEMATICS OF THE PARADISE SHEAR ZONE, PART OF A MAJOR SUTURE ZONE WITHIN THE WYOMING PROVINCE OF SOUTHWEST MONTANA

Thomas J. Kalakay,[1] Jeffrey R. Webber,[2] and David R. Lageson[3]

[1]Rocky Mountain College, 1511 Poly, Billings, Montana 59102, kalakayt@rocky.edu
[2]Stockton University, 101 Vera King Farris Galloway, New Jersey 08205, jeffrey.webber@stockton.edu
[3]Montana State University, P.O. Box 173480, Bozeman, Montana 59717, lageson@montana.edu

INTRODUCTION

The objective of this field trip is to examine the geometry, kinematics, and timing of a major suture zone within the Archean age Wyoming Province of southwest Montana. The structural and geochronologic data presented here provides vital information about early growth of the North American continent and helps test hypotheses for growth of continents during the late Archean transition from plume/vertical tectonics to a horizontal tectonic regime.

The timing and mechanisms for earliest forms of continental growth are not well understood (Hawkesworth and others, 2016). Mantle differentiation that eventually led to the incipient formation of continental crust, likely began in the Hadean eon (Boyet and Carlson, 2005; Kemp and others, 2010). However, it is widely accepted that most of Earth's continental crust formed during the Archean (Cavosie and others, 2005; Hawkesworth and others, 2016 and references therein; Reimink and others, 2016). Despite this consensus, the timing and mechanisms for early continental growth remain poorly understood (Hawkesworth and others, 2016). Exactly when the early continents began to grow and whether they grew through vertical plume processes or by lateral plate tectonics are topics of active debate. Finding a solution is hindered by the fact that these ancient rocks are mostly buried under younger sediments and thus not exposed at Earth's surface. Exposures do exist, within the cores of continents, where younger tectonic events have brought them to the surface in unique blocks. These exposures provide key information about the early growth and modification of continental crust.

One such exposed block is the northern Beartooth Range of Montana and Wyoming (fig. 1). Rocks exposed in the Beartooth uplift make up a portion of the Wyoming Province, one of the oldest known fragments of continental crust in North America (Frost 1993; Mueller and others, 1996). Rocks in the eastern and central Beartooth Range are dominated by Late Archean granitoids known as the Beartooth Magmatic Terrane (BMT) (Mueller and others, 2010). To the west, lies the Montana Metasedimentary Terrane (MMT), comprised of mostly of high-grade metasediments and varying amounts of metaigneous rocks. The chronologically and compositionally distinct magmatic terrane and the high-grade metasedimentary terrane are separated by a major discontinuity exposed in the western Beartooth Mountains (Mogk and others, 1988; 1992). Mogk and others (1988) hypothesized that juxtaposition of these units occurred via lateral accretion between 2.74 and 2.56 Ga. The primary objective of this field trip is to visit exceptional exposures and examine the important period of continental growth that occurred in the Late Archean, when plume-type crustal growth was declining and plate tectonic growth processes increased. Field trip leaders will emphasize kinematic data that illustrates lateral motion (i.e., thrusting) was the dominant process in joining the BMT and MMT terranes. There will also be discussion of thermobarometric data and isotopic dating that helps constrain field evidence regarding the precise timing of suturing between the two units.

FIELD EXCURSION OUTLINE

This all-day field trip begins in Bozeman. The first stop is at Pine Creek (fig. 2) where field trip leaders will discuss the Pine Creek fold complex and other elements of the Pine Creek suture (fig. 1). Stop 2, at Mill Creek, is an overview to discuss the geology of the North Snowy Block. If time permits, optional stops will be made to observe Mount Cowen granite and other rocks in roadside outcrops along Mill Creek. Stop 3 is near Chico Hot Springs, where the shear zone crosses the mouth of Emigrant Gulch. Stop 4 is along Sixmile Creek where the drainage exposes an important transect through the Snowy shear zone. Several stops and short hikes will be made along the Sixmile Creek road. From Sixmile Creek, the excur-

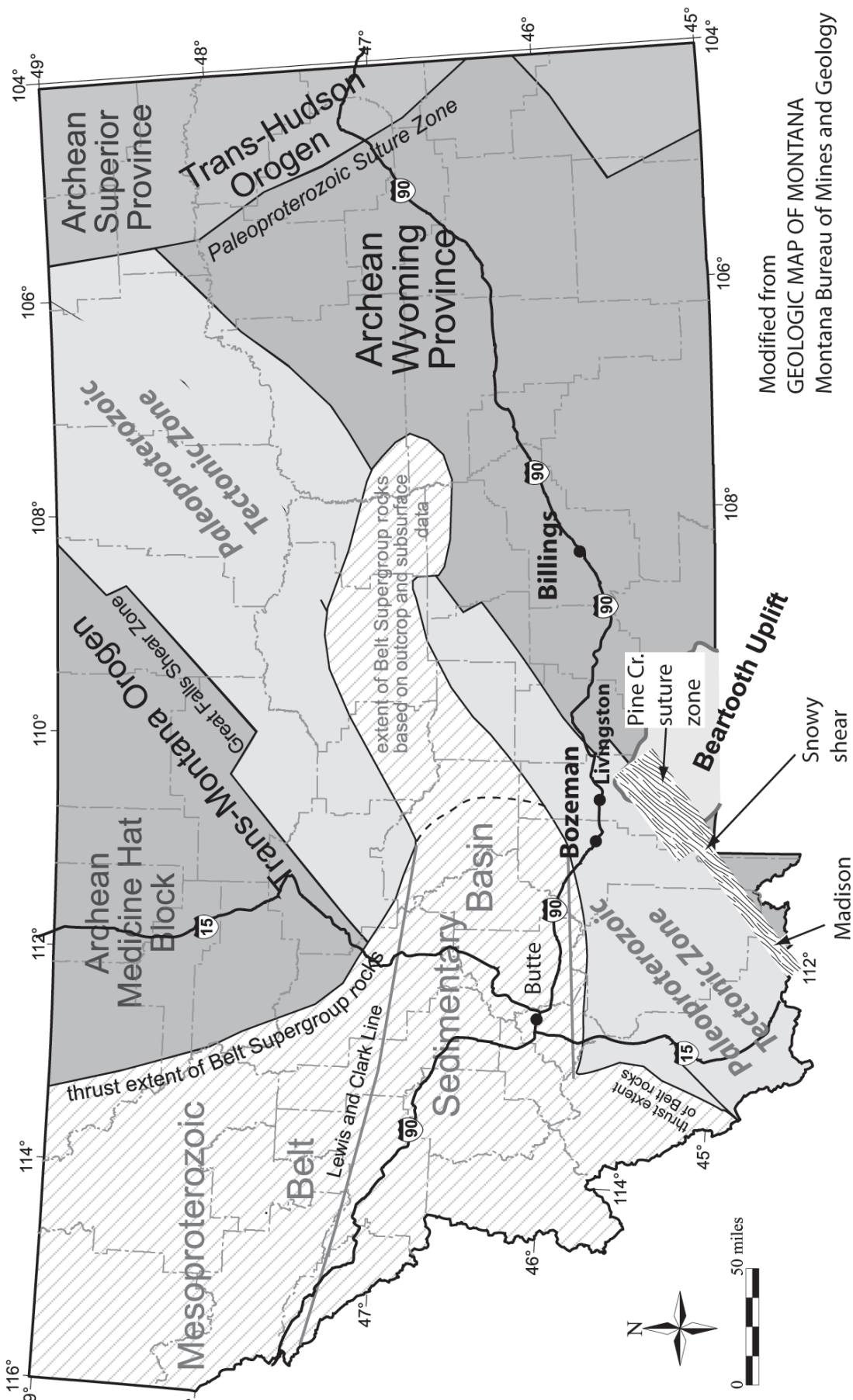

Figure 1. Generalized tectonic map of Montana. The field trip route covers the area at the NW end of the Beartooth uplift, where the Pine Creek suture and the Snowy shear zone are exposed. These structures connect along strike with the Madison mylonite zone.

Figure 2. Generalized geologic map of the Paradise Valley. Field trip stops are shown.

sion moves to the area near Crystal Cross Mountain (Stop 5), where rocks in the hanging wall of the shear zone are well exposed.

ROAD LOG

From Bozeman's East Main onramp, merge onto I-90 East. Continue on I-90 to Livingston (~23.0 miles). At Livingston, take exit 333 for US-89 South toward Yellowstone National Park. Turn left onto US-89 South. Continue south for 3.2 miles and turn left onto East River Road (State Hwy 540). Continue on East River Road for 7.7 miles, through the town of Pine Creek (good lunch stop) and turn left onto Luccock Park Road. Continue on Luccock Park Road to Pine Creek Campground (~2.7 miles).

STOP 1

At this stop, we will examine rocks and structures of the Pine Creek sequence and discuss the extent of the Paradise shear zone. In our view, the deformed belt exposed from Pine Creek to the West Boulder drainage are part of a through-going shear zone that includes the Pine Creek suture (North Snowy Block), the Snowy shear zone (South Snowy Block), the Madison mylonite zone (Southern Madison Range) and sheared rocks in the Centennial Range near the Montana-Idaho border. These structural domains are distinctly on strike with one another and also share geometric, kinematic, and timing characteristics that allow for our interpretation. At this scale, this tectonic belt forms the boundary between two fundamentally different terranes in the northern Wyoming Province, a Late Archean plutonic terrane to the east and an Archean metasedimentary terrane to the west. Relationships along the western edge of the Beartooth Mountain Range suggest that this boundary was produced during a Late Archean orogeny that shares structural and kinematic characteristics with collisional zones found in the Alps and the Himalaya.

Authors' Note

In the authors' view, the use of "North Snowy Block" and "South Snowy Block" are confusing and not useful with respect to Precambrian geology and tectonics. The North and South Snowy Blocks are defined by the Eocene age Mill Creek Fault and Elbow Creek Fault that collectively form an East-West striking structural zone that separates the North and South Snowy Blocks. Field evidence shows less than 2,000 ft (~600 m) of throw across the fault zone (Kalakay, unpublished mapping), which results in an insignificant discordance within the Precambrian rocks and structures between the two "blocks".

Pine Creek exposes a transect through rocks and structures of the Pine Creek fold complex and suture zone (Reid and others, 1975; Mogk and others, 1988). The Pine Creek complex has been described as consisting of seven units that are distinguished by abrupt discontinuities in lithology, metamorphic grade, structural style, and in some instances, isotopic age (Mogk and others, 1988). From east to west the units are the Mount Cowen augen gneiss, a paragneiss unit, augen gneiss sill, Davis Creek schist, a trondhjemite/amphibolite unit, and the so-called Pine Creek nappe complex. With the exception of the Mount Cowen augen gneiss, rocks exposed in Pine Creek are mostly comprised of metasediments. The fold complex, best exposed near Pine Creek Lake, is a conspicuous sequence consisting of fuchsite bearing quartzites, calc-silicates, and mafic gneisses.

All units within the Pine Creek sequence are intensely deformed and most show mylonitic fabrics and intense transposition within units. Mylonitic foliations are folded by a series of isoclinal and more open style folds. The Pine Creek fold is well exposed on the north wall of the canyon, below Pine Creek Lake. This km-scale fold has been described as a nappe by Reid and others (1975). It is not a true Alpine-style nappe in that the fold is not recumbent. It is instead a series of refolded isoclinal folds with moderate to steeply plunging hinge lines. Similar style folds are observed in some of the classic collision zones such as the Alps and the Himalaya. The Pine Creek fold complex forms the western part of a broad zone of deformation that extends in width from the mountain front near Pine Creek to the eastern side of the West Boulder River (a distance of over 15 km). Rocks and deformation within this belt characterize the nature of the suture zone that juxtaposed the Beartooth Magmatic Terrane and the Montana Metasedimentary Terrane.

Return west on Luccock Park Road toward East River Road (State Hwy 540). Turn left (south) onto East River Road and continue for 7.0 miles. Turn left onto Mill Creek Rd. (Option: Continue ~7 miles to Snowbank Campground to view Mt. Cowen granite along Mill Creek Road).

STOP 2

This stop provides a unique, but distant view of the geology that forms the core of the North Snowy Block.

The highest and most spectacular peak in the area is Mount Cowen (11,207 ft; 3,416 m), in the west-central part of the North Snowy Block. The Mount Cowen massif is comprised of the Mount Cowen granite gneiss and other orthogneiss units that make up the core of the North Snowy Block. The Mount Cowen gneiss unit shows a prominent steep, west dipping mylonitic foliation that strikes northeast. Kinematic indicators within the mylonites show a consistent top-to-the-southeast, reverse sense of shear (fig. 3). The gneiss is cross-cut by three distinct generations of dikes and small intrusive bodies. The oldest generation is composed of pink granite. The second generation is a distinct suite of leucogranite dikes and small pods, that make up the majority of the cross-cutting intrusions (fig. 4, fig. 5). These leucogranite bodies are interpreted as crustal melts that formed in the late stages of collision, like those observed in the Himalayan orogen (Searle and others, 2006). The youngest generation is a suite of diabase dikes. All of the cross-cutting intrusive bodies exhibit mylonitic fabrics along their contacts, yet cross-cut the mylonitic fabrics in the Mount Cowen gneiss. This indicates that timing of their emplacement came relatively late in the orogenic cycle.

STOP 2b
(optional)

Roadside outcrop of Mount Cowen gneiss along the main fork of Mill Creek near Snowbank Campground.

STOP 2c
(optional)

Roadside outcrop of deformed mafic gneiss along the west fork of Mill Creek.

Return west on Mill Creek Road. Take a slight left onto Pray Road. Continue on Pray Road and then turn left onto East River Road (State Hwy 540). Continue on East River Road for 1.7 miles and then turn left onto Chico Road. Park somewhere between Chico Hot Springs and the mouth of Emigrant Gulch.

STOP 3

A brief stop here to look at rocks and fabrics of the Snowy shear zone, which lies at the northern end of the South Snowy Block. The Snowy shear zone is contiguous with the shear zone rocks discussed and observed at earlier stops in the North Snowy Block. Rocks of interest are exposed near the mouth of Emigrant Gulch.

From Chico, head north on Chico Road and return to East River Road (~1.6 miles). Turn left (south) onto East River Road. After 4.1 miles, turn left onto Sixmile Creek Road. Continue straight on Sixmile Creek

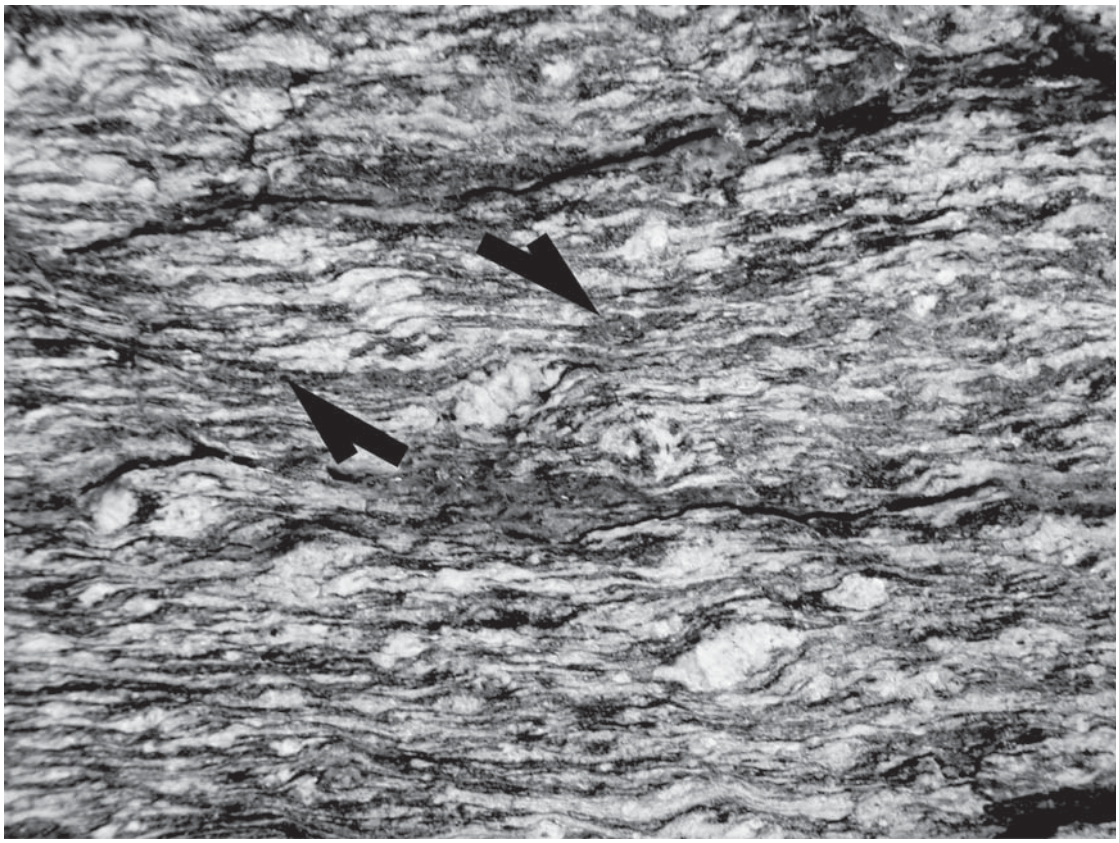

Figure 3. Mylonitic fabrics within the Mount Cowen gneiss, a deformed Archean age granite forming the core of the North Snowy Block. Kinematic indicators (S-C foliations, rotated K-Spar porphyroclasts) show a consistent reverse sense of shear.

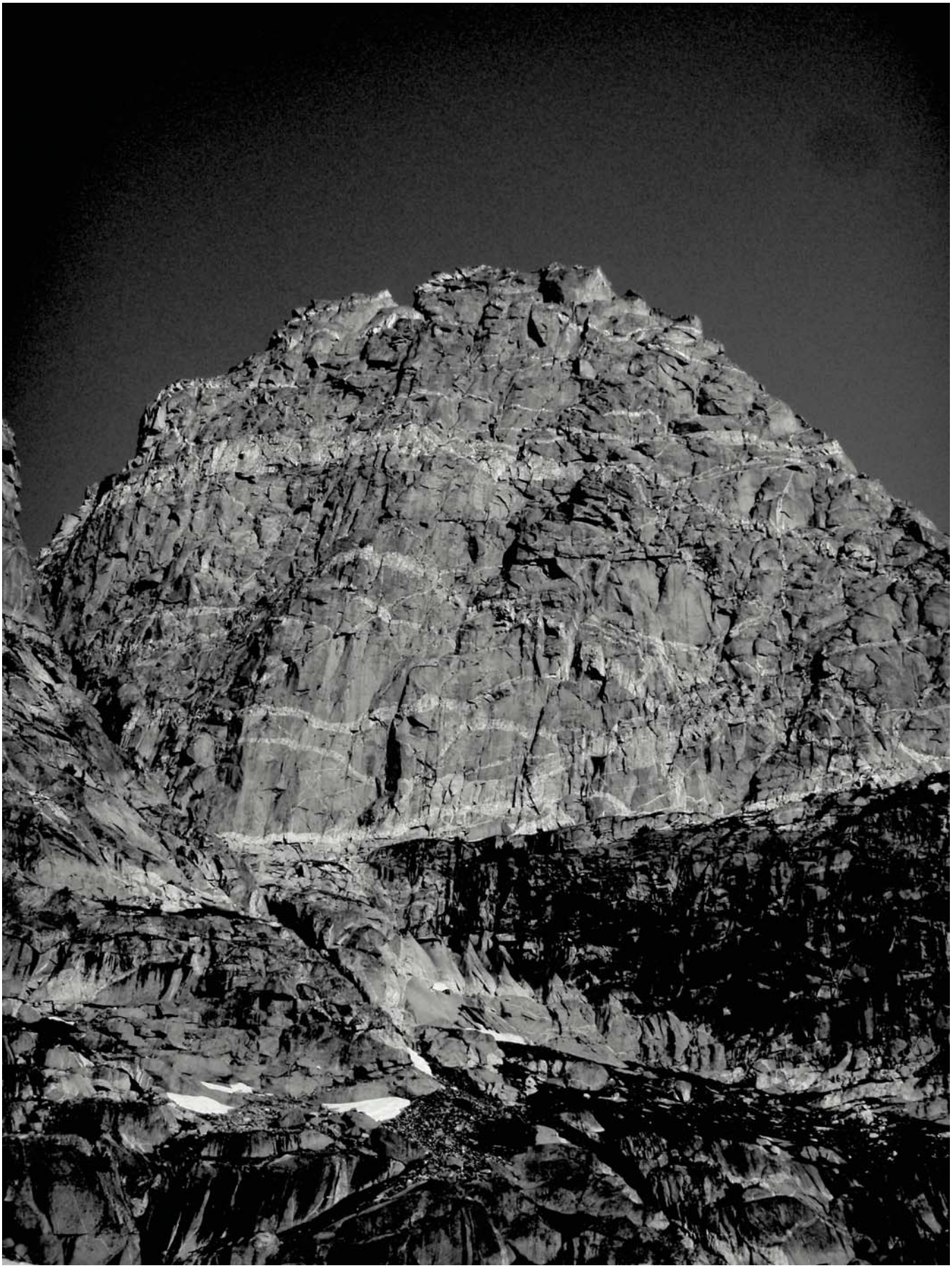

Figure 4. Leucogranite pods and dikes cross-cutting Mount Cowen gneiss on the east side of Mount Cowen.

Figure 5. Pink granite dike cross-cutting protomylonitic Mount Cowen gneiss in the cirque above Elbow Lake.

Road for ~3.5 miles. The road curves to the right (west) and becomes Daily Lake Road. Continue for another ~0.5 miles and turn left onto Sixmile Creek Road. The next several stops are along Sixmile Creek Road (mileage: ~9.5 miles from Chico stop).

STOP 4

The geology of Sixmile Creek is complicated, but crucial to understand because it epitomizes the polyphase nature of the Paradise shear zone. In this paper, we do not separate shear zone structures in the so-called North Snowy Block from those in the so-called South Snowy Block. We lump them collectively into the Paradise shear zone. In this transect, we will observe evidence for contractional, transpressional, and extensional kinematics all within what has been called the Snowy shear zone of the South Snowy Block. Fortunately, each kinematic zone is separated into its own discrete structural domain.

The Snowy shear zone cuts across the north edge of the South Snowy Block of the Beartooth Mountains (Erslev, 1992). It lies along strike with the Madison mylonite zone and other ductile shear zones in southwest Montana (fig. 1). According to Erslev (1992) and Harms and others (2004), the Snowy shear zone may have been active during the Big Sky orogeny. Erslev (1992) argued that the Snowy shear zone is a ductile normal fault based on the offset in metamorphic grade observed across the fault. If these timing and kinematic interpretations are correct, the Snowy shear zone could possibly represent one of the extensional structures during late-stage collapse of the Big Sky orogen (Harms and others, 2004).

We disagree with that interpretation and contend that normal sense of displacement is only one component of a complex, polyphase kinematic history for the Snowy shear zone. We go a step further and suggest that normal faulting recorded in shear zone fabrics is mostly related to much younger, Eocene extension.

At this stop, we will conduct an east to west traverse through the Snowy shear zone. We will begin in deformed granitoids that are most likely a southern continuation of the Mount Cowen gneiss. These rocks also contain protomylonitic and mylonitc fabrics that are very similar to those observed in the North Snowy Block. Like the Mount Cowen mylonites, kinematic indicators within this structural domain show top-to-the-southeast reverse sense of shear.

To the west of the mylonitic orthogneisses, there is a paragneiss sequence primarily composed of pelitic rocks, semi-pelitic rocks with relatively minor amounts of mafic gneiss and quartzite. The pelitic rocks contain conspicuous clots that appear to be pseudomorphs of staurolite. The clots now contain muscovite and quartz, but have the distinct shape of staurolite. The original host rock for these textures will be observed at Stop 5. Quartzites and mafic gneisses within this sequence are mylonitic with subhorizontal lineations. The pelitic rocks also contain subhorizontal lineations. Folding is prominent within the pelitic and semi-pelitic units. Fold hinges plunge steeply from 80 to 90 degrees. The subhorizontal lineations and steeply plunging fold hinges appear to overprint the reverse-sense fabrics in the orthogneiss unit. We interpret these as fabrics that record a period within the Snowy shear zone when collisional tectonics continued to progress into a transpressional tectonic regime. Similar progressions from compressional tectonics to transpressional tectonics are observed in the Alpine orogeny (Schmid and Kissling, 2000).

West of the paragneiss sequence, there is a zone comprised of metapelitic rocks, granitoids, and mafic gneisses. This sequence is mylonitic and intensely deformed. Lineations are down-dip and shear sense shows a normal sense of displacement. This is most likely the zone in which Erslev (1992) collected most of his structural data. The normal sense of shear might be related to late-stage orogenic collapse, as proposed by Harms and others (2004). However, there is no real field evidence or geochronologic data to support that interpretation. As we will observe at Stop 5, there is substantial evidence that normal-sense fabrics are most likely related to Eocene, or later, extension along the range-front fault system.

Retrace the route back to East River Road (~8.1 miles; Sixmile Creek Rd toward Daily Lake, right onto Daily Lake Rd, Continue on Sixmile Creek Rd to E. River Rd). Turn left (south) onto East River Road (State Hwy 540). Continue for 8.1 miles and then turn left (south) onto US-89. Continue for 3.1 miles and then take a right onto Tom Miner Creek Road. Cross the Yellowstone River and then turn right onto Old Yellowstone Trail. After 0.3 miles, turn left onto Rock Creek Road. The road travels mostly through private property and parking for the next stop is tricky to find. Stay with the group.

STOP 5

At this stop, we will take a short (40 minute) hike to Crystal Cross Mountain.

Exposures within the hanging wall of the Snowy shear zone near Crystal Cross Mountain were used to constrain the conditions of peak metamorphism by the application of thermodynamic modeling and geothermobarometric calculations. Bulk major oxide weight percentages were acquired from XRF analyses conducted by Acme Analytical Laboratories Ltd. and used in thermodynamic modeling. Selected stable phase assemblage diagrams were produced from the results of modeling using the program Theriak-Domino (de Capitani and Petrakakis, 2010) running the tcdb55c2d database. All mineral analyses and wave-dispersive spectroscopic (WDS) X-ray mapping was acquired with a Cameca SX-50 electron microprobe at the University of Massachusetts, Amherst. Quantitative analyses were applied to plagioclase, garnet, and biotite. WDS X-ray mapping of individual plagioclase and garnet grains were completed prior to mineral analyses to aid in the selection of transect locations for quantitative analyses. Multiple biotite analyses were applied to isolated grains throughout the matrix.

Thermodynamic modeling predicts a stable field assemblage dominated by garnet + staurolite + biotite + plagioclase + quartz, which occupies a region in pressure-temperature space from roughly 600°C to 690°C and approximately 475 MPa to 975 MPa. This predicted stable assemblage closely matches the non-retrogressed mineral assemblage observed in thin section. Isopleth contouring of almandine and grossular concentrations in garnet matches the observed composition from electron microprobe analyses at a temperature and pressure just outside of the predicted stable mineral assemblage (612°C and 841 MPa).

Quantitative electron microprobe mineral analyses were used by the program THERMOCALC (Holland and Powell, 2003) to determine the average conditions of peak metamorphism at 830 ± 220 MPa and 631°C ± 91°C. Despite the large errors associated with the THERMOCALC results, the average pressure-temperature data plot directly within the predicted stable mineral assemblage field. Furthermore, these results differ from the garnet composition by less than 20°C and 10 MPa.

Inclusions of garnet within staurolite indicate that garnet growth either predates staurolite or the two phases grew synchronously. However, no inclusions of staurolite are observed in garnet suggesting that initial garnet growth likely predated the development of staurolite. Given the results of thermodynamic modeling, a clockwise Pressure-Temperature path best supports the hypothesis of initial garnet growth followed by staurolite growth as shown in Figure 6.

Previous constraints on the conditions of peak metamorphism for the Crystal Cross Mountain area were estimated at approximately 300 MPa and 553°C based on the reported presence of andalusite (Erslev, 1992). However, these results greatly underestimate the results of our geothermobarometric and thermodynamic modeling and likely represent some component of retrograde metamorphism. Retrogression of the peak metamorphic assemblage is observed along with the development of an overprinting foliation towards the core of the Snowy shear zone, which is characterized by the greenschist facies replacement of staurolite by pseudomorphs of fine-grained mica and breakdown of garnet into mats of chlorite.

Retrace route back to US-89.

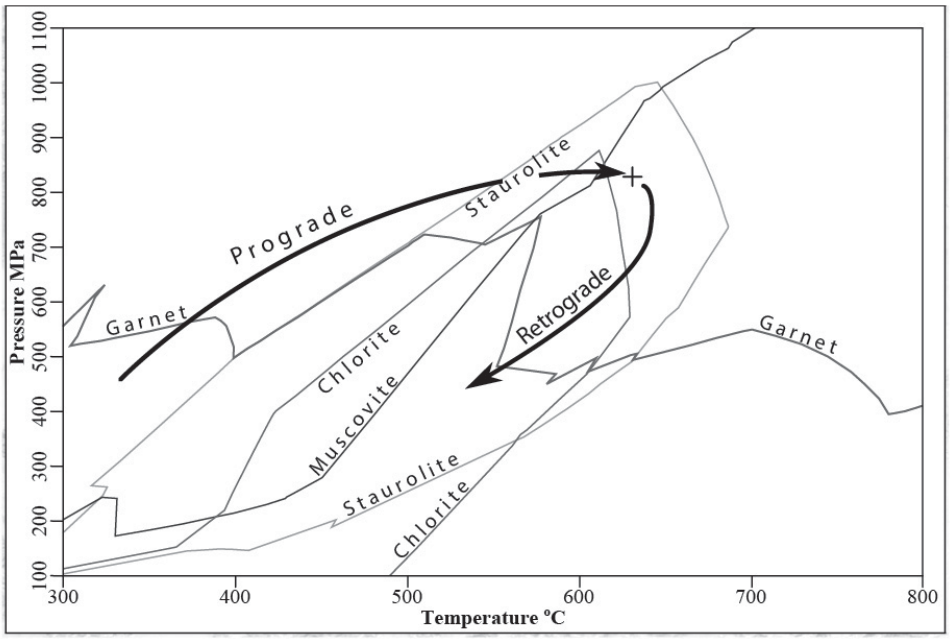

Figure 6. Selected stable assemblage diagram and inferred Pressure-Temperature path for garnet–staurolite–biotite schist of Crystal Cross Mountain.

REFERENCES

Boyet M. and Carlson R. W., 2005, 142Nd evidence for early (>4.53 Ga) global differentiation of the silicate Earth: Science v. 309 p. 576–581.

Cavosie A. J., Valley J. W., and Wilde S. A., 2005, Magmatic δ18O in 4400–3900 Ma detrital zircons; a record of the alteration and recycling of crust in the early Archean: Earth and Planetary Science Letters v. 235 p. 663–681.

de Capitani, C. and Petrakakis, K., 2010, The computation of equilibrium assemblage diagrams with Theriak/Domino software. American Mineralogist, 95(7), p.1006–1016.

Erslev, E.A., 1992, Precambrian geology and ductile normal faulting in the southwest corner of the Beartooth Uplift, Montana, in Bartholomew, M.J., and others., eds., Basement tectonics 8: Characterization and comparison of ancient and Mesozoic continental margins—Proceedings of the 8th International Conference on Basement Tectonics (Butte, Montana, 1988): Dordrecht, Netherlands, Kluwer Academic Publishers, p. 313–322.

Frost, C.D. 1993. Nd isotopic evidence for the antiquity of the Wyoming province. Geology, 21: 351–354.

Harms, T.A., Brady, J.B., Burger, H.R., and Cheney, J.T., 2004, Advances in the geology of the Tobacco Root Mountains, Montana, and their implications for the history of the northern Wyoming province, in Brady, J.B., Burger, H.R., Cheney, J.T., and Harms, T.A., eds., Precambrian geology of the Tobacco Root Mountains, Montana: Boulder, Colorado, Geological Society of America Special Paper 377, p. 227–243.

Hawkesworth, C. J., Cawood, P. A., and Dhuime, B., 2016, Tectonics and crustal evolution. GSA Today, 26(9), 4–11.

Holland, T. and Powell, R., 2003. Activity-composition relations for phases in petrological calculations: an asymmetric multicomponent formulation. Contributions to Mineralogy and Petrology, 145(4), pp. 492–501.

Kemp, A. I. S., Wilde, S. A., Hawkesworth, C. J., Coath, C. D., Nemchin, A., Pidgeon, R. T., and DuFrane, S. A., 2010, Hadean crustal evolution revisited: new constraints from Pb–Hf isotope systematics of the Jack Hills zircons. Earth and Planetary Science Letters, 296(1), 45–56.

Kemp, A. I. S., Wilde, S. A., 2010, Hadean crustal evolution revisited: new constraints from Pb–Hf isotope systematics of the Jack Hills zircons. Earth and Planetary Science Letters, 296, 45–56.

Mogk, D. W., Mueller, P. A., and Wooden, J. L.,1988, Archean tectonics of the North Snowy Block, Beartooth Mountains, Montana. The Journal of Geology, 96(2), 125–141.

Mogk, D. W., Mueller, P. A., and Wooden, J. L., 1992. The nature of Archean terrane boundaries: an example from the northern Wyoming Province. Precambrian Research, 55(1–4), 155–168.

Moore, W.B., and Webb, A.A.G., 2013, Heat-pipe Earth: Nature, v. 501, no. 7468, p. 501–505, doi: 10.1038/nature

Mueller, P.A., Wooden, J.L., Mogk, D.W., Nutman, A.P., and Williams, I.S., 1996, Extended history of a 3.5 Ga trondhjemitic gneiss, Wyoming province, USA: evidence from U–Pb systematics in zircon. Precambrian Research, 78: 41–52.

Mueller, P. A., Wooden, J. L., Mogk, D. W., Henry, D. J., and Bowes, D. R., 2010, Rapid growth of an Archean continent by arc magmatism. Precambrian Research, 183(1), 70–88.

Reid, R.R., McMannis, W.J. and Palmquist, J.C., 1975, Precambrian Geology of North Snowy Block, Beartooth Mountains, Montana (Vol. 157). Geological Society of America Special Paper.

Reimink, J. R., Davies, J., Chacko, T., Stern, R. A., Heaman, L. M., Sarkar, C., and Pearson, D. G., 2016, No evidence for Hadean continental crust within Earth's oldest evolved rock unit. Nature Geoscience, 9(10), 777–780.

Schmid, S. M., and Kissling, E., 2000, The arc of the western Alps in the light of geophysical data on deep crustal structure. Tectonics, 19(1), 62–85.

Searle, M. P., Law, R. D., and Jessup, M. J., 2006, Crustal structure, restoration and evolution of the Greater Himalaya in Nepal-South Tibet: implications for channel flow and ductile extrusion of the middle crust. Geological Society, London, Special Publications, 268(1), 355–378.

ROAD LOG TO XENOLITH LOCALITIES IN THE NORTHERN CRAZY MOUNTAINS

Francis Ö. Dudás

Massachusetts Institute of Technology

INTRODUCTION

This road log draws on previous logs by Dudás and Eggler (1989), Feltis and others (1972), Kendell (1981), Larsen and Simms (1972), Vice and others (1981), and Zieg and Godlewski (1986). The road log from Bozeman to Ringling is based exclusively on Lageson and others (1983). The local stratigraphic section is shown in table 1.

This field trip crosses major physiographic and geological boundaries (fig. 1). It starts west of the Rocky Mountain Front, and crosses, on the west side of the Bridger Range, the easternmost Basin-and-Range fault in Montana. It then crosses the Rocky Mountain Front on the east side of the Bridger Range into the "plains" physiographic province. Farther eastward, it crosses the eastern limit of the Montana disturbed belt, where the faults, thrusts, and folds that characterize western Montana are no longer important structural features.

The Crazy Mountains and the Crazy Mountains Basin lie between two major structures, the Nye–Bowler lineament to the south and the westward projection of the Lake Basin fault zone to the north (Garrett, 1972). The western margin of the basin is the Rocky Mountain Front, whereas the eastern margin is approximately coincident with the Fromberg Fault. The xenolith localities in the northern Crazy Mountains (fig. 1) are near the eastern boundary of the disturbed belt, north of the projected location of the Battle Ridge monocline that is thought to be the eastern boundary of the Helena salient of the Belt Basin.

Though Crazy Peak in the southern part of the Crazy Mountains reaches an elevation of 11,230 ft (3,424 m), the mountains are exclusively an igneous feature, with the subalkaline Big Timber and Loco Mountain stocks and their hornfels aureoles forming the high peaks. The Crazy Mountains are thus not considered part of the Rocky Mountains. They lie on the east edge of the Helena Embayment of the Belt Basin, and it is likely that Belt Supergroup rocks pinch out in the subsurface somewhere in the northern part of the range, possibly along the trace of the Battle Ridge monocline. The Shields River drains westward from the central part of the Crazy Mountains and forms an approximate boundary between subalkaline (gabbro to granite) igneous rocks to the south, and alkaline rocks to the north. The two rock series are contemporaneous within the limits of existing geochronological data, and are distinguishable by the presence of plagioclase in the subalkaline rocks, and its absence in the alkaline rocks. There is a suite of rocks of intermediate composition (58–65 wt.% SiO_2) that appears to be a mixture of subalkaline and alkaline magmas.

Previous field trips to the Crazy Mountains—the IGC field trip in 1989—focused on the alkaline rocks (Dudás and Eggler, 1989). This field trip highlights three locations in which xenoliths are prominent. The first two locations are in the northern Crazy Mountains, whereas the third is just west of Livingston, and is in rocks that are much younger than the Crazy Mountains locations (42 Ma vs. 48–50 Ma). Xenoliths are common in the alkaline rocks of the northern Crazy Mountains, so that the selected locations are highlights of a general phenomenon.

ROAD LOG

0 mi: (GPS: 45.6998N, 111.0310W)

Junction of Griffin Drive, Bozeman, with MT 86, Bridger Canyon Drive. Follow MT 86 eastward, crossing the East Fork of the Gallatin River.

1.3 mi: Poorly stratified and variably consolidated strata of the Tertiary Bozeman Group are to the south (right). Hummocky landslides developed in the hills to the right. On the left and ahead, the N–S-trending Bridger Range forms the skyline.

1.7 mi: Cross Bridger Creek near confluence with Lyman Creek from the north.

2.0 mi: West edge of figure 2, showing geology of the Bridger Canyon area.

2.5 mi: Entrance to the Bozeman Fish Technology Center.

Table 1. Stratigraphic section for the Crazy Mountains area, Montana (Balster, 1980).

Cenozoic	Paleocene		Fort Union Fm.		Fort Union Fm.
Mesozoic	Cretaceous		Hell Creek Fm.		Hoppers Fm.
			Bearpaw Fm.		Billman Ck. Fm.
		Montana Group	Judith River Fm.	Livingston Group	Miner Ck. Fm.
			Claggett Fm.		Cokedale Fm.
			Eagle Fm.		
			Telegraph Creek Fm.		
		Colorado Group	Cody Fm.		
			Frontier Fm.		
			Big Elk Fm.		
			Mowry Fm.		
			Thermopolis Fm.		
			First Cat Creek Ss.		
			Kootenai Fm.		
	Jurassic		Morrison Fm.		
		Ellis Group			
	Triassic		Dinwoody Fm.		
Paleozoic	Permian		Phosphoria Fm.		
	Pennsylvanian		Quadrant Fm.		
			Amsden Fm.		
	Mississippian	Big Snowy Group			
		Madison Group	Lodgepole, Mission Canyon		
	Devonian		Three Forks Fm.		
			Jefferson Fm.		
			Maywood Fm.		
	Ordovician		Bighorn Fm.		
	Cambrian		Grove Creek Fm.		
			Snowy Range Fm.		
			Pilgrim Ls.		
			Park Sh.		
			Meagher Ls.		
			Wolsey Sh.		
			Flathead Ss.		
Proterozoic			Spokane Fm.		
			Greyson Sh.		
		Belt Supergroup	Newland Ls.		
			Chamberlain Sh.		
			Neihart Qtzt.		
Archean			Crystalline basement		

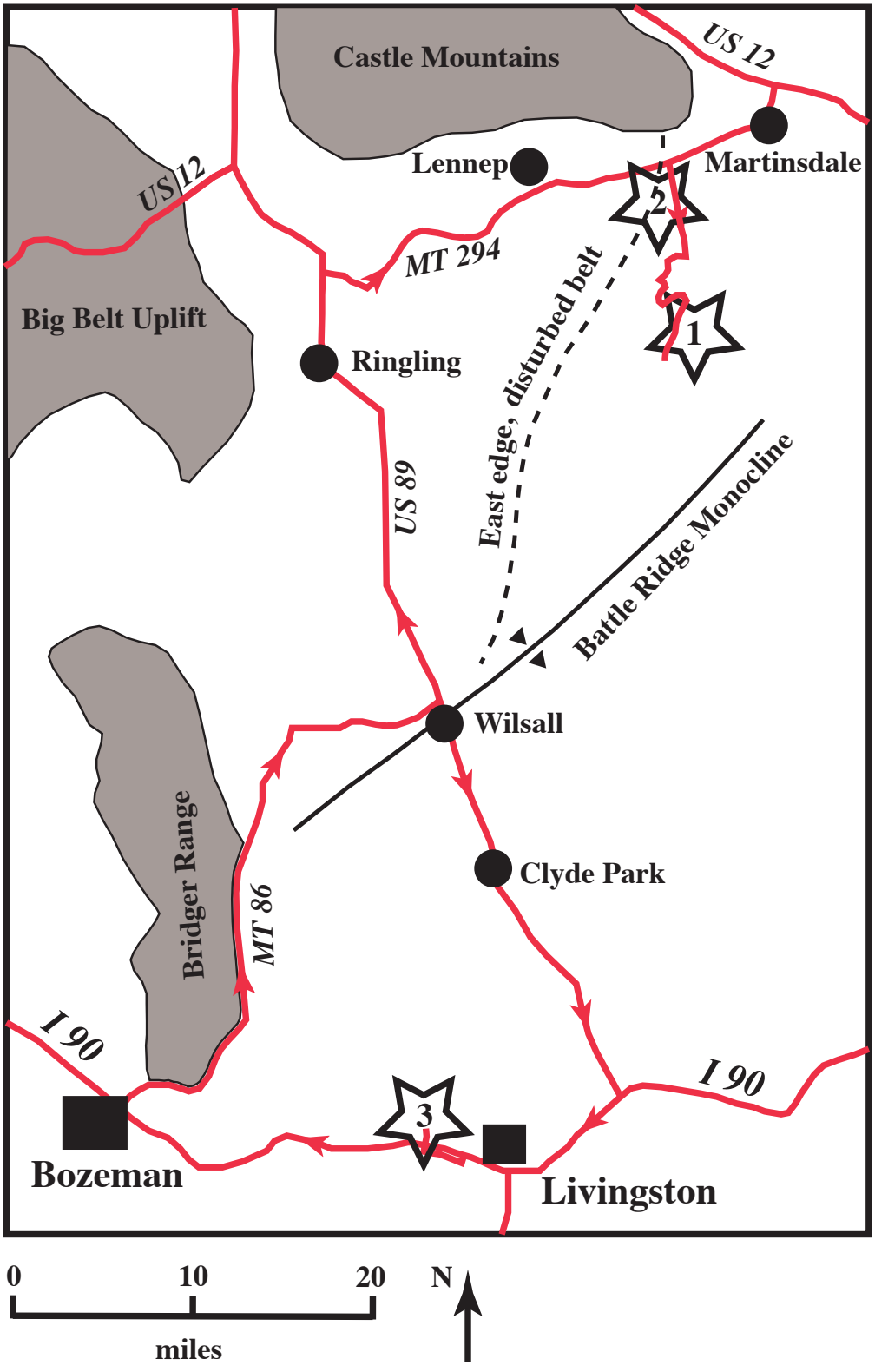

Figure 1. Regional geologic map and field trip route. The locations of the eastern limit of the disturbed belt and the Battle Ridge monocline are based on Woodward (1981).

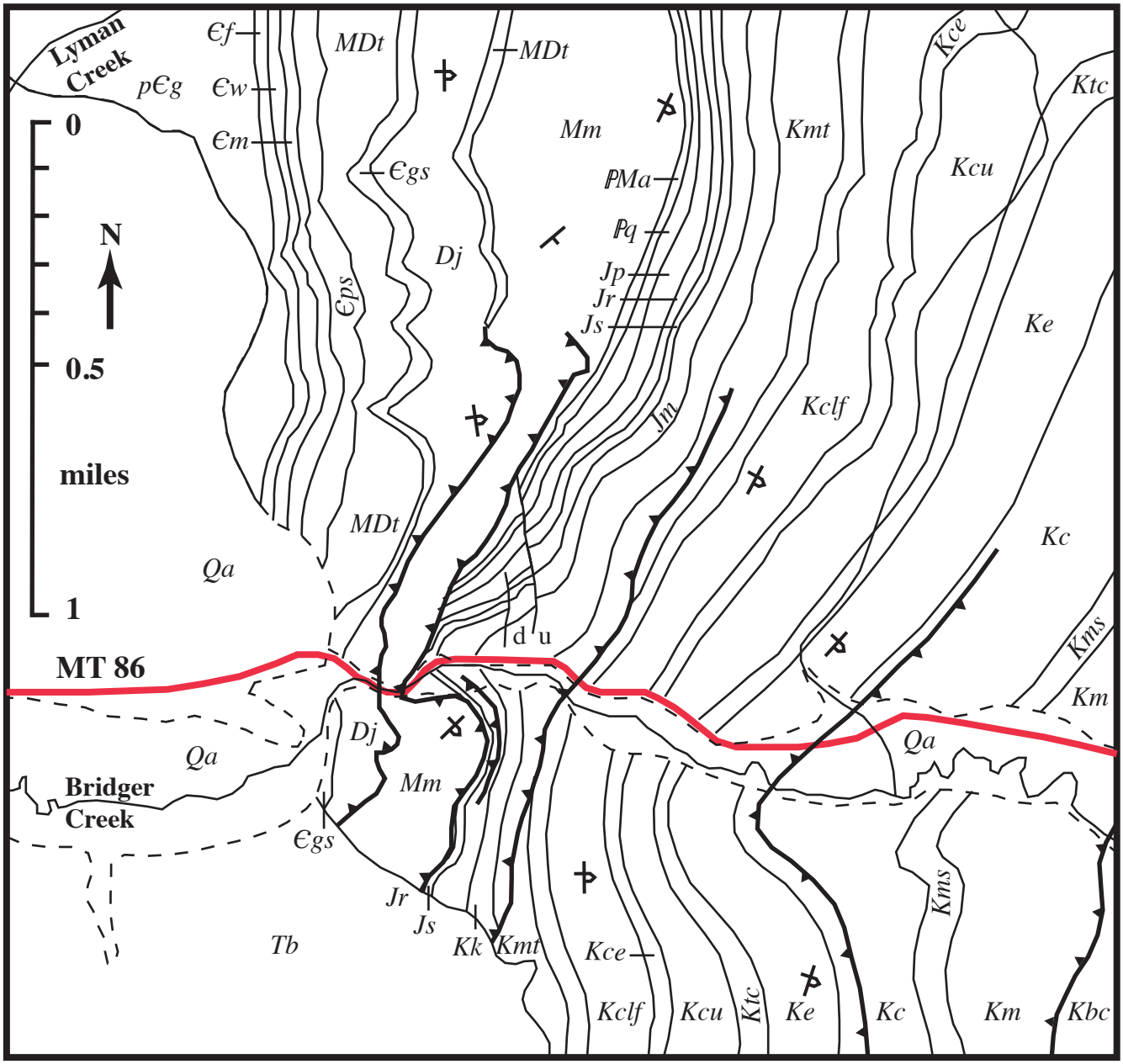

***Qa*: alluvium**
***Tb*: Bozeman Group**
***Kbc*: Billman Creek Fm.**
***Km*: Miner Creek Fm.**
***Kms*: Miner Creek Fm. ss**
***Kc*: Cokedale Fm.**
***Ke*: Eagle Fm.**
***Ktc*: Telegraph Creek Fm.**
***Kcu, Kce, Kclf*: Colorado Group**
***Kmt*: Colorado Group**
Mowry, Thermopolis Fms.
***Kk*: Kootenai Fm.**

***Jm*: Morrison Fm.**
***Js, Jr, Jp*: Swift, Rierdon, Piper Fms.**
***Pq*: Quadrant Fm.**
***PMa*: Amsden Fm.**
***Mm*: Madison Group**
***MDt*: Three Forks Fm.**
***Dj*: Jefferson Fm.**
***Cgs*: Grove Creek, Snowy Range Fms.**
***Cps*: Park Shale**
***Cm*: Meagher Limestone**
***Cw*: Wolsey Shale**
***Cf*: Flathead Sandstone**
***pCg*: Archean gneiss, granite**

Figure 2. Map of the Bridger Canyon area (redrawn after fig. 4 in Lageson and others, 1983, based on Roberts, 1964).

2.7 mi: Intersection with Fish Hatchery Road on south. Cross (approximately) the trace of the range-front Basin-and-Range fault that is the west side of the Bridger Range.

2.8 mi: Narrows of Bridger Canyon, cut into overturned and thrusted Mississippian Lodgepole Limestone. The cliff-forming Lodgepole Ls. is dolomitic in its lower part, with a concentration of chert near the base. The landslide on the right side is in Big Snowy–Amsden Fm. Rocks.

2.9 mi: Imbricate thrusting on the left side has placed the Lodgepole Ls. in contact with the gray, oolitic basal part of the Jurassic Rierdon Ls. Going eastward, the beds are overturned strata of the east limb of the Bridger Range anticlinorium. Roberts (1964) mapped six thrust faults between the narrows of the Bridger Canyon and the Billman Creek strike valley (fig. 2). Eastward, the road crosses upsection through Cretaceous rocks, with the best exposures on the left (north) side.

3.2 mi: A thrust fault (left) placed Lower Cretaceous Mowry Fm. and Thermopolis Fm. shales over the lower shale member of the Cody Fm. and the Frontier Fm.

3.6 mi: Upper Cretaceous Eagle Fm. in roadcut to left.

3.8 mi: Inferred thrust fault in Upper Cretaceous Cokedale Fm. Dip angles change from overturned, W-dipping strata to E-dipping upright beds on the east limb of the Bridger Range anticlinorium.

4.6 mi: Crossing the trace of an inferred thrust fault between the Upper Cretaceous Miner Creek and Billman Creek Formations (both Livingston Group). The Bridger Creek floodplain is on the right. For the next several miles, MT 86 follows a strike valley in rocks of the Billman Creek Fm.

6.7 mi: The Beasley Creek valley is on the left, with the southern Bridger Range on the skyline. Mississippian Madison Group rocks form the crest of the range. On the right, E-dipping strata of the Hoppers Fm. (Livingston Group) form the hills beyond the Bridger Creek floodplain.

7.8 mi: Miner Creek Fm. (Livingston Group) in the roadcut.

9.3 mi: MT 86 crosses Bridger Creek.

9.7 mi: Panoramic view of the east side of the Bridger Range on the left.

11.0 mi: Billman Creek Fm. strata in roadcuts on the left, dipping 50–60° E. Low, timbered hills to the west are formed by Jurassic and Cretaceous strata, dipping E.

14.2 mi: Access to Bridger Bowl ski area on left.

14.7 mi: Cross-Cut cross-country ski & biathlon parking lot on left.

14.9 mi: Billman Creek Fm. rocks in roadcuts.

16.1 mi: The low saddle in the Bridger Range on the left is Ross Pass. It separates the southern part of the Bridger Range (Archean metamorphic and meta-igneous rocks on the west flank) from the northern part of the range (Proterozoic Belt rocks on the western side). Steeply dipping Phanerozoic rocks form the east side of the range (McMannis, 1955). Ross Pass is on strike with the Battle Ridge monocline that lies to the east, and possibly with the Jefferson Canyon structural trend to the west, and thus may represent the southern boundary of the Helena salient of the Belt Basin, and the southern limit of thin-skinned deformation in this part of Montana. In the Bridger Range, there is superposition of young, Basin-and-Range extension on older, Cretaceous to Early Tertiary compressional features. Woodward (1981) discusses the structural setting of the Montana disturbed belt in detail.

17.3 mi: Brackett Creek Road intersection

19.0 mi: Battle Ridge pass (elev. 6,372 ft, 1,943 m). The road cuts down-section through NE-striking, NW-dipping, overturned Livingston Group rocks on the northwest side of the Battle Ridge monocline. Purple mudstone and light-colored sandstone are in the upper part of the Billman Creek Fm.

20.0 mi: Miner Creek Fm. rocks in roadcuts.

21.5 mi: Folded and faulted beds of the lower Billman Creek Fm. and the upper part of the Miner Creek Fm. ahead on the right.

22.7 mi: Cross Cache Creek.

23.5 mi: MT 86 climbs onto alluvial-outwash terrace.

25.9 mi: Flathead Pass road on left. Flathead Pass is the low saddle at the north end of the Bridger Range, the location of the type section of the Cambrian Flathead Fm.

27.0 mi: Intersection of MT 86 with the Muddy Creek road. MT 86 turns east (right). The Battle Ridge monocline is ahead on the right, and the Elkhorn Ridge anticline is to the north (left). Drilling in the 1970s and 1980s showed some oil and gas in structural traps along the Battle Ridge monocline. The Elkhorn Ridge anticline is a doubly plunging, E-verging structure associated with the Horse Butte thrust to the N. MT 86 continues on Livingston Group strata capped by alluvium. Low hills on either side are mostly Hoppers Fm. rocks.

35.7 mi: (GPS: 46.0130N, 110.6649W)

Junction of MT 86 with US 89. Panoramic view of the Crazy Mountains to the east. The main drainage on the west side of the Crazies is the Shields River, named for a member of the Lewis and Clark expedition. The Shields River Road, 1 mi south of the MT 86–US 89 junction, is the easiest access point for alkaline rock exposures on the west side of the Crazy Mountains (Three Peaks, Billie Butte, Anticlinal Phacolith, the Great Cliffs, and Target Rock), and for subalkaline rock exposures along the Shields River drainage.

From this point northward, US 89 traverses Livingston Group strata that are equivalent to the Hell Creek Fm. in age. The highway generally parallels the N–S structural trend, and follows the Wilsall Syncline. The Ringling Anticline lies to the west, whereas the Potter Basin Anticline lies to the east. Both anticlines have been drilled for oil, with no success. As the road turns to the northwest, it crosses onto the east flank of the Ringling Anticline and cuts down-section.

Turn left (north) on US 89.

37.0 mi: Billman Creek Fm. in roadcuts.

37.4 mi: Dissected alluvial terraces to the east along the Shields River.

39.6 mi: Billman Creek Fm. in roadcuts. Ahead, the road follows the Wilsall Syncline for ~3 mi.

46.2 mi: Billman Creek Fm. in roadcuts for next 3 mi.

55.3 mi: US 89 crosses from E-dipping Livingston Group strata to alluvium of 16-Mile Creek.

55.8 mi: Nose of the Ringling Anticline. Cretaceous Telegraph Creek and Eagle Formation rocks form low hills ahead to right.

55.5 mi: (GPS: 46.2174N, 110.8036W) Town of Ringling.

56.8 mi: Contact of the Montana Group (Telegraph Creek Fm.) with the Colorado Group (Cody Fm.). Horse Butte to the WNW exposes several thrust faults that displace Cretaceous Cody Fm. and Telegraph Creek Fm. rocks here, but juxtapose Mississippian Madison Group and Cody Fm. rocks further north. Northward, Paleozoic rocks are exposed west of US 89, in the hanging wall of the Horse Butte thrust, whereas folded Cretaceous strata extend to the east. The red slopes on the northward extension of Horse Butte are the Spokane Fm. of the Belt Supergroup, the only exposures of the Belt that this field trip will encounter.

60.1 mi: (GPS: 46.3381N, 110.8043W)

Junction of US 89 with MT 294. Turn right (east) on MT 294. MT 294 is on Colorado Group shales. The Moss Agate Anticline is the first structure that the road crosses; at 63.4 mi, the road crosses the axis of the Potter Basin Syncline, and at 66.0 mi, it crosses the axis of the Loweth Anticline. Alkaline dikes and sills associated with the dike swarm centered on the Comb Creek Laccolith extend at least this far west. The Upper Cretaceous section (table 1) is exposed in its entirety on the east limb Loweth Anticline, and records at least two transgressions of the Upper Cretaceous inland sea. Notable bentonites occur in the Judith River Fm. The road crosses the axis of the Hensley Syncline at 69.6 mi, and encounters the west flank of the Robinson Anticline at about 70.3 mi. The Robinson Anticline can be traced south in the Crazy Mountains through the Great Cliffs and the Anticlinal Phacolith (Harlan and others, 1988). The next major structure is the Coral Creek Anticline, whose crest is at 72.7 mi.

73.5 mi: Several malignite (MNS: see Dudás in this volume for description) dikes intrude Bearpaw Shale in roadcuts on the south side of the road (fig. 3). The dikes radiate from the Comb Creek laccolith, a nepheline syenite intrusion that is about 6 mi south

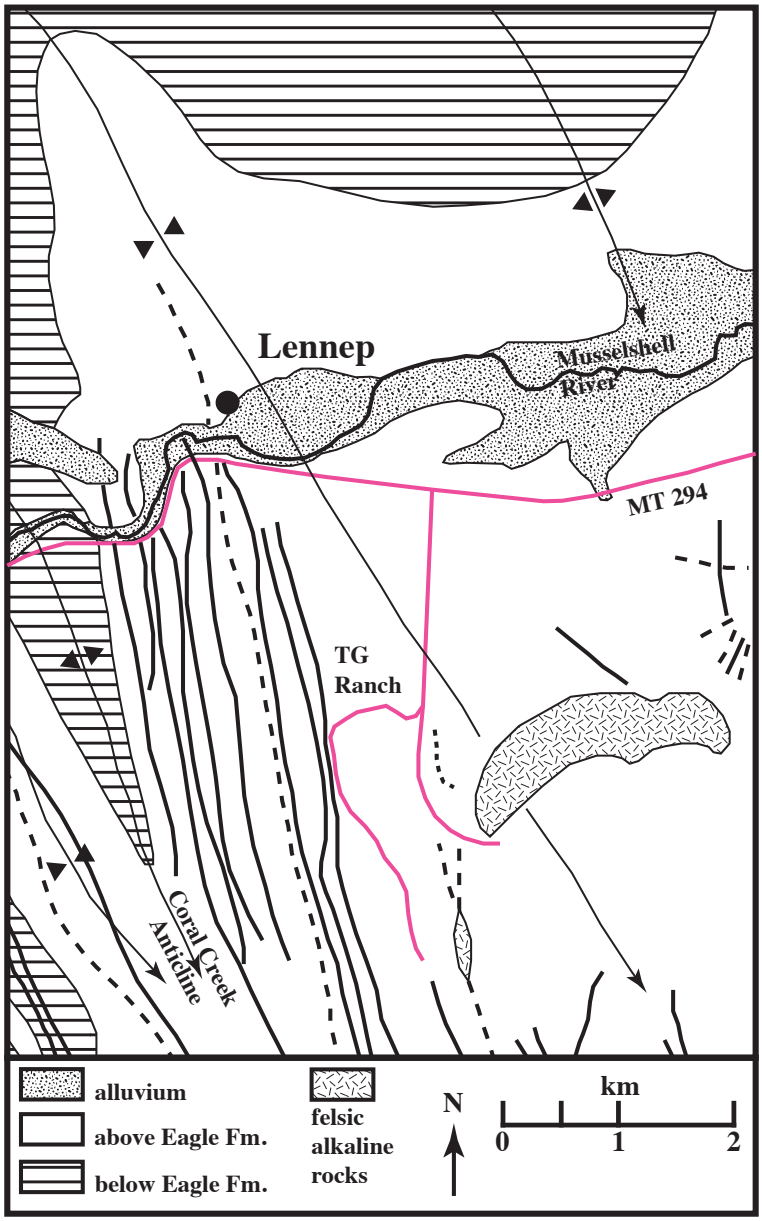

Figure 3. Map of the area near Lennep, showing major structures and dikes. General geology from Sims (1967); igneous rocks modified from Fink (1975). Solid lines are mafic alkaline rocks; long dashed lines are felsic alkaline rocks; short dashed lines show a non-alkaline lamprophyre.

of this exposure, and include a range of lithologies: malignite, phonolite, trachyte, and lamprophyre. Eocene, silica-saturated intrusions form the core of the Castle Mountains to the north. Castle, now a ghost town, was a center of silver mining and had a population exceeding 5,000 in 1893. The Pb isotopic composition of ores from Castle indicates Precambrian crustal sources similar to those of the ores from Neihart to the north (table 2).

78.3 mi: The top of the Lower Cretaceous Kootenai Fm. is exposed in the core of an anticline to the north.

81.9 mi: Cottonwood Creek Road. Turn right (south). To the east lies Gordon Butte, a malignite sill that is the largest alkaline intrusion in the Crazy Mountains.

88.1 mi: Turn right onto the Forest Lake road. The road is often muddy and rutted. Four wheel drive is recommended. Numerous dikes are exposed along the road.

92.8 mi: Crossing of the West Fork of Cottonwood Creek. The dikes exposed near the crossing include lamprophyres and trachytes. A phonolite dike is exposed along the road approx. 0.8 mi further, beyond a sharp switchback.

STOP 1 — 96.8 mi

(GPS: 46.2726 N, 110.4198 W)

The outcrops of the Castle Creek pipes are clearly visible on the skyline to the east (fig. 4). The pipes are located in the south-central part of

Table 2. Pb isotopic compositions of samples from the Castle and Neihart areas.

Location	Location	Sample	^{206}Pb / ^{204}Pb	^{207}Pb / ^{204}Pb	^{208}Pb / ^{204}Pb
Castle		Galena 04-9/5-6	16.097	15.311	36.688
Castle		Cerussite 04-9/5-7	16.071	15.285	36.600
Neihart	Carpenter Creek	Galena	17.087	15.456	37.627
Neihart		Galena	17.084	15.439	37.579
Neihart		Galena	17.026	15.438	37.535
Neihart	Cascade Silver Mines	Galena	16.982	15.411	37.444

Note. Measured ratios corrected for mass fractionation of 0.12 ± 0.03 %/a.m.u. based on replicate analyses of NBS-981; precision of ratios is ≤0.1%. Analyses completed in the laboratory of Dr. S.A. Bowring at Mass. Inst. Technology. Cascade Silver Mines sample collected by W. Lindgren, from the Lindgren collection at MIT.

Figure 4. View eastward from the Forest Lake Road, showing the Castle Creek pipes on the skyline.

sec. 13 of T. 6 N., R. 10 E. Park vehicles along Forest Lake Road. Cross Cottonwood Creek and climb to the exposures on the south-facing hillside. Access is easiest from the Cottonwood Creek side; the hillside along Castle Creek is very steep. It is approximately 500 ft, vertically, from Cottonwood Creek to the top of the upper pipe.

There is no bridge at the creek crossing; be prepared with wading boots or water mocs. The meadows along Cottonwood Creek have been used for grazing cattle, and have been infested with ticks in past years.

Section 1 of the author's preceding paper in this volume provides a detailed discussion of this location. The most spectacular xenolith exposure (fig. 4 of the preceding paper) is on the west-facing side, near the north end of the lower pipe. The upper pipe has fewer and smaller Archean xenoliths, but carries a larger number of clinopyroxenite and amphibolite xenoliths.

Return to vehicles and retrace route toward MT 294.

105.5 mi: Junction with Cottonwood Creek Road. Continue northward.

STOP 2 — 108.6 mi

(GPS: 46.3887 N, 110.4066 W)

Park vehicles on Cottonwood Creek Road. This is private land, owned by the TG Ranch: enter with permission only. Follow road to west through the gate. The outcrop of interest is located in the NE 1/4 of the SE 1/4 of sec. 1, T. 7 N., R. 10 E. Walk northward approximately 0.3 mi to a small hill where clinopyroxenite xenoliths are exposed in an MNS plug. Section 2 of the author's preceding paper in this volume provides a detailed discussion of this location.

Return to vehicles and drive to the junction of the Cottonwood Creek Road with MT 294.

Reset odometer to 0 at junction of Cottonwood Creek Rd. with MT 294.

21.8 mi: Junction with US 89. Turn left (south).

70.5 mi: Junction of US 89 and I-90. Turn right (west) onto I-90.

79.9 mi: Take exit #330. At stop, turn left, cross under I-90, and follow the Frontage Road westward.

83.0 mi: Turn right onto O'Rea Creek Road.

STOP 3 — 83.4 mi

(GPS: 45.6658 N, 110.6806 W)

Park vehicles near railroad tracks.

CAUTION: This is a very busy rail line. Take care near the tracks and when crossing them. Walk approx. 0.5 mi westward to the railroad cut where the Haymond School dike is exposed.

This location (fig. 5) is described in Dudás and Harlan (1999). The dike is an alkaline lamprophyre (camptonite) that is significantly younger (42 Ma) than the magmatism of the Crazy Mountains. It carries a variety of xenoliths and megacrysts, most of which are smaller than 5 cm. Some are crustal (granitoids or syenitic rocks, mostly with no gneissic fabric; rare, granulite-facies spinel-cordierite xenoliths are hard to see because their color blends with the host rock), some are probably cognate (mostly megacrysts of K-feldspar and amphibole), whereas others are apparently mantle-derived. Their mantle provenance is inferred from thermobarometry on pyroxene (T ~ 1,200°C; P ~ 3.5 GPa) and unusually depleted Nd isotopic compositions (ε_{Nd}, 42 = 17).

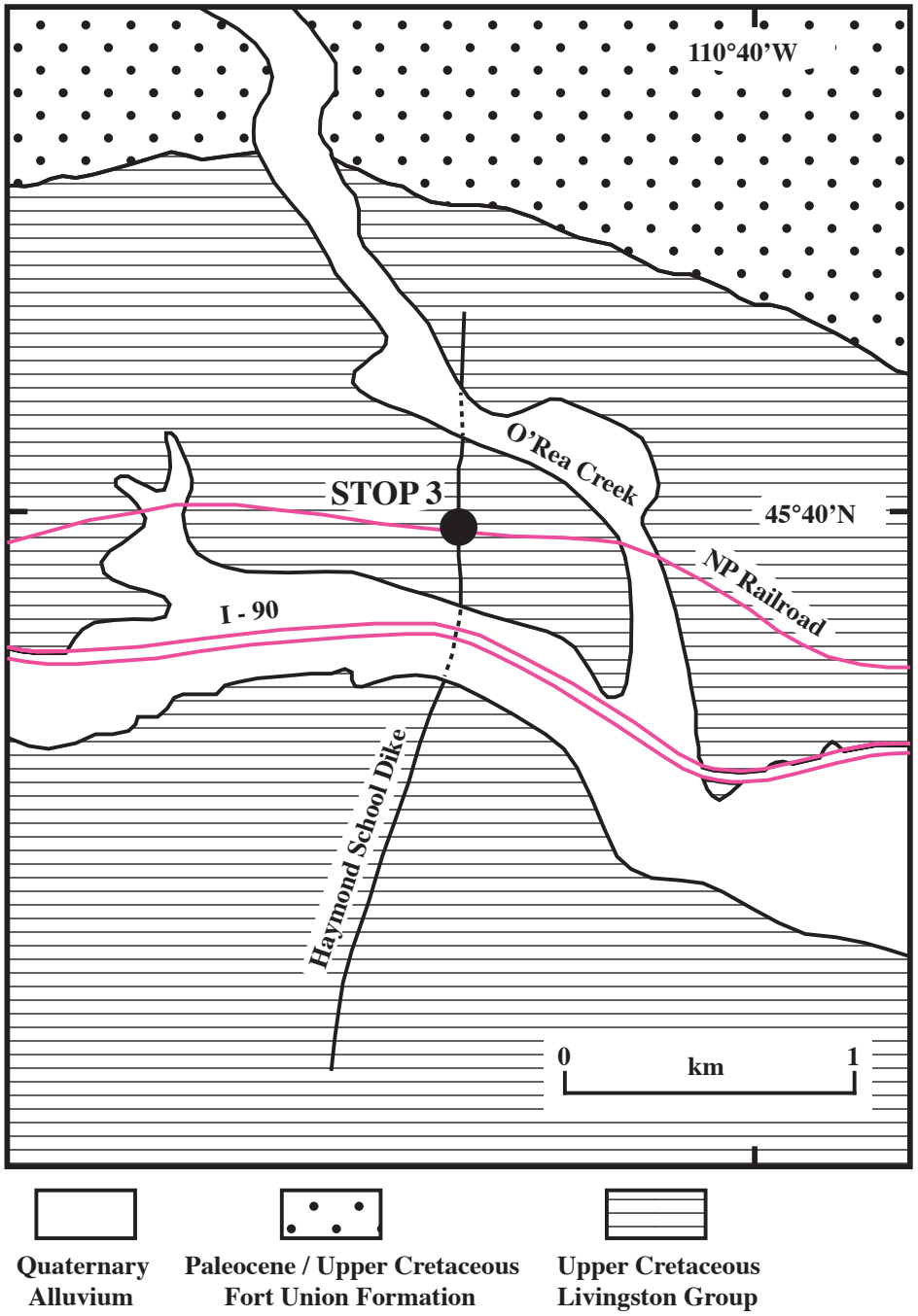

Figure 5. Generalized geological map of the area near the Haymond School dike (Stop 3). Redrawn after Roberts (1972).

Roberts (1972) mapped a number of other Tertiary dikes in the area south and west of Livingston. There is no information on their age or composition. Some of them contain xenoliths (e.g., in a roadcut at 45.5255N, 110.7024W). At this location, the xenoliths are mafic or ultramafic, but are small and strongly altered, so that no useful information can be derived from them.

ACKNOWLEDGMENTS

Jesse Mosolf and Sandra Underwood assisted with fact-checking this log, but all errors are mine alone. Sandra's review and editorial oversight have been invaluable. I owe a great debt to all of the geologists who have mapped and studied these rocks, and can claim personal knowledge only of the field stops described here.

REFERENCES

Balster, C.A., 1980, Stratigraphic nomenclature chart for Montana and adjacent areas. Montana Bureau of Mines and Geology, Geologic Map 8.

Dudás, F.Ö., and Eggler, D.H., 1989, Crazy Mountains, Montana, *in* B.C. Hearn, Jr., and others, eds., Montana High-Potassium Igneous Province, p. 7–22, Field Trip Guidebook T 346, International Geological Congress, American Geophysical Union, Washington, D.C.

Dudás, F.Ö., and Harlan, S.S., 1999, An ancient depleted mantle sample from a 42-Ma dike in Montana: Constraints on the persistence of lithosphere during Eocene magmatism. Journal of Geology, 107:287–299.

Feltis, R.D., Miller, W.R., Wurden, F., and Larsen, R., 1972, Bozeman to Harlowton, *in* Lynn, J., Balster, C.A., and Warne, J., eds., Crazy Mountains Basin: 21st Annual Field Conference, Billings, Guidebook, Montana Geological Society, pp. 211–217.

Fink, R.A., 1975, The geology and igneous petrology of the Comb Creek dike swarm, Crazy Mountains, Montana. M.S. thesis, University of Cincinnati, Cincinnati, OH. 174 pp., unpublished.

Garrett, H.L., 1972, Structural geology of the Crazy Mountains Basin. Montana Geological Society, 21st Annual Field Conference Guidebook, p. 113–118.

Harlan, S.S., Geissman, J.W., Lageson, D.R., and Snee, L.W., 1988, Paleomagnetic and isotopic dating of thrust-belt deformation along the eastern edge of the Helena salient, northern Crazy Mountains Basin, Montana. Geological Society of America Bulletin, 100:492–499.

Kendell, C., 1981, Billings to Big Timber, *in* Tucker, T.E., ed., Field Conference and Symposium, Guidebook, Montana Geological Society, pp. 373–375.

Lageson, D.R., Schmidt, C.J., Dresser, H.W., Welker, M., Berg, R.B., and James, H.L., 1983, Road Log No. 1: Bozeman to Helena via Battle Ridge Pass, White Sulphur Springs, Townsend and Toston, *in* D. Smith, compiler, Guidebook of the Fold and Thrust Belt, West-Central Montana, Montana Bureau of Mines and Geology Special Publication 86, p. 1–31.

Larsen, L.H., and Simms, F.E., 1972, Igneous geology of the Crazy Mountains, Montana—a report of work in progress. Montana Geological Society, Field Conference Guidebook, 21:135–139.

McMannis, W.J., 1955, Geology of the Bridger Range, Montana. Geological Society of America Bulletin, 66:1385–1430.

McMannis, W.J., 1965, Resume of depositional and structural history of western Montana. American Association of Petroleum Geologists Bulletin, 49:1801–1823.

Roberts, A.E., 1964, Geologic map of the Fort Ellis quadrangle, Montana. U.S. Geological Survey Miscellaneous Geological Investigations Map I-397, 1:24,000.

Roberts, A.E., 1972, Cretaceous and Early Tertiary depositional and tectonic history of the Livingston area, southwestern Montana. U.S. Geological Survey Professional Paper 526-C, 120 pp.

Sims, J.D., 1967, Geology and sedimentology of the Livingston Group, northern Crazy Mountains, Montana. Ph.D. thesis, Northwestern University, Evanston, IL. 112 pp., unpublished.

Vice, D., Vice, M., Hupp, W., and Tucker, T., 1981, Big Timber to Livingston, *in* Tucker, T.E., ed., Field Conference and Symposium, Guidebook, Montana Geological Society, pp. 375–380.

Woodward, L.A., 1981, Tectonic framework of the disturbed belt of west-central Montana. American Association of Petroleum Geologists Bulletin, 65:291–303.

Zieg, G.A., and Godlewski, D.W., 1986, Road log No. 1: A traverse across the eastern Belt basin from Neihart to Townsend, Montana, *in* Roberts, S.M., ed., Belt Supergroup: A Guide to the Proterozoic Rocks of Western Montana and Adjacent Areas. Montana Bureau of Mines and Geology Special Publication 94, p. 1–16.

NORTHWEST GEOLOGY

The Journal of The Tobacco Root Geological Society

Volume 47, July 2018

Southwest Montana Geology from the Helena Salient to the Drainages Connecting Yellowstone Park

TABLE OF CONTENTS